UNIVERSITÄT PADERBORN
FAKULTÄT FÜR NATURWISSENSCHAFTEN

Experimental and Theoretical (High Energy Resolution) X-Ray Absorption and Emission Spectroscopy

DISSERTATION

vorgelegt von

PATRICK MÜLLER

Zur Erlangung des akademischen Grades
DOKTOR DER NATURWISSENSCHAFTEN (DR. RER. NAT.)
im Department Chemie

Paderborn 2019

Promotionskommission

Prof. Dr.-Ing. Hans-Joachim Warnecke	Vorsitz
Prof. Dr. Matthias Bauer	Erstgutachter
Prof. Dr. Thomas D. Kühne	Zweitgutachter
Prof. Dr. Wolf Gero Schmidt	

UNIVERSITÄT PADERBORN

Universität Paderborn
Fakultät für Naturwissenschaften
Chemie

Eidesstattliche Erklärung

Hiermit versichere ich, die vorliegende Arbeit selbständig angefertigt und keine anderen als die von mir angegebenen Hilfsmittel verwendet zu haben. Wörtliche und sinngemäße Zitate wurden als solche gekennzeichnet und die Genehmigungen zur Veröffentlichung der urheberrechtlich geschützten Publikationen wurden eingeholt.

Paderborn, 5. April 2019

....
Patrick Müller

Halte Dir jeden Tag dreißig Minuten für Deine Sorgen frei
und mache in dieser Zeit ein Nickerchen
— ***Abraham Lincoln***

Abstract

Copper catalysed electron transfer reactions are very versatile in nature and should be exploited for industrial applications. This, however, needs a detailed understanding of the involved mechanism and the concomitant changes of geometric and electronic structure. Therefore this work aims at elucidating these parameters with X-ray absorption and emission techniques in conjunction with various theoretical approaches.

In case of so called entatic state models it could be shown that a combination of high energy resolution fluorescence detected X-ray absorption near edge structure (HERFD-XANES) and various density functional theory (DFT) calculations can reveal even small geometric changes and the concomitant change of the electronic structure. Since most of the reactions occur in solution and at room temperature, the same model complex was investigated regarding finite-temperature and condensed phase effects. It could be shown that including these via periodic boundary conditions and molecular dynamics further improves the results.

A second model complex, this time for the $\mathrm{Cu_A}$ center, was investigated with HERFD-XANES and valence-to-core X-ray emission spectroscopy (VtC-XES). In conjunction with DFT calculations the electronic structure is elucidated. In this case VtC-XES is especially helpful since different ligands can be studied separately. In addition a theoretical study reveals distinct differences for a reduced mixed-valent compound which would be the electronic structure model for a $\mathrm{Cu_A}$ center.

Kurzzusammenfassung

Kupfer katalysierter Elektronentransfer ist eine der vielseitigsten Reaktionen in der Natur und sollte für industrielle Anwendungen genutzt werden. Hierfür ist jedoch ein detailliertes Verständnis zugrunde liegender Mechanismen und damit einhergehender Änderungen der Geometrie und elektronischen Struktur unabdingbar. Ziel dieser Arbeit ist daher die Untersuchung dieser Parameter unter Verwendung von Röntgenabsorptions- und Emissionsspektroskopie in Kombination mit theoretischen Methoden.

Für Modelle des sogenannten „Entatischen Zustands“ konnte gezeigt werden, dass selbst kleinste geometrische und einhergehende elektronische Strukturänderungen durch eine Kombination von HERFD-XANES und theoretischen Methoden aufgedeckt werden können. Da die meisten dieser Reaktionen in Lösung und bei Raumtemperatur ablaufen, wurde das gleiche System zusätzlich auf den Einfluss von endlicher Temperatur und Aggregatzustand untersucht. Die Beschreibung dieser Effekte mittels periodischer Randbedingungen und Molekulardynamik verbesserte die Ergebnisse.

Ein weiterer Modellkomplex, in diesem Fall für das Cu_A Zentrum, wurde mittels HERFD-XANES und VtC-XES untersucht. In Kombination mit DFT Rechnungen konnte die elektronische Struktur aufgeklärt werden. Hilfreich war hierbei insbesondere VtC-XES, da hiermit verschiedene Liganden separat untersucht werden können. Eine theoretische Studie zeigt eindeutige Unterschiede für eine gemischt-valente Spezies, welche die korrekte elektronische Struktur des Cu_A Zentrums aufweist.

Danksagung

Ich möchte an dieser Stelle einigen Leuten für ihre Unterstützung und ihr Vertrauen während der Anfertigung dieser Arbeit danken.

Allen voran danke ich Matthias Bauer für die Chance zur Promotion in seinem Arbeitskreis auf dem interessanten Themengebiet der Röntgenspektroskopie und das damit in mich gesetzte Vertrauen. Ich möchte mich bei ihm nicht nur für die fachliche Unterstützung, sowie die Möglichkeit zur Teilnahme an diversen Messzeiten und Konferenzen bedanken, sondern ebenso für den freundlichen und entspannten Umgang auch abseits der Wissenschaft.

Mein Dank gilt außerdem Thomas Kühne für die freundliche Aufnahme in seinen Arbeitskreis, die Erweiterung des interessanten Forschungsthemas und meines Wissens durch einen gänzlich neuen Blickwinkel, sowie die Übernahme des Zweitgutachtens.

Den Kollegen im Arbeitskreis Kühne möchte ich für eine freundliche Aufnahme in ihren Reihen danken und für die entspannte und nette Arbeitsatmosphäre.

Allen ehemaligen und derzeitigen Kollegen im Arbeitskreis Bauer danke ich für die tolle, teilweise verrückte, Atmosphäre, sowohl auf als auch abseits der Arbeit und insbesondere auf Messzeiten. Neben zahlreichen fachlichen Diskussionen gab es glücklicherweise auch genug Momente zum Abschalten mit Gesprächsstoff fernab von Arbeit und Chemie. Durch euch ist der Spaß nie zu kurz gekommen und sogar Montage wurden durch Pub Quiz- sowie diverse Kinobesuche (natürlich auch an anderen Tagen) stark aufgewertet. Dafür nochmal vielen Dank!

Besonders danke ich hier noch meiner langjährigen Büro Leidensgenossin Rahel Schepper für unzählige Tassen Tee, diverse Quälereien (auch unter dem Euphemismus *Sporteinheiten* bekannt) und das Lösen zahlreicher Probleme durch simples Zuhören.

Zu guter Letzt danke ich meiner Familie, ohne deren Unterstützung und blindes Vertrauen vieles, insbesondere Studium und Fertigstellung dieser Arbeit, nicht möglich gewesen wäre.

List of Beamtimes

Ångstrømquelle Karlsruhe (ANKA)

XAS

- November 12-14 2015

Deutsches Elektronensynchrotron (DESY)

P64

- September 3-12 2017
- July 2-9 2018
- April 11-17 2019

P65

- June 2-6 2016
- July 25-29 2016
- September 15-20 2016
- October 28 - November 2 2016
- April 20-25 2017
- May 11-15 2017

Diamond Light Source

B18

- August 7-11 2017

European Synchrotron Radiation Facility (ESRF)

BM25a

- July 19-24 2017

ID26

- April 14-21 2015
- November 15-22 2016
- February 21-27 2018
- June 13-19 2018

List of Publications

Publications in Journals

1. N. J. Vollmers, P. Müller, A. Hoffmann, S. Herres-Pawlis, M. Rohrmüller, W. G. Schmidt, U. Gerstmann, M. Bauer: 'Experimental and Theoretical High-Energy-Resolution X-Ray Absorption Spectroscopy: Implications for the Investigation of the Entatic State'. *Inorg. Chem.*, **2016**, 55 (22), 11694–11706.

2. S. Preiß, C. Förster, S. Otto, M. Bauer, P. Müller, D. Hinderberger, H. Hashemi Haeri, L. Carella, K. Heinze: 'Structure and Reactivity of a Mononuclear Gold(II) Complex'. *Nat. Chem.* **2017**, 9 (12), 1249–1255.

3. P. Zimmer, P. Müller, L. Burkhardt, R. Schepper, A. Neuba, J. Steube, F. Dietrich, U. Flörke, S. Mangold, M. Gerhards, M. Bauer: 'N-Heterocyclic Carbene Complexes of Iron as Photosensitizers for Light-Induced Water Reduction'. *Eur. J. Inorg. Chem.* **2017**, 2017 (11), 1504–1509.

4. P. Müller, K. Karhan, M. Krack, U. Gerstmann, W. G. Schmidt, M. Bauer, T. D. Kühne: 'Impact of finite-temperature and condensed-phase effects on theoretical X-ray absorption spectra of transition metal complexes'. *J. Comput. Chem.* **2018**, 5 (40), 712-716.

5. P. Zimmer, L. Burkhardt, A. Friedrich, J. Steube, A. Neuba, R. Schepper, P. Müller, U. Flörke, M. Huber, S. Lochbrunner, M. Bauer: 'The Connection between NHC Ligand Count and Photophysical Properties in Fe(II) Photosensitizers: An Experimental Study'. *Inorg. Chem.* **2018**, 57 (1), 360–373.

6. P. Müller, A. Neuba, U. Flörke, G. Henkel, T. D. Kühne, M. Bauer: 'Experimental and Theoretical High Energy Resolution Hard X-ray Absorption and Emission Spectroscopy on Biomimetic Cu_2S_2 Complexes'. *J. Phys. Chem. A* **2019**, accepted, DOI:10.1021/acs.jpca.9b00463

7. R. Meinhardt, P. Müller, P. Zimmer, X. Fu, Z. Jiang, A. Neuba, U. Flörke, M. Bauer: 'Structure-Activity Correlations among new Iridium(III) Photosensitizers in light driven water reduction', manuscript in preparation.

8. K. Stührenberg, P. Müller, L. Burkhardt, P. Dierks, U. Flörke, M. Bauer: 'Bis(2,9-dimethyl-1,10-phenanthroline) copper(I) complexes revised: A HERFD and V2C study of the model compound and the impact of halogen substituents'. manuscript in preparation.

9. M. Tünnermann, P. Rehsies, P. Müller, A. Neuba, U. Flörke and M. Bauer: 'Impact of diimine ligand modification on iridium complexes for the application in photocatalytic water reduction'. manuscript in preparation

Talks

1. P. Müller, M. Bauer: 'High Energy Resolution X-ray Absorption Spectroscopy and TD-DFT Calculations on Copper Systems'. Bunsentagung, Rostock, May 7, 2016.

2. P. Müller, M. Bauer: 'TD-DFT calculations of Cu K-edge (high energy resolution) X-ray absorption spectra'. Bioanorganisches Symposium, Aachen, September 2, 2016.

Poster

1. P. Müller, M. Bauer: 'Experimental and theoretical High-energy resolution X-ray absorption spectroscopy: Implications for the investigation of the entatic state'. Bioanorganisches Symposium, Sebtember 1-3, 2016.

2. P. Müller, M. Bauer: 'Experimental and theoretical High-energy resolution X-ray absorption spectroscopy: Implications for the investigation of the entatic state'. ORCA User Meeting, Sebtember 5-6, 2016.

3. P. Müller, M. Bauer: 'Experimental and theoretical High-energy resolution X-ray absorption spectroscopy: Implications for the investigation of the entatic state'. Koordinationschemie-Treffen, March 5-7, 2017.

4. P. Müller, M. Bauer: 'Experimental and theoretical High-energy resolution X-ray absorption spectroscopy: Implications for the investigation of the entatic state'. International Workshop on Photoionization & Resonant Inelastic X-ray Scattering, Aussois (France), March 26-31, 2017.

5. P. Müller, T. D. Kühne, M. Bauer: 'Experimental and theoretical High-energy resolution X-ray absorption spectroscopy'. International Conference on X-ray Absorption Fine Structure (XAFS), Krakow (Poland), July 22-27, 2018.

6. P. Müller, M. Bauer, T. D. Kühne: 'Experimental and theoretical High-energy resolution X-ray absorption spectroscopy'. Symposium on Theoretical Chemistry, Halle (Saale), September 17-20, 2018.

7. P. Müller, M. Bauer, T. D. Kühne: ‘Experimental and theoretical High-energy resolution X-ray absorption spectroscopy’. "Bring-your-own-poster"-session, JCF Paderborn, December 5, 2018. Awarded with the ‘Best Poster Award’ by the JCF PB.
8. P. Müller, M. Bauer, T. D. Kühne: ‘Experimental and theoretical High-energy resolution X-ray absorption spectroscopy’. PC^2 User Meeting, Paderborn, December 10, 2018.

Contents

Chapter 1: Introduction

1.1 Outline

Nature evolved a variety of systems capable of catalysing different reactions at ambient temperature and pressure despite rather high thermodynamic or kinetic barriers. Most of these reactions occur at a metal ion centre embedded in a protein scaffold and are therefore highly sensitive and specific, e.g. targeting one kind of functional group. Copper proteins are especially interesting concerning many electron transfer or redox processes, e.g. blue copper, type I enzymes or the Cu_A centre.[1–11] In addition to these naturally occurring forms where copper is mostly bound to sulfur, it has been shown that hard donor atoms like nitrogen possibly induce favourable properties regarding stability of the catalytic site. This and some differences in their spectroscopic signature lead to the classification of these compounds as 'type-zero'.[11–14] Mimicking properties of the aforementioned systems would be of great value for catalytic applications. Owing to the above-mentioned high barriers research efforts returned only limited success.

In order to achieve this goal, knowledge about involved mechanisms and the geometric and electronic structure of the metal site is crucial. Gathering this information experimentally is rather challenging. The first method that comes to mind regarding the geometry is X-ray single crystal diffraction. While this is the most established technique it can only be applied to crystalline samples as the name already suggests. But most of the aforementioned catalytic reactions occur in a solvent environment, which makes liquid sample spectroscopies a necessity at some point. A second problem is that intermediate species are hardly stable and cannot be crystallised or even concentrated in a sufficient amount. Despite all of the difficulties, techniques exist that are able to probe such systems.

X-ray absorption and emission spectroscopy (XAS and XES), especially with hard X-rays at energies $\geq$4-5 keV, can deliver a lot of the desired information. Several beneficial properties are attributed to hard X-rays. First of all, these techniques are element specific, because the core level electron energies between the elements are separated well enough. Secondly, hard X-rays are able to penetrate the sample and directly probe the metal centre, hardly limited by the surroundings or experimental conditions. This gives, in addition, a lot of possibilities for new cell designs and sample environments. Furthermore, no specific state of aggregation is required, i.e. it is possible to study solids, liquids and gases or combinations of those as needed.

While some information can be extracted directly from the experimental spectra, some additional details can only be gained by combining the experiment with theory. Since this is not always straightforward, especially regarding the state of aggregation, condensed phase effects, temperature and also the desired information have an impact on the choice of a computational method as well as the concomitant effort. These spectroscopic and some computational methods are therefore discussed in more detail in the following sections.

1.2 X-Ray Source

One of the single most important developments was the usage of synchrotron radiation as incident beam instead of conventional X-ray sources. This has made a lot of XAS and XES methods possible that were inaccessible before. One reason for that being the much higher flux of 10^3-10^6 more photons compared to an X-ray tube. Synchrotron facilities were originally used for high-energy physics experiments and the emission of synchrotron radiation was just a parasitic by-product due to the concomitant loss of kinetic energy. In a synchrotron charged particles are accelerated to a velocity close to the speed of light in a vacuum pipe with circular geometry. Their trajectory is enforced by vertically arranged magnetic fields and every time they are deflected from a straight path, electromagnetic radiation is emitted. Although this holds true for any kind of accelerated charged particle according to the Maxwell equations[15], most synchrotrons use electrons or positrons. Continuous acceleration due to the circular geometry induces continuously emitted radiation.[16]

Several beneficial properties of synchrotron radiation for X-ray spectroscopy lead to the development of second generation facilities in the 1970s solely for the purpose of generating and storing this kind of radiation. These synchrotrons use bending magnets (cf. Figure 1.1, left) to deflect the electrons, which are used because of their higher efficiency regarding the emission of radiation compared to other charged particles. The aforementioned flux, defined as the total number of photons per second, is only one of several parameters classifying an X-ray source. Two additional important quantities are intensity, given by the flux per area and brilliance. The latter one is defined as the number of photons for a given source area *and* angular divergence. A reduction of one parameter, e.g. smaller spatial size, leads to an associated increase of the second one. This invariance turns the brilliance into a very characteristic quantity, meaning that a brilliant source emits a high number of photons in a small area with small angular divergence.[16]

Third generation synchrotrons were then built aiming at even higher brilliance as well as better signal-to-noise ratios even for more demanding spectroscopic techniques. These facilities use so called insertion devices like undulators or wigglers (cf. Figure 1.1, right) in straight compartments pointing away from the ring. They differ in the wavelength λ_U, which describes the spatial period of the magnets.

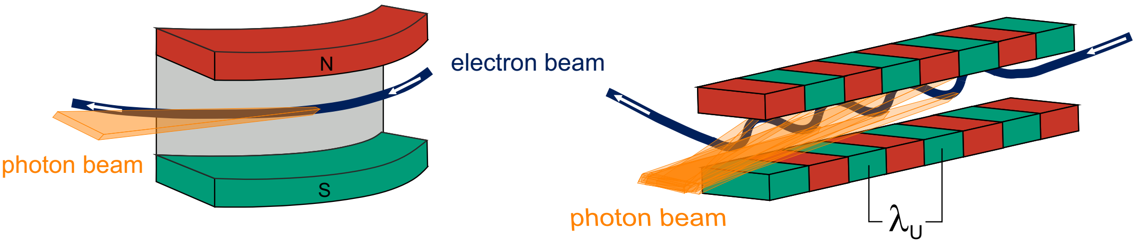

Figure 1.1: *Schematic of a bending magnet (left) and an insertion device (right). The spatial period* λ_U *is the main difference between undulators and wigglers and responsible for the different emittance of these two devices.*

In these devices electrons are forced on a wavelike trajectory with alternating magnetic fields close to each other. With every turn radiation is emitted and by tuning the distances between the magnets constructive interference can be achieved. This is the case in an undulator and leads to a narrow line spectrum. This in turn leads to higher brilliance which is necessary for e.g. high resolution emission techniques. In a wiggler the single radiation cones do not interfere and therefore the emitted spectrum is broad and continuous. Several orders of magnitude higher brilliance could be achieved compared to second generation synchrotrons.[17,18]

The most recent developments, i.e. fourth generation sources, are based on the free electron laser (FEL) technology and feature even higher brilliance. They are characterized by a narrow bandwidth and highly coherent, very short pulses. In combination with the high intensity and low repetition rates, these sources are perfectly suited and predominantly used in so called one-shot and time-dependent measurements.[17] This is possible because the intensity is high enough to generate a diffraction pattern in a single shot which can then be detected with a position sensitive detector. The only drawback of this very high intensity though is the instantaneous destruction of the sample. Fourth generation light sources are somewhat limited in their usage because of the incompatibility with standard XAS experiments. For these a broad bandwidth or tunable energy is mandatory.[16]

1.3 X-Ray Absorption Spectroscopy

Although the first X-ray absorption edges were measured a century ago,[19,20] it took a lot of time and discussion to really make it applicable. Especially the theoretical description was lacking for another 50 years.[21–24] Even today still a lot of development is ongoing, albeit not focussed on standard XAS measurements. A typical XAS spectrum can be roughly divided into three regions as shown in Figure 1.2.

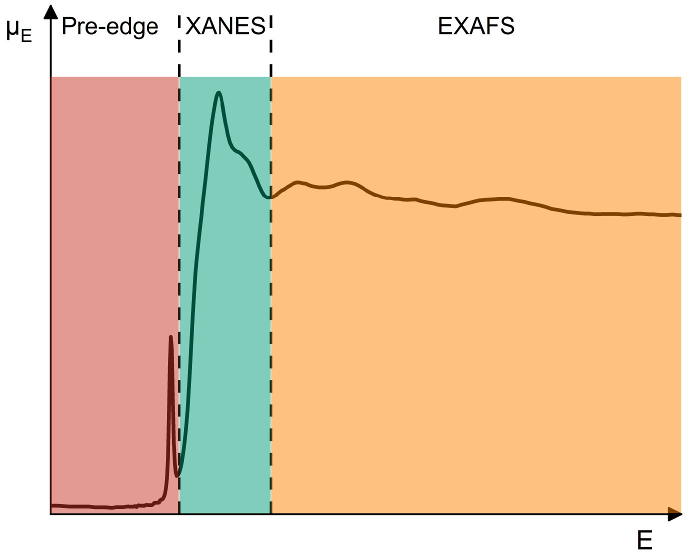

Figure 1.2: *A metal K-edge XAS spectrum depicting the division into three regions.*

Every region contains specific transitions of an electron from core levels to higher lying unoccupied states or ultimately to the continuum. For K-edge XAS the core orbital where an electron is excited from is the 1s orbital (cf. Figure 1.3).

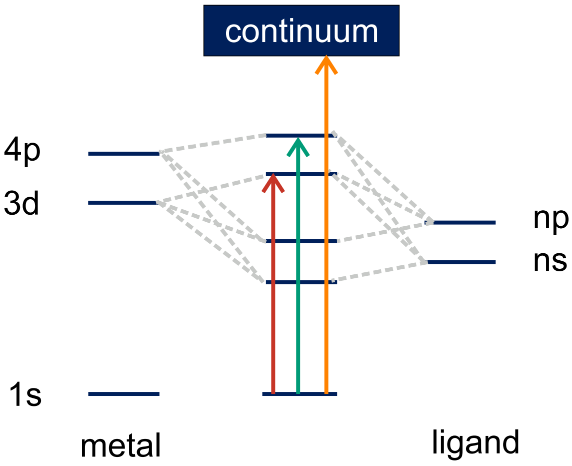

Figure 1.3: *Molecular orbital scheme of the transitions (arrows) occurring for the pre-edge (red), the XANES (green) and the EXAFS region (orange).*

The first part is called the pre-edge region and contains one or more prepeaks which arise from 1s to the lowest unoccupied molecular orbital (LUMO) transitions. Information about the oxidation state and the local geometry can be derived from this region. For 3d metals, like copper, the LUMO has contributions from the metal 3d orbitals and, depending on the geometry, differing amounts of ligand p orbitals. The intensity is rather low in most cases, which is due to the fact that it is governed by the dipole selection rule. Despite this, even transitions into rather pure 3d orbitals, e.g. in square planar geometry, have intensity which most probably stems from an electric quadrupole transition.[25] In geometries without centrosymmetry the admixture of ligand p orbitals increases and the intensity rises with it. Therefore the prepeak can also be used to determine the nd/(n+1)p hybridisation ratio which is sensitive to the geometry.[26] As mentioned above, the oxidation state can be derived as well. This can easily be explained by the copper example again. Since Cu(I) has a d^{10} configuration no prepeak will be visible. Oxidation of the copper ion and the concomitant change to a d^9 electron configuration will give rise to a prepeak. In addition to that a shift of this pre-edge feature to higher energy upon oxidation can be observed.[27]

Determination of the oxidation state can also be done via the edge energy in the second part of the spectrum, called edge or X-ray absorption near edge structure (XANES) region. The sharp rise in intensity is easily explained by dipole allowed transitions occurring at these energies. As already briefly mentioned the edge energy is specific for each element and in addition shifts to higher energies upon oxidation of the metal ion because of the more attractive positive potential of the nucleus. Determination of the oxidation state with this method can be problematic since higher lying unoccupied orbitals, e.g. metal 4p, can be populated and this gives rise to shoulders or peaks in the rising edge.

The third part of the spectrum is called the extended X-ray absorption fine structure (EXAFS) region and typically starts around 40 eV above the edge energy. With energies this high, the electron is excited into continuum states. The ejected photoelectron wave is scattered at surrounding atoms and interferes with the backscattered waves. This causes oscillations in μ_E. Since this fine structure is caused by the surrounding atoms it can be exploited by theoretical analysis and fitting procedures to give information about type, distance and number of atoms around the absorber.[16,28,29]

In a typical XAS experiment a sample is irradiated and the spectrum can be recorded in two ways. A scheme of the experimental setup is depicted in Figure 1.4.

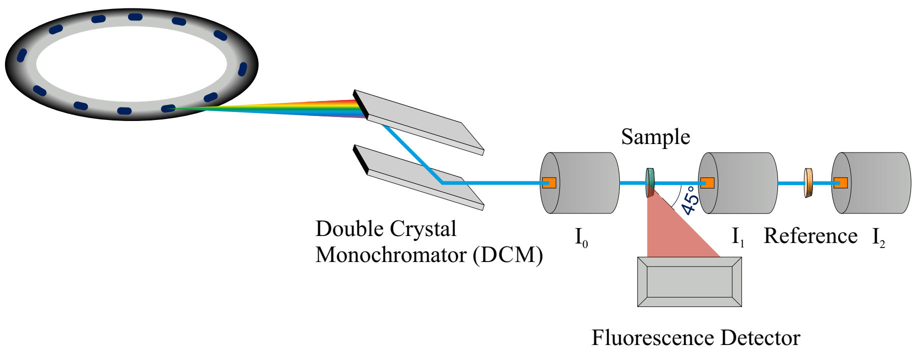

Figure 1.4: *Schematic assembly of a standard XAS experiment. Through measurement of a reference (usually a metal foil) and the sample simultaneously, energy drifts of the monochromator can be accounted for.*

Either the transmitted intensity after the sample is measured and the spectrum is calculated according to Lambert-Beer's law (cf. Equation 1.1).

$$\frac{I}{I_0} = e^{-\mu(E)x} \,, \tag{1.1}$$

with I and I_0 being the transmitted and incident intensity, x the path length through the sample and $\mu(E)$ the X-ray absorption coefficient. Or the emitted radiation following the absorption process, so called fluorescence, is measured by a solid state detector and then normalized to the incoming flux. For this the sample is turned to 45° and the detector is mounted 90° in respect to the beam and sample because this ensures maximum amount of photons detected. This approach is especially helpful to measure low sample concentrations and samples in environments that do not allow a measurement of the transmission due to thickness or too much absorption.

1.4 X-Ray Emission

Several techniques are based on the aforementioned fluorescence and are therefore summarized as X-ray emission spectroscopy. It is obvious that this is a two-step process. First a photon is absorbed and an electron is excited from a core state (cf. section 1.3) leaving a vacancy which is then filled with an electron from higher states. This relaxation process leads to radiative decay, i.e. the emission of a photon. Based on this, the phenomenon is a photon-in/photon-out process and therefore classified as X-ray scattering.[30] The electro-magnetic field A of the incoming photon can be described by a wave vector k and a polarisation ϵ. A perturbation Hamiltonian consisting of two terms can then be used to describe interaction with the sample. One is linear in A, i.e. $p \cdot A$ with p being the electron momentum operator, the other is quadratic in A. The latter vanishes in second order perturbation treatment since it is a one step scattering process and describes Compton, Thomson and Raman scattering. The more interesting term concerning X-ray emission is $p \cdot A$. In contrast this linear term only appears in second order treatment. It is needed to describe the process of reaching a final state with lifetime τ_f via an intermediate state with lifetime τ_n. These relations can be described by the resonant Kramers-Heisenberg formula since the cross-section of $p \cdot A$ is proportional to this term.[31–33]

$$F_{HK}(\omega_{in}, \omega_{out}) = \frac{\omega_{out}}{\omega_{in}} \sum_f \left| \sum_n \frac{\left\langle f \middle| \hat{O}'^{\dagger} \middle| n \right\rangle \left\langle n \middle| \hat{O} \middle| g \right\rangle}{E_n - E_g - \hbar\omega_{in} - i\Gamma_n} \right|^2 \frac{\frac{\Gamma_f}{\pi}}{\left(E_f - E_g - \hbar(\omega_{in} - \omega_{out})\right)^2 + \Gamma_f^2}, \qquad 1.2$$

with

$\hat{O}'^{\dagger} = \sum_{j'} (\epsilon^*_{out} \cdot p_{j'}) e^{-ik_{out} r_{j'}}$ transition operator,

$\hat{O} = \sum_j (\epsilon^*_{in} \cdot p_j) e^{-ik_{in} r_j}$ transition operator,

Γ_n, Γ_f lifetime energy broadenings of intermediate and final state,

$\omega_{in}, \omega_{out}$ angular velocities of the incoming and outgoing photons,

E_g, E_n, E_f energies of the ground, intermediate and final state respectively.

Only one ground, but all intermediate and final states are considered as well as all electrons in the scattering system. Two Lorentzian profiles are included as denominators. The first one is a complex description with the energy broadening Γ_n of the intermediate state. In turn, the final state lifetime is included in the second fraction where in addition the energy transfer needs to be equal to an energy difference in the system (resonance). One approximation can be made concerning possible interference effects which are allowed according to Equation 1.2. Since these do not change the transition energies, but only the intensities, they can be neglected leading to Equation 1.3.

$$F_{HK}(\omega_{in}, \omega_{out}) \approx \frac{\omega_{out}}{\omega_{in}} \sum_f \sum_n \frac{\left| \left\langle f \middle| \hat{O}'^{\dagger} \middle| n \right\rangle \right|^2 \left| \left\langle n \middle| \hat{O} \middle| g \right\rangle \right|^2}{(E_n - E_g - \hbar\omega_{in})^2 - \Gamma_n^2} \times \frac{\frac{\Gamma_f}{\pi}}{\left(E_f - E_g - \hbar(\omega_{in} - \omega_{out})\right)^2 + \Gamma_f^2} \qquad 1.3$$

Here, the cross-section is proportional to the product of absorption and emission probabilities. This formula is used as the theoretical description of various scattering techniques including resonant X-ray emission spectroscopy (RXES), resonant inelastic X-ray scattering (RIXS) and high energy resolution fluorescence detected (HERFD) XANES as will be explained later. Even standard XAS in transmission could be described since it can be seen as forward scattering with an angle of zero.

Depending on the origin of the electron filling a core hole, or specifically the 1s hole for K-edges, X-ray emission can be classified (cf. Figure 1.5).

The lowest energy emission for K-edges is called Kα (cf. Figure 1.6, red) where the 1s vacancy is filled by a 2p electron. Since there is a splitting into 2p$_{1/2}$ and 2p$_{3/2}$ two distinguishable features Kα_1 and Kα_2 are measured. This type of emission has the

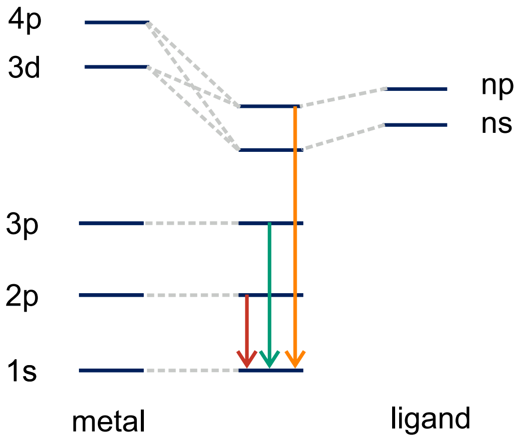

Figure 1.5: *Molecular orbital scheme of transitions occurring for different emission processes. Depending on this XES spectra can be classified into* K_a *(red),* K_β *(green) and Valence-to-Core (VtC, orange).*

highest intensity since the transition probability is higher than for the other cases.[34] Despite this fact it was not used further in this work as an emission technique because of the limited chemical insight aside from minor spin sensitivity. This stems from the fact that the 2p orbitals are spatially and energetically separated from the valence orbitals.[35] Nonetheless it can be used to collect *HERFD-XANES* spectra which will be explained later.

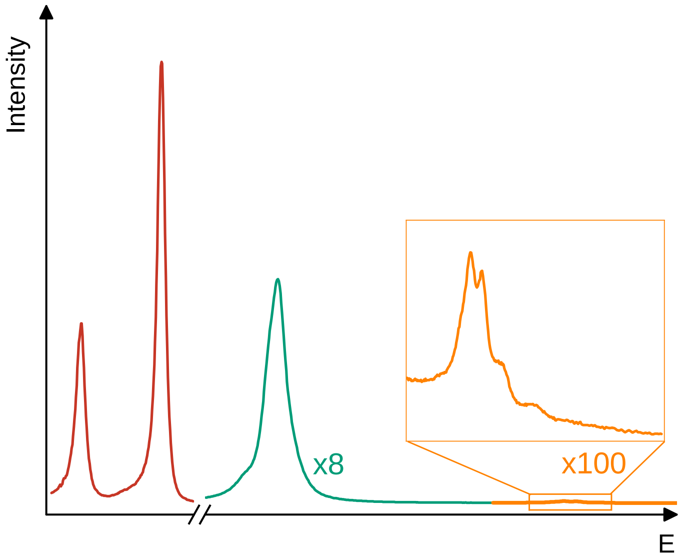

Figure 1.6: *Example spectra for the aforementioned transitions* $K\alpha_1$ *and* $K\alpha_2$ *(red)* $K\beta$ *(green) and Valence-to-Core (orange, inset).*

The following transition is the so called Kβ (cf. Figure 1.6, green) emission which corresponds to a 3p → 1s transition. Information about the oxidation state (energy shift) and the spin can be extracted. There are two prominent spectral features depending on the spin state, namely the intense higher energy $K\beta_{1,3}$ and the weaker $K\beta'$ signal. The latter one is induced by 3p-3d exchange interaction. Reducing the spin state leads to the features moving closer in energy as can be seen in Figure 1.7. Chemical sensitivity can therefore be achieved although only indirect since it is still a core-to-core phenomenon and does not probe valence orbitals directly. In contrast to the aforementioned Kα emission there is no splitting of the 3p orbitals visible. This stems from the fact that the 3p-3d exchange interaction dominates the spectral shape instead of the 3d or 3p spin-orbit coupling.[31,36] Different effects depending on the valence electron configuration and thus the spin state affect the spectral features. One thing to consider is the valence charge density which depends on the effective number of 3d electrons and thereby on the oxidation state of the metal ion. This in turn effects the screening of the core hole potential. Another contribution to the valence charge density can be attributed to the degree of covalency, since this is influenced by the delocalisation of an electron cloud between metal ion and ligand. All these effects lead to an observable shift of the K$\beta_{1,3}$ feature. *Glatzel* showed that this can be attributed to variations in the 3p-3d exchange splitting, and not to changes of the nuclear screening.[37] Having said that, the amount of information for this work is limited since it focusses around copper compounds with oxidation states of +1 (d^{10}) and +2 (d^{9}).

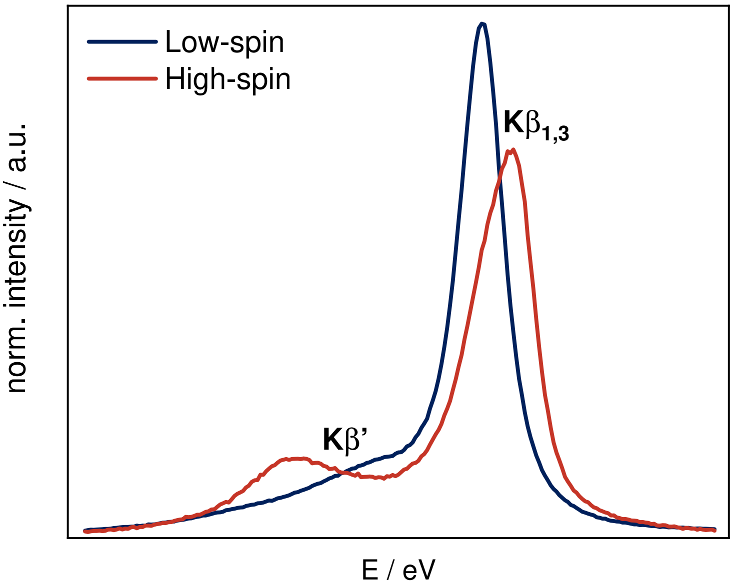

Figure 1.7: *Core-to-Core emission spectra of iron compounds in LS and HS state.*

Chemically most sensitive is the Valence-to-Core emission, which, as the name suggests, directly probes valence orbitals, i.e. highest occupied molecular orbitals (HOMOs), of a given compound.[31,36,38–43] In case of transition metals it is formally a $3d \rightarrow 1s$ relaxation process which is dipole forbidden (cf. XANES pre-edge region) and therefore ~100 times weaker than the K$\beta_{1,3}$ feature. Since the transition intensity depends on the nd/(n+1)p hybridisation (cf. section 1.3) it is also sensitive to the coordination geometry.[43] Generally the spectrum consists of the K$\beta_{2,5}$ line at higher energies and lower lying, weaker Kβ'' (cf. Figure 1.8) features. These Kβ'' or

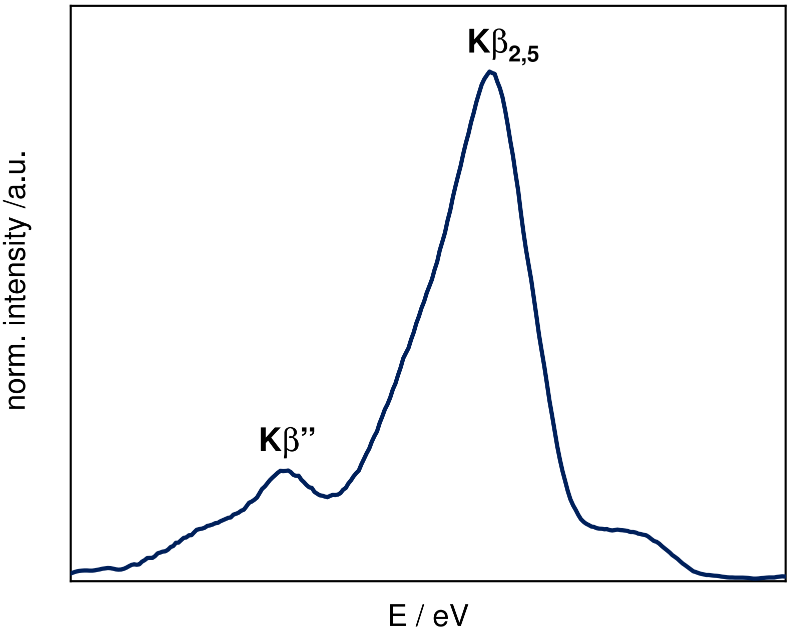

Figure 1.8: *Example Valence-to-Core emission spectrum showing the* $K\beta_{2,5}$ *and* $K\beta''$ *features.*

cross-over transitions are typically caused by electron relaxation from 2s or 3s ligand orbitals to metal 1s. These features are shifted approximately by the 2s/3s binding energy and are therefore very sensitive to the ligand environment.[36,38] In contrast to other X-ray techniques, e.g. EXAFS spectroscopy or X-ray single crystal diffraction, it is even possible to differentiate between light atoms like carbon, nitrogen and oxygen.

As already mentioned briefly any of these emission lines can be used to collect HERFD absorption spectra.[44,45] This method allows to sharpen the features compared to a standard measurement (as demonstrated in Figure 1.9) and thereby give additional information, especially in conjunction with calculations.[46–48] One of the most significant advantages is the better separation of the pre-peak from the edge which can give information about local geometry and oxidation state (cf. section 1.3). This advantage stems from the fact that fluorescence is a second order process described by the Kramers-Heisenberg formula (cf. Equation 1.3). The obtainable resolution in a XAS experiment is limited by the lifetime broadening of the final state due to *Heisenberg's* uncertainty principle. Since for K-edges the very short lifetime of the 1s core hole is the determining factor, the energy broadening is large. To circumvent this issue the aforementioned HERFD technique is used where the intensity is collected via fluorescence detection. In contrast to a standard measurement, in which the intensity is integrated over all fluorescence lines, only a single narrowly chosen decay channel is monitored. For this to work the instrumental resolution has to be smaller or equal to the natural lifetime broadening of the selected emission line. By doing this, the aforementioned final state is no longer the 1s, but a

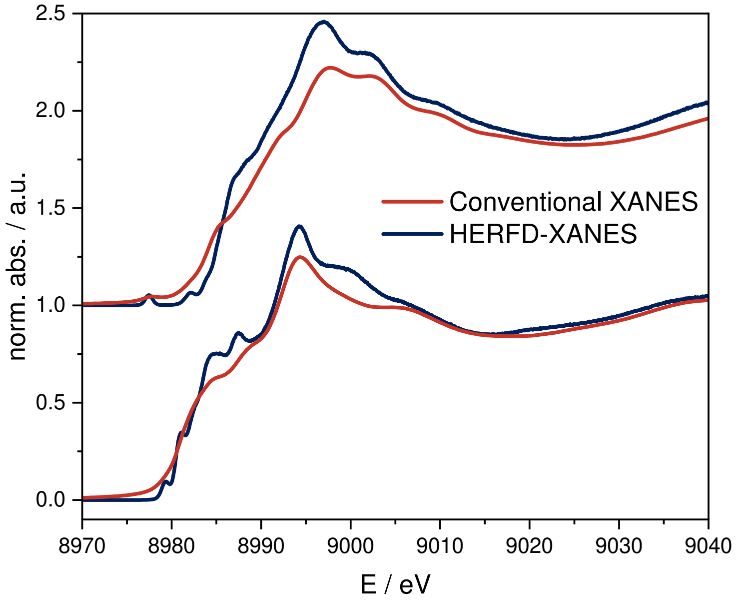

Figure 1.9: *Comparison of conventional and HERFD-XANES spectra of a* Cu^{1+} *(bottom) and a* Cu^{2+} *(top) compound.*

2p (Kα) or 3p(Kβ) core hole which have significantly longer lifetimes and thereby a reduced energy broadening.

All of the above-mentioned techniques are recorded in high resolution by using analyser crystals. There are two major types of spectrometer geometries using reflection, a scanning-type and a dispersive one. The functional principle and differences are explained in the following.

The basis for all of these methods and instrumentations is the diffraction of X-rays according to the Bragg Law (cf. Equation 1.4)

$$n\lambda = 2d\sin(\theta), \tag{1.4}$$

where n is the diffraction order, λ is the X-ray wavelength, d is the lattice constant and θ the Bragg angle.

It describes the correlation of a photon with given energy (wavelength) being reflected at only one angle θ. In reality though, the reflected radiation is dispersed to a range of angles around the theoretical value. As a consequence there is an angular width $\Delta\theta$, the so-called *Darwin width*, fulfilling the aforementioned condition. If working in backscattering geometry, i.e. at an angle of 90°, this goes to zero and therefore this geometry is tried to be realized in any practical application. This contributes to the possible energy resolution according to the derivative of the Bragg equation (cf. Equation 1.5).[49]

$$\frac{\mathrm{d}E}{E} = \mathrm{d}\theta\cot(\theta) \tag{1.5}$$

The most widely used scanning geometry is based on a Rowland circle according to *Johann* and *Johansson*.[50,51] A beam originating from a fixed point on the circle is reflected onto the detector under the same Bragg angle on every point of the circle. Most widely applied is the *Johann* approach where sample, detector and bent analyser crystal with radius 2R are fixed on a circle with radius R. These different radii mean that only the central point of the surface lies on the Rowland circle. This is the so-called Johann aberration which is negligible if working close to backscattering geometry ($\theta = 90°$). To increase the covered solid angle and thereby the collected amount of photons multiple crystals with overlapping Rowland circles can be used (cf. Figure 1.10). In the original geometry crystals were bent cylindrically along the Rowland circle.[50] These days mostly spherically bent crystal analysers are used. Since the Rowland circle condition has to be fulfilled the analyser crystals and the detector are motorised and can be moved around, while the sample is fixed.

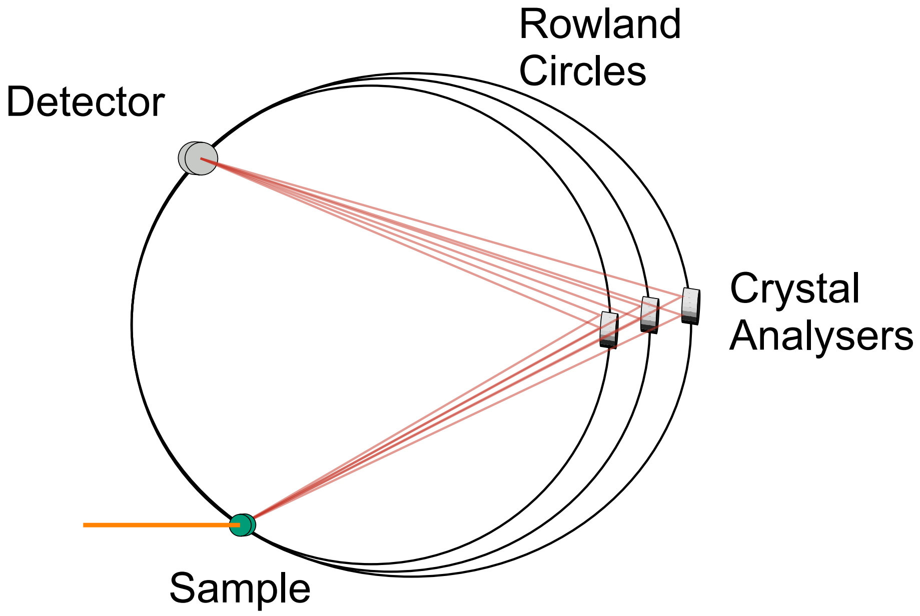

Figure 1.10: *Scheme of a point-to-point scanning type spectrometer geometry with three Rowland circles.*

Johansson introduced a slightly modified setup which differs in the preparation of the crystal analysers.[51] Instead of only bending them to the radius of 2R they are also ground to the radius R of the Rowland circle. This ensures precise focussing since the entire crystal surface lies exactly on the Rowland circle. Thereby it also enables geometries differing from the backscattering angle since there is no variation of the incident photon angles across the crystal surface. Therefore it is the advantageous setup when going to lower energies (1.5 - 3 keV). In this case smaller Bragg angles are inevitable and no appropriate crystal analysers with angles $> 70°$ are available.[31]

In contrast to scanning point-by-point the energy a wavelength dispersive setup can be used, allowing to record an entire spectrum in one shot. This is achieved by using optical elements that diffract X-rays over a range of Bragg angles simultaneously and then concomitantly record the intensity with a position sensitive detector.[31] Thereby time-dependent measurements with low time resolutions become feasible which are especially interesting for catalytic or excited state investigations in a pump-probe scheme. The simplest assembly uses a flat crystal as optical element but it does not allow for high-resolution while collecting a large solid angle. To circumvent this issue the *von Hamos* geometry[52,53] can be used which is based on cylindrically bent crystal analysers (cf. Figure 1.11). These combine the high-energy resolution advantage of a flat crystal with a large solid angle assigned with a bent (curved) crystal. X-rays emitted on these crystals are diffracted and focussed according to the Bragg Law (cf. Equation 1.4).

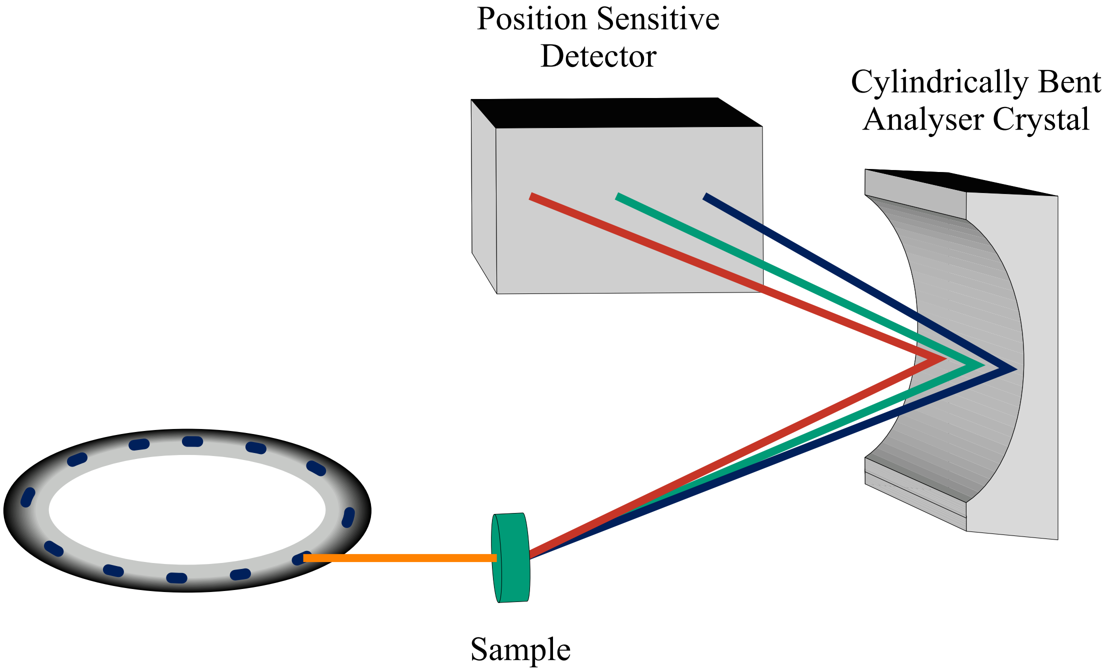

Figure 1.11: *Scheme of a von Hamos spectrometer geometry using only one analyser crystal.*

1.5 Density Functional Theory

The foundation of density functional theory (DFT) was laid down in the 1920's by Thomas and Fermi, who postulated a functional correlation between the properties of a molecule and its electron density ρ.[54,55] Since then DFT, and its time dependent counterpart, have become widely applicable methods in computational chemistry.[56–60] The first approaches were too strongly simplified though and did not describe for example molecular bonds. It was not until 1964 when Hohenberg and Kohn proved that the drastic simplification to a one particle problem (from N interacting particles) was indeed exact and viable.[61]

With the Born-Oppenheimer approximation[62] in mind one can write

$$E[\rho(r)] = T[\rho(r)] + V_{en}[\rho(r)] + J[\rho(r)] + Q[\rho(r)], \tag{1.6}$$

with

$T[\rho(r)]$ kinetic energy of the electrons,

$V_{en}[\rho(r)]$ nuclear-electron attraction energy,

$J[\rho(r)]$ classical electron-electron repulsion energy,

$Q[\rho(r)]$ quantum (non-classical) electron-electron interaction.

The two terms $V_{en}[\rho(r)]$ and $J[\rho(r)]$ are known and can be computed according to the following equations:

$$V_{en}[\rho(r)] = -\sum_{A=1}^{M} \int \frac{Z_A}{|r - R_A|} \rho(r) dr, \tag{1.7}$$

$$J[\rho(r)] = \frac{1}{2} \int \int \frac{\rho(r_1)\rho(r_2)}{r_{12}} dr_1 dr_2, \tag{1.8}$$

The most significant unknown term is the kinetic energy and the description or accurate approximation is a difficult task, which was not solved satisfactorily. Kohn and Sham then presented a theoretical approach that turned out to be the foundation of modern DFT.[56,63] They showed that the kinetic energy could be approximated accurately by using a fictitious system of non interacting electrons with the same density as the real system. This is achieved by calculating the kinetic energy via a single slater determinant of orbitals ϕ_i (cf. Equation 1.9).

$$T_s[\{\phi_i\}] = -\frac{1}{2} \sum_{i=1}^{n} \int \phi_i^*(r) \nabla^2 \phi_i(r) dr \tag{1.9}$$

Since T_s is obviously different to T and Q is unknown as well these two terms are combined in the exchange-correlation functional E_xc.

$$E_{xc}[\rho(r)] = T[\rho(r)] - T_s[\{\phi_i\}] + Q[\rho(r)] \tag{1.10}$$

This functional is unknown and a lot of effort went into the construction of various types of functionals that approximate the values as accurate as possible.[56]

Since molecular orbitals ϕ_i are unknown and complicated[64,65] they have to be expanded by means of known functions χ_μ (cf. Equation 1.11).

$$\phi_i = \sum_{\mu} c_{\mu i} \chi_\mu \tag{1.11}$$

In this fashion the problem is reduced to finding a set of numbers to describe a previously unknown function.[66] There are two popular representations for the description of orbitals, namely the Gaussian and the plane wave basis. The first one is especially used in quantum chemistry and the functions are of the following form:

$$\chi_m = N_m r_x^{m_x} r_y^{m_y} r_z^{m_z} e^{\left[-\zeta r^2\right]}, \tag{1.12}$$

with the parameter set $N_m, m_x, m_y, m_z, \zeta$ and the angular momentum quantum number m.[67] They are widely used because these functions are intended to mimic atomic orbitals[67] and are constructed to model the quantum states of the atomic wave function.[68] This is beneficial for the mostly orbital based view on molecules in chemistry. A second approach, largely used in solid state physics, are plane waves. They are predominantly used in this field because of their inherent delocalisation and periodicity, which is optimally suited to describe periodic systems like crystals. They are simply constructed by a wave vector G and an expansion coefficient $n_i(G)$ (cf. Equation 1.13).

$$\phi_i = \sum_G n_i(G) e^{iGr} \tag{1.13}$$

In this work both approaches are used in different fashions because both suit a specific purpose. Concerning the calculation of X-ray spectra a proper description of localized core and valence orbitals is needed for the pre-edge and edge part of the spectrum and Gaussian type orbitals are well suited to tackle this. Additionally for higher energy parts a more delocalised description is beneficial and therefore a plane wave approach is chosen.

There are several ways of using DFT and TD-DFT to calculate X-ray absorption and emission spectra. The easiest but nonetheless very valuable approach is to simply take orbital differences between the donor and acceptor orbitals from a ground state DFT calculation.[41] It is shown that this works very well for VtC-XES. In case of XAS at least a core excited state should be taken into account. This is for example achieved by calculating the wave function of this state and then calculate transitions accordingly.[69] Or by using TD-DFT for the calculation of transitions as done for UV/Vis but by limiting the donor space to the 1s orbital (in case of K-edge spectroscopy).[70,71] Obviously there are a lot more approaches but these are the basic ideas of the ones that were used for this work.

1.6 Ab-initio Molecular Dynamics

Since a plethora of chemical reactions in nature as well as in the laboratory occur in solution the proper description of weakly interacting systems is necessary. This especially means that the equilibrium structure is not sufficient for the calculation of properties because the potential well can be overcome even at room temperature. Therefore it is mandatory that all configurations other than the 0 K equilibrium have to be taken into account with their appropriate statistical weight.[72] One method to accomplish this is molecular dynamics (MD),[72,73] in this case the ab-initio approach specifically, which will shortly be presented.

The first thing to mention here is that the nuclei are described classically while the electrons are treated quantum mechanically (in contrast to standard MD where everything is treated classically). The basic idea is to move the particles according to Newtons equations of motion.

$$\dot{R} = \frac{\partial \mathscr{H}}{\partial P} \; and \; \dot{P} = \frac{\partial \mathscr{H}}{\partial R}, \tag{1.14}$$

where $\mathscr{H} = T + V$ denotes the Hamiltonian or total energy and $\dot{R}$ and $\dot{P}$ are the time derivatives of the positions and momenta in the given system.

The forces on the particles are then evaluated quantum mechanically. One question that immediately arises is how to calculate the wave function after every time step of such a simulation. One way, although a very costly one, would be to calculate the electronic structure iteratively after each time step following the potential energy surface of the ground state, i.e. optimize the system each step. This approach is known as Born-Oppenheimer MD (BOMD). Despite efforts to make it more efficient this method only had limited success due to the cost, especially since techniques to transfer electronic information from one step to the next were absent.[67,74]

Another more efficient way was proposed by Car and Parrinello in 1985 (CPMD) as a combination of DFT and MD.[75] In contrast to BOMD the electronic information is propagated instead of being optimised. This is achieved with an extended-Lagrangian method and the introduction of a fictitious electron dynamic.

$$\mathscr{L}(R,\phi) = \frac{1}{2}\sum_I M_I \dot{R}_I^2 + \frac{1}{2}\sum_i \mu \frac{\partial}{\partial t} \langle \phi_i \,|\, \phi_i \rangle - V(R,\phi), \tag{1.15}$$

with $\mathscr{L}$ being the Lagrangian, ϕ an orthonormal set of molecular orbitals, V the potential energy and M as well as μ the atomic mass and a fictitious electron mass respectively. The aforementioned propagation leads to high electron resonance frequencies though which in turn requires very short time steps for successful calculations.[76]

A similar approach, termed second generation CPMD, was presented by Kühne et al. in 2007[77] which allows timesteps as large as in BOMD. The *always stable predictor-corrector* (ASPC) method by Kolafa[78] is used to propagate the electronic information. In the original work a wave function is extrapolated in a polynomial of order K with the K+1 previous wave functions as support, whereas in the adaptation the density was chosen instead (cf. Equation 1.16). The reasoning is that it evolves far more smoothly than the wave function.[76]

$$C^P(t_n) \cong \sum_{m=1}^{K} (-1)^{m+1} m \frac{\binom{2K}{K-m}}{\binom{2K-2}{K-1}} \underbrace{C(t_{n-m})C^T(t_{n-m})}_{P(t_{n-m})} \times S(t_{n-m})C(t_{n-1}), \tag{1.16}$$

Here, the density of time step t_n is extrapolated using the K+1 previous densities and then transformed back to the wavefunction with $C(t_{n-1})$. Since this step is not exact, the error is added to the one made in the extrapolation.[77] In order to reduce this error as much as possible, a corrector step is implemented after the predictor step as follows. If this corrector step is applied to convergence the method turns into a BO approach.

$$\begin{gathered} C(t_n) = \omega \,\mathrm{MIN}[C^P(t_n)] + (1-\omega)C^P(t_n), \\ \text{with } \omega = \frac{K}{2K-1} \text{ and } K \geq 2 \end{gathered} \tag{1.17}$$

Preceding this is a matrix purification step.[79] It is necessary to restore the orthonormality of the molecular orbitals, which is violated due to the approximative extrapolation (Equation 1.16). In order to avoid iteration to convergence, the error made calculating the forces is assumed as a random noise Ξ_I acting on the converged forces F_{BO}. The additive white noise Ξ_I and the dissipative behaviour can be compensated using a modified Langevin equation with the damping coefficient γ.

$$M_I\ddot{\mathbf{R}}_\mathbf{I} = F_I^{BO} - \gamma M_I \dot{\mathbf{R}}_\mathbf{I} + \Xi_I \tag{1.18}$$

The unknown damping parameter γ is evaluated in a preliminary run and then fixed.[76]

These are just some basics of DFT and AIMD and the computational details can be found in the respective publications.

Chapter 2: Experimental and Theoretical X-Ray Absorption Spectroscopy on Cu(DMEGqu)

The Cu(I) / Cu(II) pair of complexes with the hybrid guanidine-quinoline ligand is investigated by means of HERFD-XANES measurements as well as time dependent density functional theory (TD-DFT), gauge-including projector-augmented-wave(GIPAW) and Gaussian augmented plane wave (GAPW) calculations.

The first study (TD-DFT/GIPAW) mainly focusses on geometric parameters and identification of features in the spectrum showing that even small geometric and electronic changes can be revealed. This is especially important for so called Entatic State systems that change their geometry upon oxidation but still have strong resemblance.

The second work uses a GAPW XAS approach in combination with AIMD to study the impact of condensed-phase and finite-temperature effects on the X-ray absorption spectra. In addition a theoretical outlook is given for the effects of solvation on X-Ray absorption spectra.

2.1 Implications for the Investigation of the Entatic State

Participations in this Publication

N. J. Vollmers, M. Rohrmüller, U. Gerstmann & W. G. Schmidt — Quantum Espresso Calculations

A. Hoffmann & S. Herres-Pawlis — Synthesis and provisioning of the samples

P. Müller & M. Bauer — HERFD-XANES measurements, ORCA calculations and concomitant orbital analysis

Reprinted with permission from **Experimental and Theoretical High-Energy-Resolution X-ray Absorption Spectroscopy: Implications for the Investigation of the Entatic State**
Nora Jenny Vollmers, Patrick Müller, Alexander Hoffmann, Sonja Herres-Pawlis, Martin Rohrmüller, Wolf Gero Schmidt, Uwe Gerstmann, and Matthias Bauer, *Inorganic Chemistry* **2016** 55 (22), 11694-11706, DOI:10.1021/acs.inorgchem.6b01704.

Inorganic Chemistry
Article
pubs.acs.org/IC

Experimental and Theoretical High-Energy-Resolution X-ray Absorption Spectroscopy: Implications for the Investigation of the Entatic State

Nora Jenny Vollmers,[†,§] Patrick Müller,[‡,§] Alexander Hoffmann,[⊥] Sonja Herres-Pawlis,[⊥] Martin Rohrmüller,[†] Wolf Gero Schmidt,[†] Uwe Gerstmann,[*,†] and Matthias Bauer[*,‡]

[‡]Department Chemie and [†]Department Physik, Universität Paderborn, Warburger Straße 100, D-33098 Paderborn, Germany
[⊥]Institut für Anorganische Chemie, RWTH Aachen University, Landoltweg 1, D-52074 Aachen, Germany

Ⓢ *Supporting Information*

ABSTRACT: High-energy-resolution-fluorescence-detected X-ray absorption near-edge structure (HERFD-XANES) spectroscopy is shown to be a sensitive tool to investigate the electronic changes of copper complexes induced by geometric distortions caused by the ligand backbone as a model for the entatic state. To fully exploit the information contained in the spectra gained by the high-energy-resolution technique, (time-dependent) density functional theory calculations based on plane-wave and localized orbital basis sets are performed, which in combination allow the complete spectral range from the prepeak to the first resonances above the edge step to be covered. Thus, spectral changes upon oxidation and geometry distortion in the copper *N*-(1,3-dimethylimidazolidin-2-ylidene)quinolin-8-amine (DMEGqu) complexes $[Cu^I(DMEGqu)_2](PF_6)$ and $[Cu^{II}(DMEGqu)_2](OTf)_2\cdot MeCN$ can be accessed.

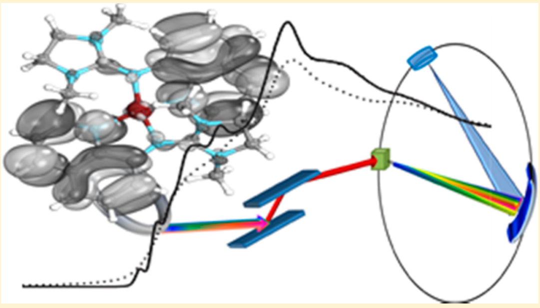

INTRODUCTION

Copper plays a central role in many electron-transfer (ET) processes in nature.[1] Blue copper, or type I, proteins span a large window of reduction potentials, which leads to a variety of possible ET partners.[1,2]

Although in nature copper is mostly bound to sulfur in such proteins, it was already reported that hard donor atoms also work in biomimetic ET systems with possibly advantageous properties regarding lifetimes of the catalytic site.[3] These nonblue systems exhibit ET features similar to those of type I proteins, but without sulfur donors and having a broader axial electron paramagnetic resonance hyperfine splitting, leading to the name "type-zero" compounds. The geometrical distortion between cuprous and cupric sites plays a central role for the efficiency of such ETs. Studying copper type-zero complexes with nitrogen-donor ligands using X-ray spectroscopic and theoretical techniques can therefore significantly contribute to the understanding of copper-mediated ET processes.

The ability to tune the Cu^I/Cu^{II} redox couple is crucial not only in nature but also for catalytic applications of biomimetic complexes. The reduction potential of the Cu^I/Cu^{II} redox pair is influenced by the electronic and structural parameters at the copper coordination site. In particular, the inner coordination sphere is dominating these parameters and has been subjected to many studies.[4−6] In the case of enzymes, those constraints are caused by the protein backbone, leading to a situation named rack-induced or entatic state, which facilitates ET from the kinetic point of view.[7,8]

In such states, deviations from the geometry obtained by ligand-field theory appear. Considering the Cu^I/Cu^{II} redox couple, the according geometries would be square-planar for Cu^{II} and tetrahedral for Cu^I. Changes in the redox state require therefore a change in the coordination symmetry. Any (even small) geometry deviation from the ligand-field limit facilitates the interconversion of the Cu^I/Cu^{II} redox states, enabling exceptionally fast ET. In the last years, many efforts have been invested in the synthesis of conformationally invariant copper(I/II) complexes as model complexes for the entatic state, but good models are still rare,[7,9−15] and the nature of the resulting entatic state is controversially discussed.[16−18] While some authors favor an electronic entatic state,[13] others claim geometric strain by the ligands to be the origin of the deviation from the theoretical ligand-field geometry.

It is thus a mandatory task to access experimentally the electronic (d-electron density) and geometric (arrangement of coordinating ligands) structures at the copper center to further understand the working principle of entatic model complexes. Single-crystal diffraction is surely the working horse for this purpose. However, it cannot be applied in the in situ

Received: July 20, 2016
Published: November 4, 2016

DOI: 10.1021/acs.inorgchem.6b01704
Inorg. Chem. 2016, 55, 11694−11706

environment of biomimetic compounds, i.e., in solution. Here, only short-range sensitive methods will give the desired information.

X-ray absorption spectroscopy (XAS) is the only element-specific method to achieve this aim. If hard-X-ray XAS at the copper K-edge is used, it has the advantage of delivering geometric and electronic structural parameters independent of the sample environment and can therefore be applied also under biorelevant in situ conditions.[19] Many successful applications of XAS on biomimetic copper complexes and related systems are known in the literature. They mainly focus on the structure information in the extended X-ray absorption fine structure (EXAFS) spectra.[20−22] These studies underline the spectroscopic prowess of XAS in this context. However, the full potential of the X-ray absorption near-edge structure (XANES) region, in which details about both the geometric (backscattering) and electronic (orbital contributions) situations are contained, could not be fully used. This is due to the lifetime broadening of the 1s electron−hole after K-edge excitation.[23,24] This broadening limits the extraction of information from the preedge peak and XANES region significantly.[25] Both spectral parts are broadened in such a way that details of the lowest unoccupied molecular orbital (LUMO) states above the Fermi level, which are highly sensitive to geometric changes, are masked and the characteristic first resonances after the edge are smeared out.[23]

The recent development of high-energy-resolution-fluorescence-detected XANES (HERFD-XANES) offers a powerful tool to overcome this limitation.[23] With this method, the lifetime broadening effect can be reduced significantly, and the fine structure in the prepeak and XANES spectra can be resolved. This allows a detailed comparison with theoretical calculations.

However, the computational XANES modeling faces a variety of challenges. On the one hand, the requirement to treat core−hole excitations renders the straightforward application of pseudopotential methods difficult. All-electron calculations, which appear particularly suitable for describing XAS, suffer from significantly larger computational costs than those required by pseudopotential-based methods. On the other hand, the description of excited states is, strictly speaking, beyond the realm of density functional theory (DFT), the method of choice for the description of complex structures. DFT neither accounts for the quasiparticle character of the electrons nor describes electron−hole attraction effects. There are well-founded and successful strategies[26] to overcome these limitations, e.g., the GW approximation for the electronic self-energies, where they are expressed as a convolution of the single-particle propagator G and the dynamically screened Coulomb interaction W, and the Bethe−Salpeter equation (BSE) approach to describe Coulomb-coupled electron−hole pairs.[27] However, these methodologies are prohibitively expensive for complex structures. In particular, far-edge regions cannot be easily computed within GW-BSE. Obviously, electron correlation methods such as coupled-cluster (CC) theory also give accurate access to excited states and thus can be used to determine X-ray excitations.[28−30] Again, the method is highly expensive, even if multilevel coupled-cluster (MLCC) implementations appear promising.[31]

Time-dependent DFT (TD-DFT) is numerically less demanding and thus presently the method of choice to address charge-neutral excitations in complex molecules. It is also frequently used to determine core excitations.[32−35] This approach is well-founded in principle, but the complication is hidden in the unknown time-dependent exchange and correlation (XC) potential that appears in the Kohn−Sham equations. Most numerical implementations rely on the adiabatic approximation, which often proves successful for finite systems such as molecules but fails for extended systems such as solids.[36] Constrained and orthogonality constrained density functional theories (cDFT[37] and OCDFT[38,39]) are possible alternative approaches to excited-state configurations.

A third difficulty in simulating XAS data is related to the basis set used to expand the electronic wave functions. Localized basis functions such as Gaussians are computationally efficient and do thus allow for the modeling of core electrons as well as many-body effects, e.g., by means of TD-DFT, even for comparatively complex structures; see., e.g., ref 40. However, they do not form a complete set and are not suitable for the description of excited high-energy states that typically are fairly delocalized. Plane waves, on the other hand, form by the construction of a complete and orthogonal basis set, the numerical convergence of which can be smoothly varied and reliably controlled. Moreover, plane waves are ideally suited to describe delocalized high-energy states as well as systems with periodic boundary conditions such as molecular crystals.[41] Naturally, the description of core states with plane waves is cumbersome.

In order to deal with these complications, we use two different and to some extent complementary theoretical approaches to simulate XANES: On the one hand, for molecular species, we use TD-DFT with a localized orbital basis set that is expected to be particularly suitable for the description of preedge peaks.[42] On the other hand, we used the continued-fraction expansion of Green's function[43−45] in conjunction with a plane-wave basis set, which appears particularly suited for solids, e.g., molecular crystal structures.[46] Here, the incorporation of the 1s core−hole into pseudopotentials[47,48] allows for a computationally very efficient cDFT-like description of excitonic effects involving core states[49] and also K-edge XAS spectra in a broad energy range. It has been used to describe the prepeak region of copper compounds[50] but results in a particularly reliable description of near- and far-edge features of the absorption spectrum.[47,51−55]

Consequently, the purpose of this work is 3-fold: (i) to establish HERFD-XANES as a new high-resolution method to investigate copper-based biomimetic systems, (ii) to elucidate the capability of TD-DFT and the continued-fraction approach to simulate and rationalize such spectra, and (iii) to show that a combined application of these schemes is able to unravel many details of the molecular geometries, which can be used to answer questions related to the entatic state principle in biomimetic systems. As a prototype example for such systems, we use a pair of copper(I) and copper(II) complexes formed by the quinoline-based ligand *N*-(1,3-dimethylimidazolidin-2-ylidene)quinolin-8-amine (DMEGqu), namely, $[Cu^I(DMEGqu)_2](PF_6)$ and $[Cu^{II}(DMEGqu)_2](OTf)_2 \cdot MeCN$.[56] These complexes are characterized by the fact that the structures of their cationic units are structurally very similar.

EXPERIMENTAL SECTION

HERFD-XANES Measurements. HERFD-XANES experiments were performed at beamline ID26 at the European Synchrotron Radiation Facility (ESRF) in Grenoble, France. For measurements at the copper K-edge (8979 eV), a Si(311) double-crystal monochromator was used. The maximum beam current was 200 mA with a ring energy of 6 GeV. For K-edge measurements, the solid samples were prepared as wafers using degassed cellulose as a binder to avoid self-absorption effects. Spectra were recorded at 30 K in a closed-cycle helium cryostat. The copper(I) samples were additionally prepared under an inert atmosphere in a glovebox. The spectrometer was kept under a helium atmosphere to reduce the absorption of fluorescence radiation. No signs of radiation damage could be detected in any sample within the acquisition time, and measurements were carried out on multiple spots.

DFT Calculations. *ORCA.* Copper K-edge transitions were calculated using the TD-DFT approach implemented in *ORCA3.0.2.*[33,57−59] In these calculations, the core properties were described by triple-ζ basis sets CP(PPP)[60] for the copper atom and Ahlrich's all-electron TZVP for all other atoms.[61−63] Geometry optimizations of ionized single molecules were carried out using *ORCA3.0.3* employing Ahlrich's TZVP on all atoms with TPSSh.[64] This is frequently considered the functional of choice for copper-related systems and has in particular been proven useful for the description of the structural and vibrational properties of quinoline−guanidine copper complexes.[65−68] Furthermore, the Grimme dispersion correction with Becke−Johnson damping (D3BJ) has been utilized.[69,70] XANES spectra have been calculated for different molecular structures, i.e., for the self-consistently optimized gas-phase (*ORCA*) geometries, for single molecules, the geometry of which is obtained from the experimentally determined crystal structures (X-ray diffraction) and for molecular structures based on the calculated solid-state geometries (QUANTUM ESPRESSO). Thereby, several XC functionals were tested, i.e., the meta-generalized gradient approximation (GGA) functional TPSS and its hybrid version TPSSh,[64] the hybrid GGA functional B3LYP,[71−74] and the semilocal GGA functionals BP86[75,76] and PBE.[77] To speed up the hybrid calculations, the RIJCOSX[78,79] approximation implemented in *ORCA* was used. A special DFT grid of seven was set for copper. The tight convergence criterion was imposed on all calculations. For further analysis of the results, we used the program *MOAnalyzer.*[80] The calculated spectra have all been shifted to match the copper K-edge: a shift of 33−44 eV was required for hybrid functionals and 216−233 eV for semilocal functionals. In addition to the shift, all spectra have been normalized to the intensity of a characteristic peak [in case of copper(II), the prepeak]. The discrete single-energy transitions have been subjected to Gaussian broadening, with a full width at half-maximum linearly rising with increasing excitation energy.

QUANTUM ESPRESSO. Periodic boundary conditions and a plane-wave basis were employed for the realistic modeling of molecular crystals using the *QUANTUM ESPRESSO* (QE) package[46] implementation of DFT. The QE package has also been used for XAS simulations based on the continued-fraction approach.[47,48] Specifically, the *Xspectra* code[46] is used in conjunction with gauge-including projector-augmented-wave (GIPAW) pseudopotentials. Within this PAW-XAS approach, the incorporation of the 1s core−hole into the copper pseudopotentials allows for a reliable, but computationally very efficient description of excitonic effects[49] using Lanczos recursion scheme to expand Green's function.[43−45] For structure optimization as well as for the simulation of XAS spectra, the complete crystal structures, including the counterions [two PF_6^- in the case of copper(I) species and eight OTf^- as well as one acetonitrile molecule for the copper(II) species], have been used. Notably, the calculated XAS spectra do not change considerably if we truncate the structures and consider only one molecule and its counterion(s) within periodic boundary conditions. This corresponds to bisecting and quartering of the actual crystal unit cell for the copper(I) and copper(II) systems. The insensitivity of the XAS simulations with respect to this structural simplification indicates that the weak intermolecular coupling between the molecules has only a minor influence on the XAS spectra. The XAS spectra are calculated using the same *k*-point sampling as that for the self-consistent total-energy calculations. A 2 × 2 × 2 *k*-point sampling and a cutoff energy of 90 Ry lead to numerically converged results for solid-phase calculations. The gas-phase calculations were done with the same cutoff, but with a single *k* point (Γ point) and using a large $(20\ \text{Å})^3$ supercell that mimics a single molecule in vacuum. Throughout the QE calculations, we use the PBE functional.[77] All calculations were done including van der Waals interaction (D3BJ dispersion), which is expected to be of particular relevance for the gas-phase structures.[68] The calculated spectra have been aligned with respect to the copper K-edge of the experimental spectra. The line width is chosen to be energy-dependent, rising arctan-like from 0.2 at 8975 eV to 2.0 at 8940 eV.[81] The broadening used in the calculations thus follows qualitatively the trend in the experimental spectra but is chosen to be somewhat smaller, in order to prevent it from masking the fine structure of the simulations.

Materials. The complexes $[Cu^{I}(DMEGqu)_2](PF_6)$ and $[Cu^{II}(DMEGqu)_2](OTf)_2{\cdot}MeCN$ were prepared according to a literature procedure.[56]

RESULTS AND DISCUSSION

HERFD-XANES Measurements. Two different counterions, PF_6^- and OTf^-, were used during crystallization of the copper(I) and copper(II) species, respectively.[56] The resulting key geometric parameters are given in Table 1; the unit cells and molecular structures of $[Cu^{I}(DMEGqu)_2]^+$ and $[Cu^{II}(DMEGqu)_2]^{2+}$ in the solid state are compared in Figure 1. The unit cell of the copper(I) species consists of two molecules plus *two* counterions (PF_6^-), whereby the arrangement of the two molecules shows inversion symmetry (cf. Figure 1, left). For copper(II), the molecular crystal structure is more complex and consists of *four* molecules plus *eight* OTf^- counterions plus four acetonitrile molecules (cf. Figure 1, right).

Table 1. Geometric Parameters of the Two Complexes (Obtained from X-ray Diffraction)

	$[Cu^{I}(DMEGqu)_2]$ PF_6	$[Cu^{II}(DMEGqu)_2](OTf)_2{\cdot}$ MeCN[a]
Bond Length [Å]		
$Cu{-}N_{imine,gua}$	2.113(2), 2.134(2)	1.978(3), 1.998(3)
$Cu{-}N_{qu}$	1.981(2), 1.959(2)	1.986(3), 1.981(3)
$C_{gua}{-}N_{imine,gua}$	1.302(3), 1.309(3)	1.347(4), 1.342(4)
$C_{gua}{-}N_{amine,gua}$	1.361(3), 1.366(3)	1.325(4), 1.341(4)
	1.352(3), 1.357(3)	1.324(4), 1.346(4)
Chelate Angle [deg]		
N−Cu−N	81.9(1), 81.8(1)	81.8(1), 82.7(1)
Structure Factor		
$\tau_4 = \frac{360° - (\alpha + \beta)}{141}$	0.57	0.36
Torsion Angle (deg)		
$\angle(C_{gua}N_3, CuN_2)$	44.2, 52.6	56.6, 60.4
$\angle(CuN_2, CuN'_2)$	63.1	42.2

[a] Here, two different molecules are present in the asymmetric unit.

As previously shown for $[Cu(tmeda)_2]^+$ (tmeda = tetramethylethylenediamine), one would expect a tetrahedral geometry for copper(I) complexes,[82] whereas the corresponding copper(II) system[83] is expected in a square-planar fashion. The DMEGqu complexes in this study exhibit geometries between these two extremes. The τ_4 parameter can be used to describe the geometry of a 4-fold coordination. By definition, ideal tetrahedral sites show a value of $\tau_4 = 1$ and square-planar sites $\tau_4 = 0$.[84] This was shown previously for related compounds,[7] and similar values are obtained.

The copper(I) complex $[Cu^{I}(DMEGqu)_2](PF_6)$ is characterized by a value of 0.57, indicative of a strongly distorted tetrahedron. The copper(II) complex $[Cu^{II}(DMEGqu)_2](OTf)_2{\cdot}MeCN$ shows a smaller value of 0.36. An alternative measure is given by the angle between the two chelate planes (90° = tetrahedron and 0° = square planar), which adopts values of 63° in the $[Cu^{I}(DMEGqu)_2]^+$ cation and 42° for $[Cu^{II}(DMEGqu)_2]^{2+}$, indicating a twist of about 20° upon oxidation.[56]

Figure 2 compares the conventional XANES spectra recorded in transmission with the HERFD-XANES spectra. The latter ones are obtained using a focusing Johann-type spectrometer with spherically bent analyzer crystals.[23,85] The energy of the

DOI: 10.1021/acs.inorgchem.6b01704
Inorg. Chem. 2016, 55, 11694−11706

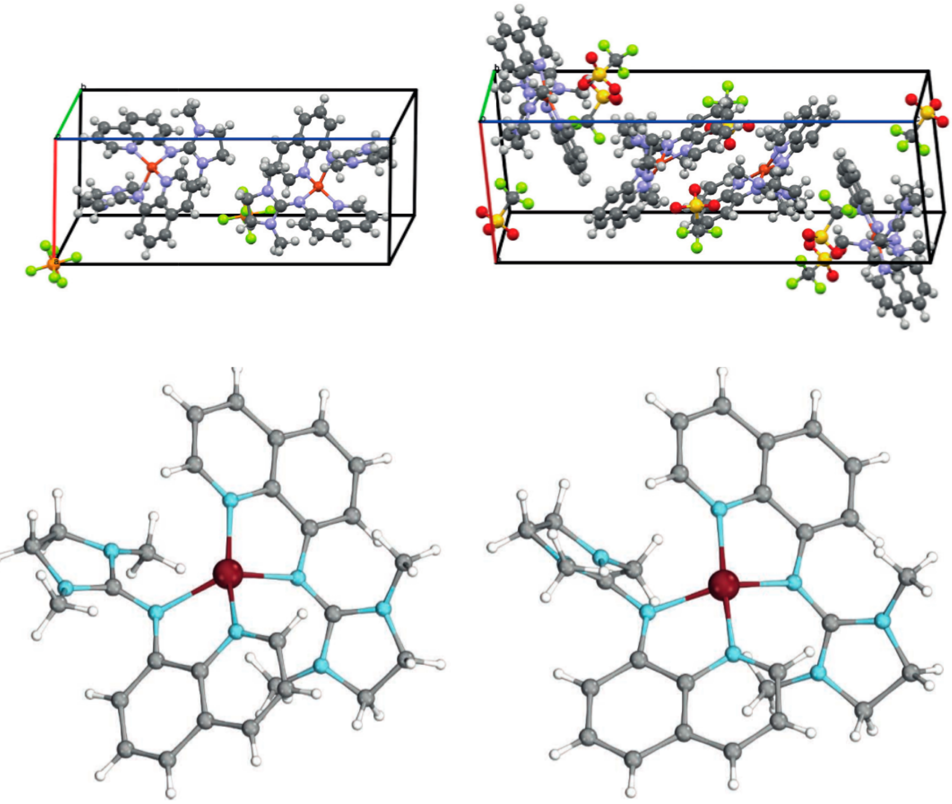

Figure 1. (Experimental) Unit cells of the complete molecular crystals (top) of $[Cu^{I}(DMEGqu)_2](PF_6)$ (triclinic, left) and $[Cu^{II}(DMEGqu)_2](OTf)_2\cdot$MeCN (triclinic, right) including the counterions. For the sake of clarity, enlarged structures of the cationic sites are shown below.[56]

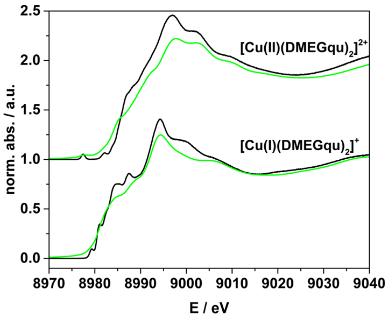

Figure 2. Comparison of the conventional (green) and high-resolution (black) XANES spectra taken for the same samples of $[Cu^{I}(DMEGqu)_2](PF_6)$ and $[Cu^{II}(DMEGqu)_2](OTf)_2\cdot$MeCN molecular crystals.

analyzer crystals is fixed at a certain value, and its intensity is recorded while the incident beam energy is swept over the absorption edge. These measurements follow the approach originally introduced by Hämäläinen et al.[86] as high-resolution fluorescence excitation in order to obtain lifetime-broadening-removed XANES spectra. Carra et al.[87] and Loeffen et al.[88] pointed out that this method is not strictly yielding lifetime-broadening-removed spectra. However, Tanaka et al.[89] showed that, under certain circumstances, the high-resolution excitation spectra are essentially identical with conventionally obtained XANES spectra but with much higher resolution and are thus called HERFD-XANES. Most important, the emitted photon energy has to correspond to a peak position in the fluorescent spectrum. Another core criterion is that off-diagonal elements representing nonlocal states are not present in the RIXS planes (cf. the Supporting Information) because they would lead to artifacts in the HERFD-XANES spectra. When this technique is applied, a tremendous increase in the resolution is observed,[25] as proven in Figure 2, whereby the degree of resolved fine structure is particularly obvious for the copper(I) complex. The benefit of high-energy-resolution-fluorescence detection is 3-fold: (i) the experimental background is nearly eliminated; (ii) the prepeak, if present, of the copper(II) complex is significantly better resolved, and (iii) the XANES fine structure is impressively sharpened but obviously to different extents.

While the first point is more or less only relevant for a better analysis of the prepeak intensities, the latter two points offer further valuable information on the investigated species: The 4-fold coordination can be identified by comparing the preedge intensity and general spectral shape to those in earlier studies.[90] Also, the influence of the oxidation state on the edge position is easily recognized: The edge of copper(II) is shifted by 3 eV with respect to copper(I). Most remarkably, the spectra, especially for the copper(I) case, reveal a detailed fine structure in the edge. In other words, the HERFD-XANES measurements yield richer spectral information compared to conventional measurements,

DOI: 10.1021/acs.inorgchem.6b01704
Inorg. Chem. 2016, 55, 11694−11706

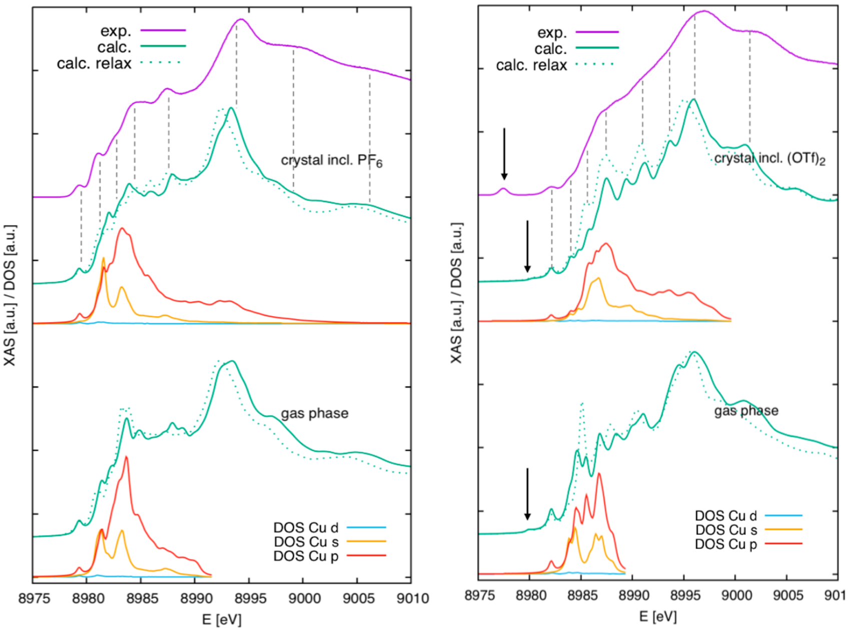

Figure 3. Comparison of the experimental copper(I) (left) and copper(II) (right) XAS spectra with theoretical PAW-XAS spectra calculated for the experimental crystal structures (solid green lines): (i) for a periodic molecular crystal including the counterions PF_6^- and OTf^-, respectively (top); (ii) for charged isolated molecules, i.e., for the gas phase (bottom). For further comparison, calculated spectra for the self-consistently relaxed structures are also indicated by dotted lines. Vertical dashed lines serve as guides for the eyes. For copper(II), the prepeak is indicated by arrows. The further curves describe the projected DOS.

which allows for a more detailed comparison to theoretical calculations, e.g., a more accurate assignment of the underlying transitions. As already mentioned in the Introduction, the prepeak region is best described by TD-DFT, while above the Fermi level, the continued-fraction approach describes the measured data very well. This will be demonstrated in the following sections.

DFT Simulations of XANES Spectra. *I. PAW-XAS Results.* In order to get an overview and an understanding of the general shape of the XAS spectra, we start our DFT simulation with the continued-fraction PAW-XAS method. The multiprojector GIPAW approach is able to describe the XAS spectrum in a broad energy range up to 30 eV and more above the copper K-edge, as demonstrated in Figure 3. Especially in the case of the copper(I) complex, the agreement is quite impressive if a periodic molecular crystal including the PF_6^- counterions is modeled (green curves in Figure 3, top): All peaks and shoulders are present and predicted at reasonably correct energies. For the copper(II) complex, in particular in the region 5−15 eV above the edge, the agreement is less obvious because the resolved experimental features are not as pronounced as those in the copper(I) case. Here, an improved agreement between the experiment and theory can be enforced by increasing the line width of the calculated spectra by a factor of 2. On the basis of the presently available data, we speculate that the larger unit cell for the copper(II) provides more spatial degrees of freedom and is potentially more easily affected by thermal vibrations and, consequently, by an enhanced thermal broadening of the spectra.

It is noteworthy that all of the PAW-XAS spectra are obtained while explicitly taking into account occupied states exclusively. Thanks to the projectors and the Lanzcos recursion scheme,[44−46] we can profit from the completeness relationship of an infinite quantum mechanical basis set by substituting (infinite) sums over empty states with (finite) sums over occupied states. In fact, additional calculations for the projected density of states (DOS) reveal that 420 empty states are distributed over a limited energy range of about 10 eV; see also the base lines in Figure 3. To cover the full energy range, several tens of thousands empty states would be required.

We further note that as good as possible agreement with the global shape of the experimental spectra is generally obtained by simulations that are based on the complete unit cell of the molecular crystal, taking also into account the counterions explicitly, either by using the experimental crystal structure from single-crystal X-ray diffraction (cf. Figure 1 and Table 1) or by using structures relaxed within DFT, i.e., as obtained from minimizing the Hellmann−Feynman forces within the molecular crystals. By the latter approach, the features of the far-edge part of the spectrum are slightly red-shifted toward the edge step, but in parallel some near-edge features are better described (see the dotted lines in Figure 3). This is, in particular, true for the copper(I) species and the shape and height of the characteristic shoulder at 8981 eV (2 eV above the edge), which originates from strong metal-to-ligand charge-transfer (MLCT) Cu 1s → C 2p, N 2p transitions.

When modeling the corresponding gas-phase species, i.e., the ionized isolated molecules without counterions, most features of the spectra are reproduced, but the relative intensity of some peaks is inverted in comparison to the experiment, in particular in the region 2−6 eV above the copper K-edge, where the Cu 1s → 4p transitions are strongly overestimated in the gas-phase modeling, in particular for the copper(II) case. Finally, the

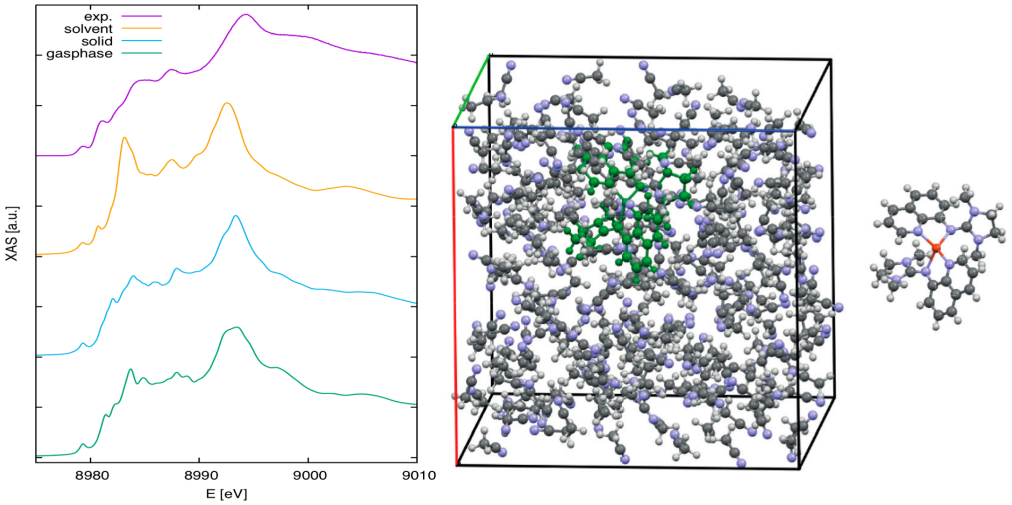

Figure 4. DFT-calculated XAS spectra for the $[Cu^{I}(DMEGqu)_2]^+$ species in acetonitrile (left, yellow line), modeled within a large, $25.7 \times 25.7 \times 25.7$ A^3 supercell (right) containing the copper(I) complex itself (green, colored besides) and 231 solvent molecules (in total 1452 atoms).

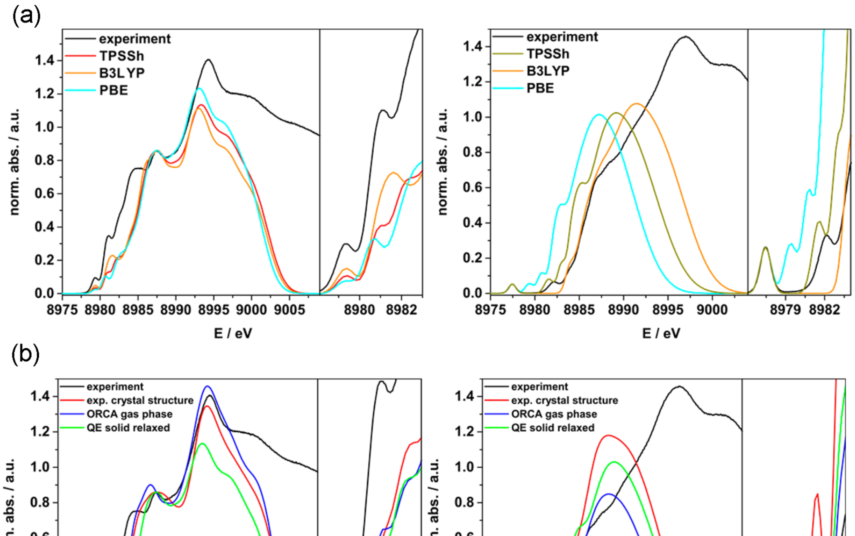

Figure 5. (a) Comparison of the TD-DFT-calculated copper(I) (left) and copper(II) (right) spectra using different XC functionals for the QE-relaxed solid structure. For copper(I), the intensity of the spectra is normalized to the intensity of the 8987 eV peak; for copper(II), it is normalized to that of the prepeak at 8977.5 eV. (b) Calculated XANES spectra (TD-DFT with the TPSSh functional) for DFT-relaxed structures (gas phase and molecular crystal) and for the experimental crystal structure in comparison to the experimental spectrum. For copper(I) (left), the intensity of the spectra is normalized to the intensity of the 8987 eV peak; for copper(II) (right), it is normalized to that of the prepeak at 8977.5 eV. Transitions into 120 and 250 empty states have been used for copper(I) and copper(II), respectively.

prepeak features caused by 1s → LUMO transitions are not properly described in the continued-fraction approach. The intensity of the prepeak at 8977.45 eV and its distance to the edge is considerably underestimated. The latter is mainly related to the common underestimation of the highest occupied molecular orbital (HOMO)−LUMO gaps if using semilocal XC functionals. Note that, for the near- and far-edge regions, related to transitions into more delocalized empty states, this problem plays a minor role. For a more detailed quantitative discussion of the prepeak, however, we refer to the TD-DFT calculations described below, where, in particular, the influence of the used XC functional is thoroughly investigated.

It has to be noted that, strictly speaking, the modeling of isolated molecules does not correspond to the experimental situation, where XAS is performed either on molecular crystals (solid state) or on molecular species in solution. Similar to the solid state, also in solution the interaction with the neighboring solvent molecules is able to influence the XAS spectra significantly. To illustrate this, we have performed additional calculations for the $[\mathrm{Cu^I(DMEGqu)_2}]^+$ species in an acetonitrile (C_2H_3N) solution. For this purpose, a copper(I) complex has been modeled in a large supercell containing 231 solvent molecules equivalent to a 78 mM concentration of solution (see Figure 4). In a first step, the atomic positions of the copper(I) complex are kept fixed, while the distribution of the solvent molecules is optimized using molecular dynamics. Afterward, within such an optimized solvent environment, the copper(I) complex is allowed to relax freely. For the resulting structure, we calculate the copper K-edge XAS spectrum. Again a quite good agreement with the results of the solid-state simulation is obtained for large parts of the spectrum (cf. Figure 4, left). The peak at 8983 eV, however, appears to be considerably overestimated, similar to the relaxed gas-phase geometry, but even more pronounced (cf. Figure 3, bottom, left). The intensity of this peak, which is mainly characterized by transitions into the ligand π^* system with a predominant amount of C 2p orbitals (for further details, see the next section), depends very sensitively on the microscopic details of the solvent environment. This will result (i) in effectively reduced intensities in statistical ensembles as in the experiment and (ii) a considerably larger temperature dependence of the XAS spectra as in the case of the solid state (molecular crystals).

Obviously, precise modeling of the molecules in solution and simulation of their XAS spectra are rather cumbersome because they require statistical averaging over a large ensemble of structures. Here, the so-called gas-phase modeling of isolated molecules (within reasonable geometries) actually provides an efficient alternative, which will also be used in the TD-DFT calculations described below.

II. TD-DFT Results. Usually the intensity of a prepeak is used to adjust the TD-DFT-derived XAS spectra to the experimental spectra. For copper(II), this leads to an adequate relationship between the various spectra (see, e.g., Figure 5a, right). In the copper(I) case with a completely filled $3d^{10}$ shell, however, there is no such classical prepeak. Using the first peak at the copper K-edge instead is not reliable because its intensity depends strongly on the technical details of the theoretical description (e.g., the choice of the XC functional; cf. Figure 5a, left). Thus, it does not provide a reliable global reference. Here, we use the peak around 8987 eV as an alternative. Its intensity as well as its energetic position does not depend on the DFT functional, and the latter agrees nicely with the experimental one.

a. Influence of the Geometry. The relationship between the molecular structure and simulated spectra inferred from the continued-fraction approach is largely confirmed by TD-DFT calculations: The near-edge regions seem to be described slightly better when the DFT-relaxed structures are used instead of the experimental ones. This can be clearly seen in the case of the copper(II) species by analyzing the characteristic shoulder above 8985 eV. Figure 5b (right) shows (using the all-in-all best-performing TPSSh functional; cf. Figure 5a) that its shape is best reproduced for the fully relaxed crystal structure. At this point, it is not clear if this is really due to changes in the crystal structure, e.g., increased C−H bond lengths, or due to some kind of error cancellation within gas-phase modeling. Notably, for copper(II), the torsion angle between the two CuN_2 planes in the first coordination shell, a quantity that characterizes the entatic state of the complexes used for this study, is basically the same for the crystal structure relaxed within DFT-PBE and the relaxed gas-phase geometry obtained using the TPSSh functional. It becomes, however, obvious that the self-consistently relaxed gas-phase geometries provide no valid starting point for simulation of the X-ray spectra: The symmetry of the resulting structures is considerably overestimated; e.g., the Cu−N distances become pairwise identical (see Tables 2 and 3). In other words, the structures lose their characteristic asymmetry. With HERFD-XANES being a local method, the Cu−N distances are important as well, besides the torsion angle between the two CuNN planes. Unique shifts of all Cu−N distances (as expected for the bond length overestimating the PBE functional[65,67]) lead only to an energy shift of the whole spectra. The asymmetry within the two chemically equivalent $\mathrm{Cu{-}N_{qu}}$ and $\mathrm{Cu{-}N_{imine,gua}}$ distances, in contrast, leads to the characteristic splittings of the main peaks in the near-edge region, contributing substantially to the shape of the spectra.

Table 2. Geometric Parameters of the Copper(I) Structures Derived from Gas-Phase Optimization for Two Different DFT Functionals (TPSSh and PBE), from a Relaxation of the Molecular Crystal (Solid) and the Experimental Crystal Structure (from X-ray Diffraction) Itself

copper(I)	exptl crystal structure	gas-phase TPSSh	gas-phase PBE	solid relaxed PBE
τ_4	0.57	0.67	0.65	0.62
$\mathrm{Cu{-}N_{qu}}$	1.981(2), 1.959(2)	1.973, 1.973	2.017, 2.017	2.025, 1.994
$\mathrm{Cu{-}N_{imine,gua}}$	2.113(2), 2.134(2)	2.110, 2.109	2.181, 2.182	2.098, 2.098
$\angle \mathrm{CuN_2/CuN'_2}$	63.1	76.6	76.6	69.6

Table 3. Geometric Parameters of the Copper(II) Structures Derived from Gas-Phase Optimization for Two Different DFT Functionals (TPSSh and PBE), from a Relaxation of the Molecular Crystal (solid) and the Experimental Crystal Structure (from X-ray Diffraction) Itself

copper(II)	exptl crystal structure	gas-phase TPSSh	gas-phase PBE	solid relaxed PBE
τ_4	0.36	0.43	0.47	0.46
$\mathrm{Cu{-}N_{qu}}$	1.986(3), 1.981(3)	1.973, 1.972	2.027, 2.026	2.021, 2.008
$\mathrm{Cu{-}N_{imine,gua}}$	1.978(3), 1.998(3)	1.967, 1.967	2.065, 2.066	2.033, 1.999
$\angle \mathrm{CuN_2/CuN'_2}$	42.2	45.6	51.6	45.8

b. Influence of XC Functionals. Out of the functionals probed here, TPSSh performs all-in-all best concerning the modeling of the XANES spectra. Taking also the kinetic energy of the orbitals into account, this meta-hybrid functional with a moderate amount of Hartree−Fock (HF) exchange (10% in comparison to 25% in B3LYP) has been frequently reported to describe the structural and electronic properties of similar 3d transition-metal-including complexes.[7,66,67] We found that the absolute energies, i.e., the position of the copper K-edges, are generally closer to the experiment for all hybrid calculations. This can be explained with the addition of HF exchange reducing the self-interaction error and therefore giving higher accuracy for strongly localized core states as well as for the Cu 3d levels and, thus, for the corresponding core−excited state transitions.[32] Even more important, the energy splitting between the prepeak and the following features for the copper(II) species is too small for the nonhybrid functionals throughout all calculated spectra. It is noteworthy that this splitting is too small even for the TPSSh functional that contains rather moderate 10% exact exchange. The position of the prepeak becomes even worse (now too far away from the copper K-edge) for standard hybrid functionals like B3LYP. This kind of overcorrection, however, can be fixed by adjusting the fraction of HF exchange. In the case of copper(II), 12.5% HF exchange was needed to achieve the correct splitting in the preedge region (additional spectra provided in the Supporting Information), whereas for copper(I), the HF exchange did not show a significant influence, as can be seen in Figure 5b for the two spectra calculated with B3LYP (25% HF) and TPSSh (10% HF). We attribute this substantial difference to the electron configuration being paramagnetic $3d^9$ in the copper(II) case and diamagnetic closed-shell d^{10} for copper(I), which renders the concomitant influence of the exchange interaction less significant. In the following sections, only the TPSSh functional results will be discussed for the TD-DFT calculations.

c. Comparison with the Experiment. We start a more detailed discussion of the two different complexes with the copper(II) compound $[\mathrm{Cu^{II}(DMEGqu)_2}](\mathrm{OTf})_2\cdot\mathrm{MeCN}$, which, thanks to the open-shell $3d^9$ configuration, gives rise to the aforementioned distinct prepeak. The measured HERFD-XANES spectra (cf. Figures 2 and 5a,b) locate this prepeak at 8977.45 eV. Our TD-DFT calculations reveal a 1s orbital to LUMO transition underneath this peak. The spatial distribution of the β-LUMO is shown in Figure 6 and consists mostly (>55%) of Cu 3d orbitals (detailed contributions are provided in the Supporting Information). A symmetry-dependent admixture of Cu p as well as p orbitals of the nitrogen and carbon ligands allows for a dipole transition that leads to a significantly enlarged intensity compared to a pure 1s → 3d transition. Nevertheless, the quadrupole (1s → 3d) transition still accounts for as much as 25% intensity. The following feature at 8982 eV is mainly characterized by transitions in the ligand π^* system with a predominant amount of C 2p orbitals. The next intense feature in the edge above 8985 eV can be assigned to a 1s → 4p + LMCT shakedown (multielectron) transition, similar to that reported previously for square-planar copper(II) complexes.[91] At higher energies, the localized and finite character of the basis set used for the TD-DFT calculations prevents the reproduction of spectral features. Additional multiscattering effects, thus, cannot be considered within TD-DFT.[92]

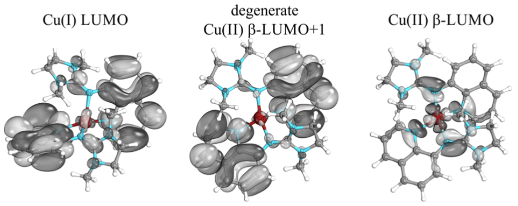

Figure 6. Comparison of the acceptor orbital (LUMO) related to the first transition peak in the calculated copper(I) spectra (left) and the degenerate β-LUMO+1/β-LUMO+2 of the copper(II) calculation (middle); acceptor orbital (β-LUMO) of the prepeak transition calculated for the copper(II) species (right).

As already mentioned above, the copper(I) spectrum of $[\mathrm{Cu^{I}(DMEGqu)_2}](\mathrm{PF_6})$ (Figure 5a,b, left) shows no prepeak because the $3d^{10}$ configuration does not allow for 1s → 3d transitions. The LUMO for the copper(I) species is shown in Figure 6 (left) and consists mostly of ligand π^* orbitals. These features around 8980 eV can accordingly be assigned to MLCT transitions. A closer look reveals that this calculated feature is of the same character as that in the copper(II) case but shifted to lower energies because of the smaller ionization threshold in copper(I), i.e., the influence of the nuclear charge on the orbital energies. The LUMO of the copper(I) case (Figure 6, left) is indeed very similar to the degenerate β-LUMO+1/β-LUMO+2 (Figure 6, middle) in the copper(II) case. These assignments strengthen the MLCT assignment.[33,93] The copper(I) spectra show a characteristic, very intense 1s → 4p transition visible as a shoulder. This feature is shifted to higher energies for copper(II); it is, therefore, often hidden under the edge.

d. Sensitivity to Structural Changes. To further elucidate the effect of geometrical distortions on the XANES spectra (as, e.g., relevant in entatic states), we also calculated spectra for *constrained* tetrahedral ($\angle\mathrm{CuN_2/CuN_2'} = 90°$) and square-planar ($\angle\mathrm{CuN_2/CuN_2'} = 0°$) geometries. For this purpose, the values of the N−Cu−N angles (except the two ligand chelate angles) were fixed, while otherwise relaxing the positions of all of the atoms of the cationic gas-phase molecules. Thereby, the $\angle\mathrm{CuN_2/CuN_2'}$ angles were fixed to the mentioned 0°/90° values as well. This also results in a change of the bond lengths (see the Supporting Information), which has been described earlier,[65] but does not affect the value for the following discussion. The XANES spectra (Figure 7, left) calculated for the two resulting structures show clearly distinguishable prepeak intensities as well as significantly different intensities for the following preedge transitions. This can be explained by the changing amount of the p contribution to the acceptor orbital of the excitation in the XAS process. The square-planar case mimics an ideal quadrupole. Consequently, the prepeak is predominantly determined by the quadrupole term. No significant dipole contribution is found because in the LUMO there is no admixture of Cu p orbitals and only a little of the C and N p orbitals. Note that the contribution of the N p orbitals remains nearly constant and is, thus, not discussed further in this context. The tetrahedral coordination, in contrast, shows a maximum electric-dipole contribution (being responsible for more than 90% of the intensity). The LUMO in this case consists of 2% Cu 4p and 15% C 2p orbitals in conjunction with an amount of 45% Cu d. Figure 8 shows the orbital shape of the LUMOs; the orbital contributions for the different cases are listed in Table 4. A comparison of the shape and features of the calculated spectra confirms the importance of the $\angle\mathrm{CuN_2/CuN_2'}$ angle. As expected, none of the extreme cases is able to reproduce the spectrum of the $[\mathrm{Cu^{II}(DMEGqu)_2}](\mathrm{OTf})_2\cdot\mathrm{MeCN}$ structure. Mixing, however, the spectra obtained for the two extreme angles of 0 and 90° with their respective ratios (51% tetrahedral and 49% square-planar, giving an angle of 45.84°; cf. Table 3) results in a spectrum that shows a good agreement with the actual spectrum of $[\mathrm{Cu^{II}(DMEGqu)_2}](\mathrm{OTf})_2\cdot\mathrm{MeCN}$, despite the tetrahedral and square-planar geometries being strongly constrained, i.e., providing hypothetical constructs. In Figure 7 (TD-DFT results), this is shown for the near-edge regime, and in Figure 9, right (PAW-XAS results), also for the far-edge region using the same mixing ratio

DOI: 10.1021/acs.inorgchem.6b01704
Inorg. Chem. 2016, 55, 11694−11706

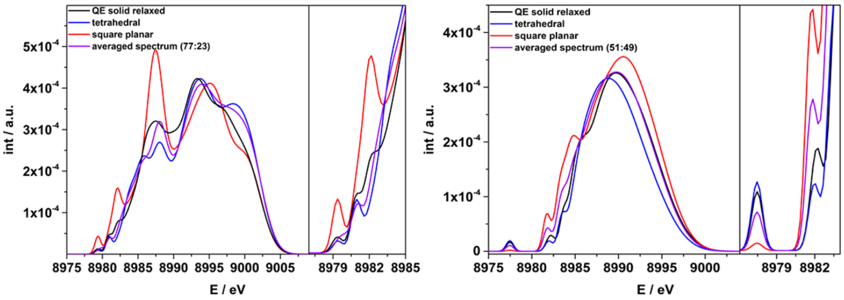

Figure 7. Comparison of the TD-DFT calculated spectra for the constrained square-planar and tetrahedral geometries for the copper(I) (left) and copper(II) (right) cases. Weighted-averaged spectra (77:23 and 51:49, respectively) and the spectra from a fully relaxed crystal geometry (QE solid relaxed) are also given. Right insets: zoom of the preedge regions.

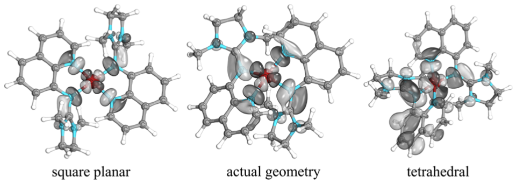
square planar actual geometry tetrahedral

Figure 8. Spatial distribution of the β-LUMO orbitals for the three different copper(II) configurations, illustrating the increasing localization on the ligands with increasing tetrahedral distortion.

Table 4. s, p, and d Orbital Contributions (%) for Each LUMO of the Copper(II) Calculations Split into Fractions for Copper, Nitrogen, and Carbon

	Cu		N		C	
LUMO contributions	p	d	s	p	s	p
solid relaxed	2.3	55.0	2.9	20.7	0.0	6.9
square-planar	0.0	57.3	4.1	22.0	0.0	4.5
tetrahedral	2.0	45.1	1.1	21.9	0.0	15.5

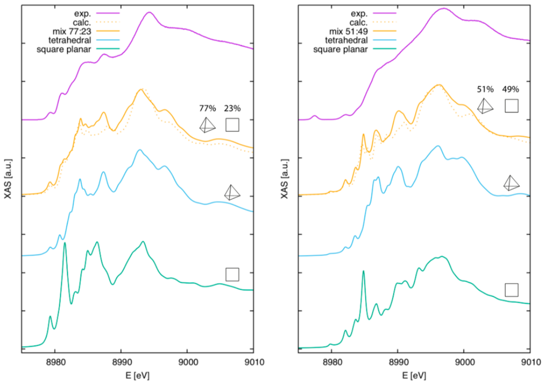

Figure 9. Theoretical XANES spectra for the copper(I) (left) and copper(II) (right) gas-phase molecules (PAW-XAS results) calculated for different geometries: for the constrained square-planar (green) and tetrahedral (blue) geometries and for the weighted mixtures of 77:23 for copper(I) and 51:49 for copper(II). For comparison, the spectra for the minimum total energy geometries are also indicated (dotted lines), and the experimental spectra (top) are also given again.

of 51:49. Here, the curve from mixing, i.e., more or less from averaging the constrained limits (solid line), follows nicely the curve calculated for the actual experimental geometry (dashed line); by this, it also agrees with the experimental HERFD-XANES spectrum. In addition, this procedure leads to a magnification of the prepeak, most clearly visible in the square-planar geometry.

For copper(I), the benefit of the mixing procedure is also significant (Figure 9, left). However, the tetrahedral contribution dominates the now clearly weighted superposition given by 77% (tetrahedral) and 23% (square-planar) relating to an angle of 69.59° (cf. Table 2). As a consequence, already the purely tetrahedral geometry reproduces the actual experimental spectrum of $[\text{Cu}^{\text{I}}(\text{DMEGqu})_2](\text{PF}_6)$ for the high-energy transitions above 8982 eV. In this sense, for copper(I), the benefit of a square-planar admixture is restricted to the region close to the edge: In TD-DFT (Figure 7, left), the square-planar spectrum yields a too large energetic split-up between the first transitions. The tetrahedral limit, on the other hand, fits the preedge region quite well. The combination of both extremes again fits the features as well as in the copper(II) case.

■ SUMMARY AND CONCLUSION

Here HERFD-XANES spectroscopy is combined for the first time with the theoretical spectroscopy based on TD-DFT and the PAW-XAS approach in order to achieve a comprehensive description and understanding of the HERFD-XANES data. This combined approach was applied to provide a proof-of-principle for the investigation of small structural changes (e.g., entatic-state effects) in biomimetic geometrically constrained copper complexes. A $\text{Cu}^{\text{I}}/\text{Cu}^{\text{II}}$ redox couple stabilized by a DMEGqu ligand served as an ideal case study: the 4-fold Cu−N coordination in both oxidation states deviates from the prototypical textbook cases, tetrahedral for copper(I) and square-planar for copper(II).

With the combination of TD-DFT and PAW-XAS, the rich information content in the HERFD-XANES spectra, ranging from the preedge signals, over the edge fine structure up to the first oscillations in the XAS coefficient after the edge step, can be fully utilized to characterize the structural and electronic changes when the copper oxidation state is changed from Cu^{I} to Cu^{II}. It thus will enable future high-resolution X-ray studies on the ET processes facilitated by ligand-induced geometry distortions. While the preedge peak is best described by TD-DFT because of its localized 1s → LUMO transitions, the local basis used in the TD-DFT calculations prevents a proper description of transitions at higher energies in the near-edge and, in particular, the far-edge region. Nevertheless, the range over which TD-DFT predicts spectral features with reasonable quality even in the rising edge region with its quasi-continuum states is astonishing and, to our knowledge, unprecedented: So far, TD-DFT has only been applied to predict preedge peaks, and no attempts were made to apply it to transitions beyond these energies.[92,94]

But still, starting with the rising edge, the PAW-XAS approach in the continued fraction is superior because (i) plane waves are ideally suited to describe the delocalized high-energy states and periodic systems such as the experimentally investigated molecular crystals, (ii) thanks to a multiprojector description, the Lanzcos recursion scheme, and (iii) by making use of completeness relation, the XANES spectra can be reasonably described for a broad energy range covering at least 30 eV. Although muffin-tin full multiple scattering and finite-difference-method approaches are more powerful to simulate spectra up to higher energies including the EXAFS region, the results here are the first to simulate XANES data using a full-electron approach that proves to be accurate enough to reproduce even the features in the HERFD-XANES spectra in terms of energy and intensity.

With both methods, the effect of geometrical distortion on the electronic structure in an entatic-state model, as reflected in the HERFD-XANES spectra of the molecular crystals, can be explained. In order to investigate the feasibility of the applied theoretical methods, different kinds of modeling were used in the theoretical spectral calculations: (i) periodic molecular crystals from the experimental single-crystal parameters as well as fully relaxed geometries and (ii) charged isolated gas-phase molecules. The PAW-XAS calculations based on the periodic molecular crystal (including the counterions) give slightly better results than simulations based on gas-phase molecules. The latter, however, still predict all transitions but with reduced accuracy concerning the peak intensities. The same trend is obtained in the TD-DFT calculations. Here, the TPSSh hybrid functional is found to yield best results, confirming recent findings from similar copper complexes.[65−68]

It could finally be shown that, for cases in which expensive theoretical calculations are *not* feasible, a simple fingerprint approach based on the linear combination XANES principle[95,96] can be used to identify the degree of internal, ligand-induced distortion by comparing experimental data with a weighted mixture of spectra calculated for hypothetical tetrahedral and square-planar structures of the same compound. This requires, of course, high-resolution experimental spectra that are available thanks to HERFD-XANES spectroscopy.

With these results, the way is paved for investigations on biomimetic complexes in situ, i.e., under biocatalytic conditions. Such systems are characterized by low concentrations and interfering solvent molecules. By additional comparative calculations, we have shown that the spectra of *individual* molecules in solution depend strongly on the microscopic details of the solvent environment. The statistical ensembles investigated in the experiments, thus, seem to be explained in a more reliable way by modeling gas-phase molecules. However, further detailed studies are necessary to confirm this suggestion for biomimetic complexes in low-concentrated solution in general. By using hard X-rays in HERFD-XANES measurements, which are conducted in fluorescence geometry and with high incoming fluxes, the electronic states and connectively the geometric structure can be determined under such conditions. Moreover, making use of time-resolved experiments at synchrotrons or even free electron lasers,[97−100] the ET reactions of the entatic state and type-zero model complexes can be investigated by means of the changes in the orbital contributions to the HERFD-XANES spectra. We finally conclude that HERFD-XANES in combination with computational modeling opens up new opportunities for the investigation of ET processes in chemistry.

■ ASSOCIATED CONTENT

Supporting Information

The Supporting Information is available free of charge on the ACS Publications website at DOI: 10.1021/acs.inorgchem.6b01704.

RIXS planes, calculated spectra of additional geometries, and acceptor orbital contributions of selected transitions and geometric parameters of the geometries used in the calculations (PDF)

■ AUTHOR INFORMATION

Corresponding Authors

*E-mail: uwe.gerstmann@uni-paderborn.de (U.G.).
*E-mail: matthias.bauer@uni-paderborn.de (M.B.).

Author Contributions

§These authors contributed equally to this work and should therefore be acknowledged as joint first authors.

Notes

The authors declare no competing financial interest.

■ ACKNOWLEDGMENTS

The ESRF is acknowledged for a provision of beamtime. We thank Dr. Mauro Rovezzi for assistance during the measurements. The Deutsche Forschungsgemeinschaft is acknowledged for financial support (Grant FOR1405). Generous grants of computer time at the Paderborn Center for Parallel Computing PC^2 and the HLRS Stuttgart are gratefully acknowledged.

■ REFERENCES

(1) Solomon, E. I.; Hadt, R. G. Recent advances in understanding blue copper proteins. *Coord. Chem. Rev.* **2011**, *255*, 774−789.

(2) Hosseinzadeh, P.; Marshall, N. M.; Chacón, K. N.; Yu, Y.; Nilges, M. J.; New, S. Y.; Tashkov, S. A.; Blackburn, N. J.; Lu, Y. Design of a single protein that spans the entire 2-V range of physiological redox potentials. *Proc. Natl. Acad. Sci. U. S. A.* **2016**, *113*, 262−267.

(3) Lancaster, K. M.; DeBeer George, S.; Yokoyama, K.; Richards, J. H.; Gray, H. B. Type-zero copper proteins. *Nat. Chem.* **2009**, *1*, 711−715.

(4) Comba, P.; Kerscher, M. Computation of structures and properties of transition metal compounds. *Coord. Chem. Rev.* **2009**, *253*, 564−574.

(5) Rorabacher, D. B. Electron Transfer by Copper Centers. *Chem. Rev.* **2004**, *104*, 651−697.

(6) Gray, H. B.; Malmström, B. G.; Williams, R. J. P. Copper coordination in blue proteins. *JBIC, J. Biol. Inorg. Chem.* **2000**, *5*, 551−559.

(7) Hoffmann, A.; Binder, S.; Jesser, A.; Haase, R.; Flörke, U.; Gnida, M.; Salomone-Stagni, M.; Meyer-Klaucke, W.; Lebsanft, B.; Grünig, L. E.; Schneider, S.; Hashemi, M.; Goos, A.; Wetzel, A.; Rübhausen, M.; Herres-Pawlis, S. Catching an Entatic State-A Pair of Copper Complexes. *Angew. Chem., Int. Ed.* **2014**, *53*, 299−304.

(8) Comba, P. Coordination compounds in the entatic state. *Coord. Chem. Rev.* **2000**, *200−202*, 217−245.

(9) Hancock, R. D.; Martell, A. E. Ligand design for selective complexation of metal ions in aqueous solution. *Chem. Rev.* **1989**, *89*, 1875−1914.

(10) Knapp, S.; Keenan, T. R.; Zhang, X.; Fikar, R.; Potenza, J. A.; Schugar, H. J. Nearly tetrahedral 1:2 complexes of copper(I), copper(II), nickel(II), cobalt(II), and zinc(II) with 2,2′-bis(2-imidazolyl)biphenyl. *J. Am. Chem. Soc.* **1987**, *109*, 1882−1883.

(11) Comba, P.; Kerscher, M.; Roodt, A. Slow Electron Self-Exchange in Spite of a Small Inner-Sphere Reorganisation Energy ? The Electron-Transfer Properties of a Copper Complex with a Tetradentate Bispidine Ligand. *Eur. J. Inorg. Chem.* **2004**, *2004*, 4640−4645.

(12) Xie, B.; Elder, T.; Wilson, L. J.; Stanbury, D. M. Internal Reorganization Energies for Copper Redox Couples: The Slow Electron-Transfer Reactions of the [Cu II/I (bib) 2] 2+/+ Couple. *Inorg. Chem.* **1999**, *38*, 12−19.

(13) Chaka, G.; Sonnenberg, J. L.; Schlegel, B. H.; Heeg, M. J.; Jaeger, G.; Nelson, T. J.; Ochrymowycz, L. A.; Rorabacher, D. B. A Definitive Example of a Geometric "Entatic State" Effect: Electron-Transfer Kinetics for a Copper(II/I) Complex Involving A Quinquedentate Macrocyclic Trithiaether−Bipyridine Ligand. *J. Am. Chem. Soc.* **2007**, *129*, 5217−5227.

(14) Garcia, L.; Cisnetti, F.; Gillet, N.; Guillot, R.; Aumont-Nicaise, M.; Piquemal, J.-P.; Desmadril, M.; Lambert, F.; Policar, C. Entasis through Hook-and-Loop Fastening in a Glycoligand with Cumulative Weak Forces Stabilizing Cu I. *J. Am. Chem. Soc.* **2015**, *137*, 1141−1146.

(15) Dahl, E. W.; Szymczak, N. K. Hydrogen Bonds Dictate the Coordination Geometry of Copper: Characterization of a Square-Planar Copper(I) Complex. *Angew. Chem.* **2016**, *128*, 3153−3157.

(16) Comba, P. Strains and stresses in coordination compounds. *Coord. Chem. Rev.* **1999**, *182*, 343−371.

(17) Comba, P.; Schiek, W. Fit and misfit between ligands and metal ions. *Coord. Chem. Rev.* **2003**, *238*−*239*, 21−29.

(18) Comba, P.; Müller, V.; Remenyi, R. Interpretation of the temperature-dependent color of blue copper protein mutants. *J. Inorg. Biochem.* **2004**, *98*, 896−902.

(19) Bauer, M.; Bertagnolli, H. X-Ray Absorption Spectroscopy - the Method and Its Applications. *Methods in Physical Chemistry*; Wiley-VCH Verlag GmbH & Co. KGaA: Weinheim, Germany, 2012; pp 231−269.

(20) Haumann, M.; Liebisch, P.; Müller, C.; Barra, M.; Grabolle, M.; Dau, H. Photosynthetic O2 Formation Tracked by Time-Resolved X-ray Experiments. *Science* **2005**, *310*, 1019−1021.

(21) Dau, H.; Liebisch, P.; Haumann, M. X-ray absorption spectroscopy to analyze nuclear geometry and electronic structure of biological metal centers-potential and questions examined with special focus on the tetra-nuclear manganese complex of oxygenic photosynthesis. *Anal. Bioanal. Chem.* **2003**, *376*, 562−583.

(22) Bjornsson, R.; Delgado-Jaime, M. U.; Lima, F. A.; Sippel, D.; Schlesier, J.; Weyhermüller, T.; Einsle, O.; Neese, F.; DeBeer, S. Molybdenum L-edge XAS spectra of MoFe nitrogenase. *Z. Anorg. Allg. Chem.* **2015**, *641*, 65−71.

(23) Glatzel, P.; Bergmann, U. High resolution 1s core hole X-ray spectroscopy in 3d transition metal complexes - Electronic and structural information. *Coord. Chem. Rev.* **2005**, *249*, 65−95.

(24) Atkins, A. J.; Bauer, M.; Jacob, C. R. High-resolution X-ray absorption spectroscopy of iron carbonyl complexes. *Phys. Chem. Chem. Phys.* **2015**, *17*, 13937−13948.

(25) Bauer, M. HERFD-XAS and valence-to-core-XES: new tools to push the limits in research with hard X-rays? *Phys. Chem. Chem. Phys.* **2014**, *16*, 13827−13837.

(26) Bechstedt, F. *Many-Body Approach to Electronic Excitations*; Springer Series in Solid-State Sciences 181; Springer: Berlin, 2015.

(27) Shirley, E. L. Ab Initio Inclusion of Electron-Hole Attraction: Application to X-Ray Absorption and Resonant Inelastic X-Ray Scattering. *Phys. Rev. Lett.* **1998**, *80*, 794−797.

(28) Coriani, S.; Fransson, T.; Christiansen, O.; Norman, P. Asymmetric-lanczos-chain-driven implementation of electronic resonance convergent coupled-cluster linear response theory. *J. Chem. Theory Comput.* **2012**, *8*, 1616−1628.

(29) List, N. H.; Coriani, S.; Christiansen, O.; Kongsted, J. Identifying the Hamiltonian structure in linear response theory. *J. Chem. Phys.* **2014**, *140*, 224103.

(30) Peng, B.; Lestrange, P. J.; Goings, J. J.; Caricato, M.; Li, X. Energy-Specific Equation-of-Motion Coupled-Cluster Methods for High-Energy Excited States: Application to K -edge X-ray Absorption Spectroscopy. *J. Chem. Theory Comput.* **2015**, *11*, 4146−4153.

(31) Myhre, R. H.; Coriani, S.; Koch, H. Near-Edge X-ray Absorption Fine Structure within Multilevel Coupled Cluster Theory. *J. Chem. Theory Comput.* **2016**, *12*, 2633−2643.

(32) Besley, N. A.; Gilbert, A. T. B.; Gill, P. M. W. Self-consistent-field calculations of core excited states. *J. Chem. Phys.* **2009**, *130*, 124308.

(33) DeBeer George, S.; Petrenko, T.; Neese, F. Prediction of Iron K-Edge Absorption Spectra Using Time-Dependent Density Functional Theory †. *J. Phys. Chem. A* **2008**, *112*, 12936−12943.

(34) Roper, I. P. E.; Besley, N. A. The effect of basis set and exchange-correlation functional on time-dependent density functional theory calculations within the Tamm-Dancoff approximation of the x-ray emission spectroscopy of transition metal complexes. *J. Chem. Phys.* **2016**, *144*, 114104.

(35) Zhang, Y.; Mukamel, S.; Khalil, M.; Govind, N. Simulating Valence-to-Core X-ray Emission Spectroscopy of Transition Metal Complexes with Time-Dependent Density Functional Theory. *J. Chem. Theory Comput.* **2015**, *11*, 5804−5809.

(36) Onida, G.; Reining, L.; Rubio, A. Electronic excitations: Density-functional versus many-body Green's-function approaches. *Rev. Mod. Phys.* **2002**, *74*, 601−659.

(37) Wu, Q.; van Voorhis, T. Constrained Density Functional Theory and Its Application in Long-Range Electron Transfer. *J. Chem. Theory Comput.* **2006**, *2*, 765−774.

(38) Evangelista, F. A.; Shushkov, P.; Tully, J. C. Orthogonality Constrained Density Functional Theory for Electronic Excited States. *J. Phys. Chem. A* **2013**, *117*, 7378−7392.

(39) Derricotte, W. D.; Evangelista, F. A. Simulation of X-ray absorption spectra with orthogonality constrained density functional theory. *Phys. Chem. Chem. Phys.* **2015**, *17*, 14360−14374.

(40) Krewald, V.; Retegan, M.; Cox, N.; Messinger, J.; Lubitz, W.; DeBeer, S.; Neese, F.; Pantazis, D. A. Metal oxidation states in biological water splitting. *Chem. Sci.* **2015**, *6*, 1676−1695.

(41) Riefer, A.; Rauls, E.; Schmidt, W. G.; Eberhard, J.; Stoll, I.; Mattay, J. 2-Aminopyrimidine-silver(I) based organic semiconductors: Electronic structure and optical response. *Phys. Rev. B: Condens. Matter Mater. Phys.* **2012**, *85*, 165202.

(42) Chandrasekaran, P.; Stieber, S. C. E.; Collins, T. J.; Que, L., Jr.; Neese, F.; DeBeer, S. Prediction of high-valent iron K-edge absorption spectra by time-dependent Density Functional Theory. *Dalton Trans.* **2011**, *40*, 11070−11079.

(43) Lanczos, C. Solution of systems of linear equations by minimized iterations. *J. Res. Natl. Bur. Stand.* **1952**, *49*, 33−53.

(44) Haydock, R.; Heine, V.; Kelly, M. J. Electronic structure based on the local atomic environment for tight-binding bands. II. *J. Phys. C: Solid State Phys.* **1975**, *8*, 2591−2605.

(45) Walker, B.; Gebauer, R. Ultrasoft pseudopotentials in time-dependent density-functional theory. *J. Chem. Phys.* **2007**, *127*, 164106.

(46) Giannozzi, P.; Baroni, S.; Bonini, N.; Calandra, M.; Car, R.; Cavazzoni, C.; Ceresoli, D.; Chiarotti, G. L.; Cococcioni, M.; Dabo, I.; Dal Corso, A.; de Gironcoli, S.; Fabris, S.; Fratesi, G.; Gebauer, R.; Gerstmann, U.; Gougoussis, C.; Kokalj, A.; Lazzeri, M.; Martin-Samos, L.; Marzari, N.; Mauri, F.; Mazzarello, R.; Paolini, S.; Pasquarello, A.; Paulatto, L.; Sbraccia, C.; Scandolo, S.; Sclauzero, G.; Seitsonen, A. P.; Smogunov, A.; Umari, P.; Wentzcovitch, R. M. QUANTUM ESPRESSO: a modular and open-source software project for quantum simulations of materials. *J. Phys.: Condens. Matter* **2009**, *21*, 395502.

(47) Taillefumier, M.; Cabaret, D.; Flank, A.-M.; Mauri, F. X-ray absorption near-edge structure calculations with the pseudopotentials: Application to the K edge in diamond and *α* -quartz. *Phys. Rev. B: Condens. Matter Mater. Phys.* **2002**, *66*, 195107.

(48) Gougoussis, C.; Calandra, M.; Seitsonen, A. P.; Mauri, F. First-principles calculations of x-ray absorption in a scheme based on ultrasoft pseudopotentials: From *α* -quartz to high- T c compoun. *Phys. Rev. B: Condens. Matter Mater. Phys.* **2009**, *80*, 075102.

(49) Buczko, R.; Duscher, G.; Pennycook, S. J.; Pantelides, S. T. Excitonic Effects in Core-Excitation Spectra of Semiconductors. *Phys. Rev. Lett.* **2000**, *85*, 2168−2171.

(50) Gougoussis, C.; Rueff, J.-P.; Calandra, M.; d'Astuto, M.; Jarrige, I.; Ishii, H.; Shukla, A.; Yamada, I.; Azuma, M.; Takano, M. Multiple pre-

edge structures in Cu K -edge x-ray absorption spectra of high- T c cuprates revealed by high-resolution x-ray absorption spectroscopy. *Phys. Rev. B: Condens. Matter Mater. Phys.* **2010**, *81*, 224519.

(51) Gaudry, E.; Cabaret, D.; Brouder, C.; Letard, I.; Rogalev, A.; Wilhlem, F.; Jaouen, N.; Sainctavit, P. Relaxations around the substitutional chromium site in emerald: X-ray absorption experiments and density functional calculations. *Phys. Rev. B: Condens. Matter Mater. Phys.* **2007**, *76*, 094110.

(52) Juhin, A.; Brouder, C.; Arrio, M.-A.; Cabaret, D.; Sainctavit, P.; Balan, E.; Bordage, A.; Seitsonen, A. P.; Calas, G.; Eeckhout, S. G.; Glatzel, P. X-ray linear dichroism in cubic compounds: The case of Cr 3 + in MgAl. *Phys. Rev. B: Condens. Matter Mater. Phys.* **2008**, *78*, 195103.

(53) Cabaret, D.; Mauri, F.; Henderson, G. S. Oxygen K -edge XANES of germanates investigated using first-principles calculations. *Phys. Rev. B: Condens. Matter Mater. Phys.* **2007**, *75*, 184205.

(54) Bunău, O.; Calandra, M. Projector augmented wave calculation of x-ray absorption spectra at the L 2, 3 edges. *Phys. Rev. B: Condens. Matter Mater. Phys.* **2013**, *87*, 205105.

(55) Juhin, A.; de Groot, F.; Vankó, G.; Calandra, M.; Brouder, C. Angular dependence of core hole screening in LiCoO2: A DFT+U calculation of the oxygen and cobalt K -edge x-ray absorption spectra. *Phys. Rev. B: Condens. Matter Mater. Phys.* **2010**, *81*, XX.

(56) Hoffmann, A.; Stanek, J.; Dicke, B.; Peters, L.; Wetzel, A.; Grimm-Lebsanft, B.; Jesser, A.; Bauer, M.; Gnida, M.; Meyer-Klaucke, W.; Rübhausen, M.; Herres-Pawlis, S. Implications of guanidine substitution on copper complexes as entatic state models. *Eur. J. Inorg. Chem.* **2016**, *2016*, 4731.

(57) Neese, F. The ORCA program system. *Wiley Interdiscip. Rev.-Comput. Mol. Sci.* **2012**, *2*, 73−78.

(58) DeBeer George, S.; Petrenko, T.; Neese, F. Time-dependent density functional calculations of ligand K-edge X-ray absorption spectra. *Inorg. Chim. Acta* **2008**, *361*, 965−972.

(59) DeBeer George, S.; Neese, F. Calibration of scalar relativistic density functional theory for the calculation of sulfur K-edge X-ray absorption spectra. *Inorg. Chem.* **2010**, *49*, 1849−1853.

(60) Neese, F. Prediction and interpretation of the 57Fe isomer shift in Mössbauer spectra by density functional theory. *Inorg. Chim. Acta* **2002**, *337*, 181−192.

(61) Schäfer, A.; Horn, H.; Ahlrichs, R. Fully optimized contracted Gaussian basis sets for atoms Li to Kr. *J. Chem. Phys.* **1992**, *97*, 2571.

(62) Schäfer, A.; Huber, C.; Ahlrichs, R. Fully optimized contracted Gaussian basis sets of triple zeta valence quality for atoms Li to Kr. *J. Chem. Phys.* **1994**, *100*, 5829−5835.

(63) Weigend, F.; Ahlrichs, R. Balanced basis sets of split valence, triple zeta valence and quadruple zeta valence quality for H to Rn: Design and assessment of accuracy. *Phys. Chem. Chem. Phys.* **2005**, *7*, 3297−3305.

(64) Staroverov, V. N.; Scuseria, G. E.; Tao, J.; Perdew, J. P. Comparative assessment of a new nonempirical density functional: Molecules and hydrogen-bonded complexes. *J. Chem. Phys.* **2003**, *119*, 12129−12137.

(65) Jesser, A.; Rohrmüller, M.; Schmidt, W. G.; Herres-Pawlis, S. Geometrical and optical benchmarking of copper guanidine-quinoline complexes: Insights from TD-DFT and many-body perturbation theory. *J. Comput. Chem.* **2014**, *35*, 1−17.

(66) Hoffmann, A.; Grunzke, R.; Herres-Pawlis, S. Insights into the influence of dispersion correction in the theoretical treatment of guanidine-quinoline copper(I) complexes. *J. Comput. Chem.* **2014**, *35*, 1943−1950.

(67) Hoffmann, A.; Rohrmüller, M.; Jesser, A.; dos Santos Vieira, I.; Schmidt, W. G.; Herres-Pawlis, S. Geometrical and optical benchmarking of copper(II) guanidine-quinoline complexes: insights from TD-DFT and many-body perturbation theory (part II). *J. Comput. Chem.* **2014**, *35*, 2146−2161.

(68) Witte, M.; Gerstmann, U.; Neuba, A.; Henkel, G.; Schmidt, W. G. Density functional theory of the Cu A -like Cu 2 S 2 diamond core in Cu 2II(NGuaS) 2 Cl 2. *J. Comput. Chem.* **2016**, *37*, 1005−1018.

(69) Grimme, S.; Antony, J.; Ehrlich, S.; Krieg, H. A consistent and accurate ab initio parametrization of density functional dispersion correction (DFT-D) for the 94 elements H-Pu. *J. Chem. Phys.* **2010**, *132*, 154104.

(70) Grimme, S.; Ehrlich, S.; Goerigk, L. Effect of the damping function in dispersion corrected density functional theory. *J. Comput. Chem.* **2011**, *32*, 1456−1465.

(71) Becke, A. D. A new mixing of Hartree−Fock and local density-functional theories. *J. Chem. Phys.* **1993**, *98*, 1372.

(72) Becke, A. D. Density-functional thermochemistry.III. The role of exact exchange. *J. Chem. Phys.* **1993**, *98*, 5648.

(73) Lee, C.; Yang, W.; Parr, R. G. Development of the Colle-Salvetti correlation-energy formula into a functional of the electron density. *Phys. Rev. B: Condens. Matter Mater. Phys.* **1988**, *37*, 785−789.

(74) Vosko, S. H.; Wilk, L.; Nusair, M. Accurate spin-dependent electron liquid correlation energies for local spin density calculations: a critical analysis. *Can. J. Phys.* **1980**, *58*, 1200−1211.

(75) Becke, A. D. Density-functional exchange-energy approximation with correct asymptotic behavior. *Phys. Rev. A: At., Mol., Opt. Phys.* **1988**, *38*, 3098−3100.

(76) Perdew, J. P. Density-functional approximation for the correlation energy of the inhomogeneous electron gas. *Phys. Rev. B: Condens. Matter Mater. Phys.* **1986**, *33*, 8822−8824.

(77) Perdew, J. P.; Burke, K.; Ernzerhof, M. Generalized Gradient Approximation Made Simple. *Phys. Rev. Lett.* **1996**, *77*, 3865−3868.

(78) Neese, F.; Wennmohs, F.; Hansen, A.; Becker, U. Efficient, approximate and parallel Hartree-Fock and hybrid DFT calculations. A 'chain-of-spheres' algorithm for the Hartree-Fock exchange. *Chem. Phys.* **2009**, *356*, 98−109.

(79) Neese, F. An improvement of the resolution of the identity approximation for the formation of the Coulomb matrix. *J. Comput. Chem.* **2003**, *24*, 1740−1747.

(80) Delgado-Jaime, M. U.; DeBeer, S. Expedited analysis of DFT outputs: Introducing moanalyzer. *J. Comput. Chem.* **2012**, *33*, 2180−2185.

(81) Bunău, O.; Joly, Y. Self-consistent aspects of x-ray absorption calculations. *J. Phys.: Condens. Matter* **2009**, *21*, 345501.

(82) Pasquali, M.; Floriani, C.; Venturi, G.; Gaetani-Manfredotti, A.; Chiesi-Villa, A. Copper(I)-carbon monoxide chemistry: genesis and chemical and structural properties of copper(I) terminal and bridging carbonyls. *J. Am. Chem. Soc.* **1982**, *104*, 4092−4099.

(83) York, J. T.; Brown, E. C.; Tolman, W. B. Characterization of a Complex Comprising a {Cu2(S2)2}2+ Core: Bis(μ-S22−)dicopper(III) or Bis(μ-S2.−)dicopper(II)? *Angew. Chem., Int. Ed.* **2005**, *44*, 7745−7748.

(84) Yang, L.; Powell, D. R.; Houser, R. P. Structural variation in copper(i) complexes with pyridylmethylamide ligands: structural analysis with a new four-coordinate geometry index, τ_4. *Dalton Trans.* **2007**, 955−964.

(85) Johann, H. H. Die Erzeugung lichtstarker Röntgenspektren mit Hilfe von Konkavkristallen. *Eur. Phys. J. A* **1931**, *69*, 185−206.

(86) Hämäläinen, K.; Siddons, D. P.; Hastings, J. B.; Berman, L. E. Elimination of the inner-shell lifetime broadening in x-ray-absorption spectroscopy. *Phys. Rev. Lett.* **1991**, *67*, 2850−2853.

(87) Carra, P.; Fabrizio, M.; Thole, B. T. High Resolution X-Ray Resonant Raman Scattering. *Phys. Rev. Lett.* **1995**, *74*, 3700−3703.

(88) Loeffen, P. W.; Pettifer, R. F.; Müllender, S.; van Veenendaal, M. A.; Röhler, J.; Sivia, D. S. Deconvolution of lifetime broadening at rare-earth LIII edges compared to resonant inelastic x-ray scattering measurements. *Phys. Rev. B: Condens. Matter Mater. Phys.* **1996**, *54*, 14877−14880.

(89) Tanaka, S.; Okada, K.; Kotani, A. Resonant X-Ray Emission Spectroscopy in Dy Compounds. *J. Phys. Soc. Jpn.* **1994**, *63*, 2780−2787.

(90) Kau, L. S.; Spira-Solomon, D. J.; Penner-Hahn, J. E.; Hodgson, K. O.; Solomon, E. I. X-ray absorption edge determination of the oxidation state and coordination number of copper. Application to the type 3 site in Rhus vernicifera laccase and its reaction with oxygen. *J. Am. Chem. Soc.* **1987**, *109*, 6433−6442.

(91) Sarangi, R.; Yang, L.; Winikoff, S. G.; Gagliardi, L.; Cramer, C. J.; Tolman, W. B.; Solomon, E. I. X-ray absorption spectroscopic and

computational investigation of a possible S···S interaction in the [Cu3S2]3+ core. *J. Am. Chem. Soc.* **2011**, *133*, 17180−17191.

(92) Tomson, N. C.; Williams, K. D.; Dai, X.; Sproules, S.; DeBeer, S.; Warren, T. H.; Wieghardt, K. Re-evaluating the Cu K pre-edge XAS transition in complexes with covalent metal−ligand interactions. *Chem. Sci.* **2015**, *6*, 2474−2487.

(93) Walroth, R. C.; Uebler, J. W. H.; Lancaster, K. M. Probing Cu I in homogeneous catalysis using high-energy-resolution fluorescence-detected X-ray absorption spectroscopy. *Chem. Commun.* **2015**, *51*, 9864−9867.

(94) Ray, K.; Petrenko, T.; Wieghardt, K.; Neese, F. Joint spectroscopic and theoretical investigations of transition metal complexes involving non-innocent ligands. *Dalton transactions (Cambridge, England: 2003)* **2007**, 1552−1566.

(95) Ressler, T.; Wong, J.; Roos, J.; Smith, I. L. Quantitative speciation of mn-bearing particulates emitted from autos burning (methylcyclopentadienyl) manganese tricarbonyl-added gasolines using XANES spectroscopy. *Environ. Sci. Technol.* **2000**, *34*, 950−958.

(96) Datta, S.; Rule, A. M.; Mihalic, J. N.; Chillrud, S. N.; Bostick, B. C.; Ramos-Bonilla, J. P.; Han, I.; Polyak, L. M.; Geyh, A. S.; Breysse, P. N. Use of X-ray Absorption Spectroscopy To Speciate Manganese in Airborne Particulate Matter from Five Counties Across the United States. *Environ. Sci. Technol.* **2012**, *46*, 3101−3109.

(97) Bressler, C.; Chergui, M. Ultrafast X-ray Absorption Spectroscopy. *Chem. Rev.* **2004**, *104*, 1781−1812.

(98) Canton, S. E.; Kjær, K. S.; Vankó, G.; van Driel, T. B.; Adachi, S.-i.; Bordage, A.; Bressler, C.; Chabera, P.; Christensen, M.; Dohn, A. O.; Galler, A.; Gawelda, W.; Gosztola, D.; Haldrup, K.; Harlang, T.; Liu, Y.; Møller, K. B.; Németh, Z.; Nozawa, S.; Pápai, M.; Sato, T.; Sato, T.; Suarez-Alcantara, K.; Togashi, T.; Tono, K.; Uhlig, J.; Vithanage, D. A.; Wärnmark, K.; Yabashi, M.; Zhang, J.; Sundström, V.; Nielsen, M. M. Visualizing the non-equilibrium dynamics of photoinduced intramolecular electron transfer with femtosecond X-ray pulses. *Nat. Commun.* **2015**, *6*, 6359.

(99) Milne, C. J.; Pham, V.-T.; Gawelda, W.; van der Veen, R. M.; Nahhas, A. E.; Johnson, S. L.; Beaud, P.; Ingold, G.; Lima, F.; Vithanage, D. A.; Benfatto, M.; Grolimund, D.; Borca, C.; Kaiser, M.; Hauser, A.; Abela, R.; Bressler, C.; Chergui, M. Time-resolved x-ray absorption spectroscopy: Watching atoms dance. *J. Phys. Conf. Ser.* **2009**, *190*, 012052.

(100) Penfold, T. J.; Karlsson, S.; Capano, G.; Lima, F. A.; Rittmann, J.; Reinhard, M.; Rittmann-Frank, M. H.; Braem, O.; Baranoff, E.; Abela, R.; Tavernelli, I.; Rothlisberger, U.; Milne, C. J.; Chergui, M. Solvent-Induced Luminescence Quenching: Static and Time-Resolved X-Ray Absorption Spectroscopy of a Copper(I) Phenanthroline Complex. *J. Phys. Chem. A* **2013**, *117*, 4591−4601.

Supporting Information

Experimental and theoretical high-energy resolution X-ray absorption spectroscopy: Implications for the investigation of the entatic state

Nora Jenny Vollmers,[‡,#,] *Patrick Müller,*[†,#] *Alexander Hoffmann,*[§] *Sonja Herres-Pawlis,*[§] *Martin Rohrmüller,*[‡] *Wolf Gero Schmidt,*[‡] *Uwe Gerstmann,*[*,‡] *Matthias Bauer*[*,†]

[†]Universität Paderborn, Department Chemie, Warburger Straße 100, D-33098 Paderborn, Germany

[‡]Universität Paderborn, Department Physik, Warburger Straße 100, D-33098 Paderborn, Germany

[§]RWTH Aachen University, Institut für Anorganische Chemie, Landoltweg 1, D-52074 Aachen, Germany

*Corresponding Authors: matthias.bauer@uni-paderborn.de, uwe.gerstmann@uni-paderborn.de

Table of Contents

Section S1 – RIXS planes

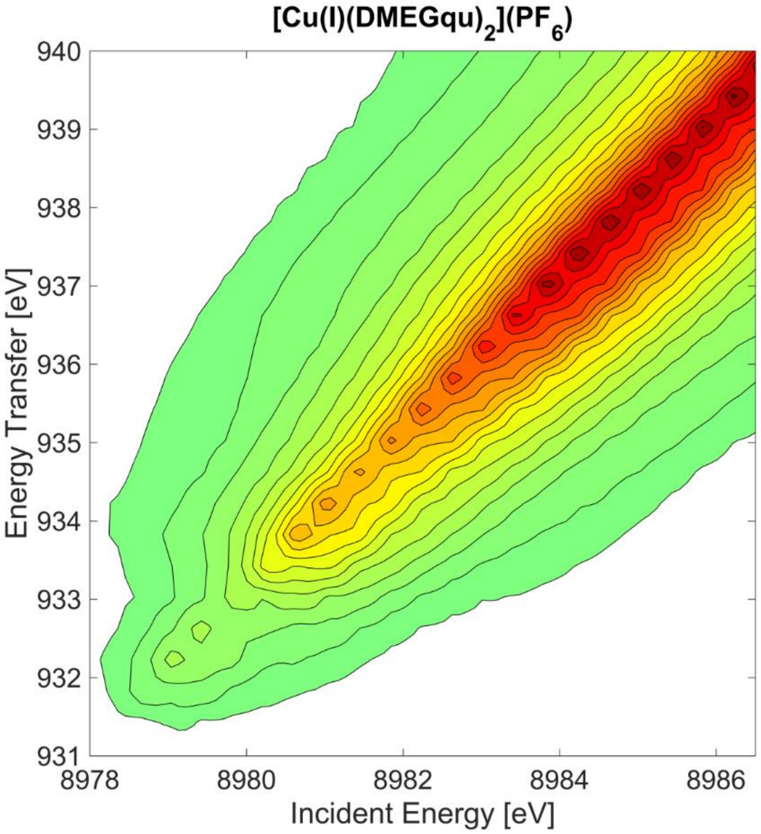

Figure S1: RIXS Plane of [Cu(I)(DMEGqu)2](PF6)

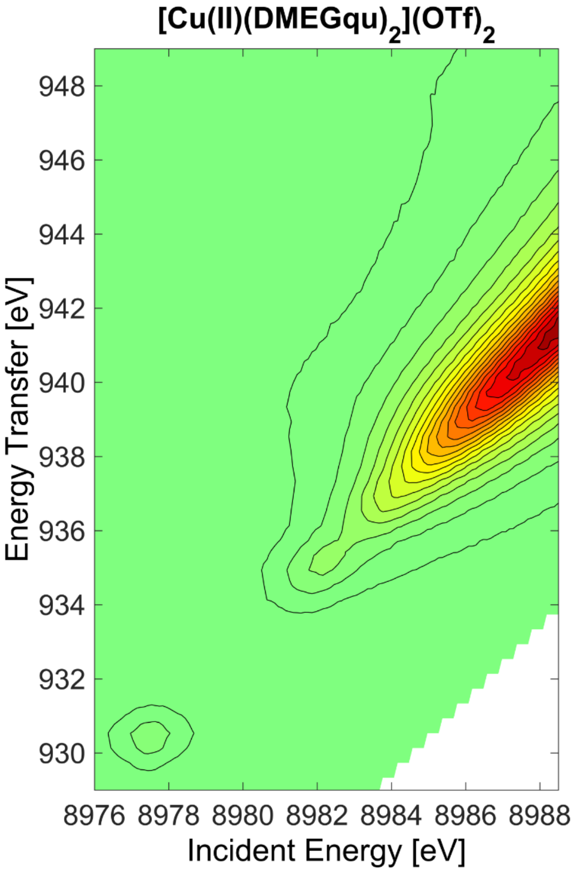

Figure S2: RIXS Plane of $[Cu(II)(DMEGqu)_2](OTf)_2$

Section S2 – Additional calculated spectra

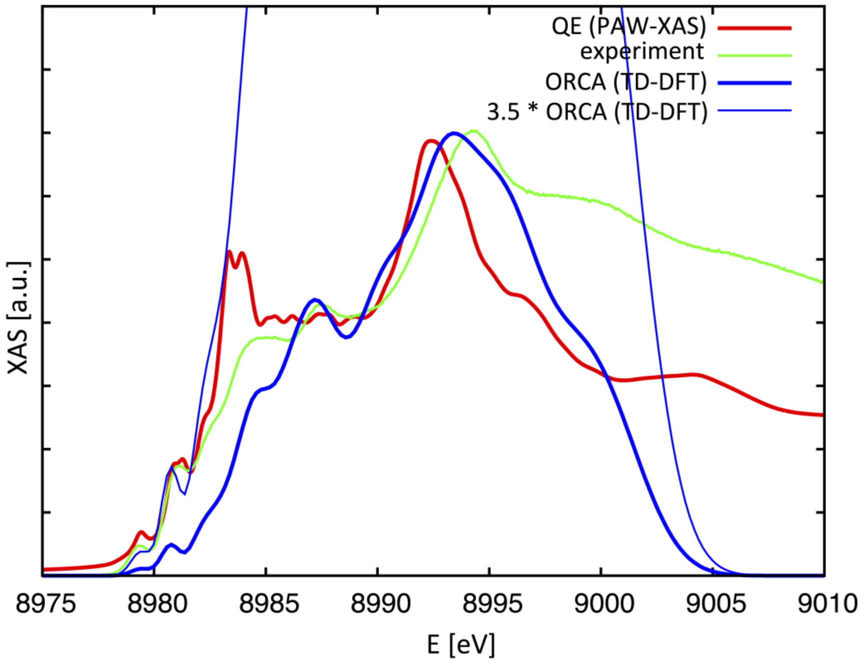

Figure S3: Direct comparison of the two theoretical methods taking the Cu(I) species as an example. For better comparison, the data is calculated for technical settings, which can be realized equally well within both methods: PBE functional, relaxed gas phase geometry (i.e. isolated molecule); the ORCA (TD-DFT) values are given twice, with intensitys calings fitting the data best (i) in the rising edge (thin line) and (ii) at higher energies between 8987 and 8997 eV (thick line). For further comparison, the experimental data is also given.

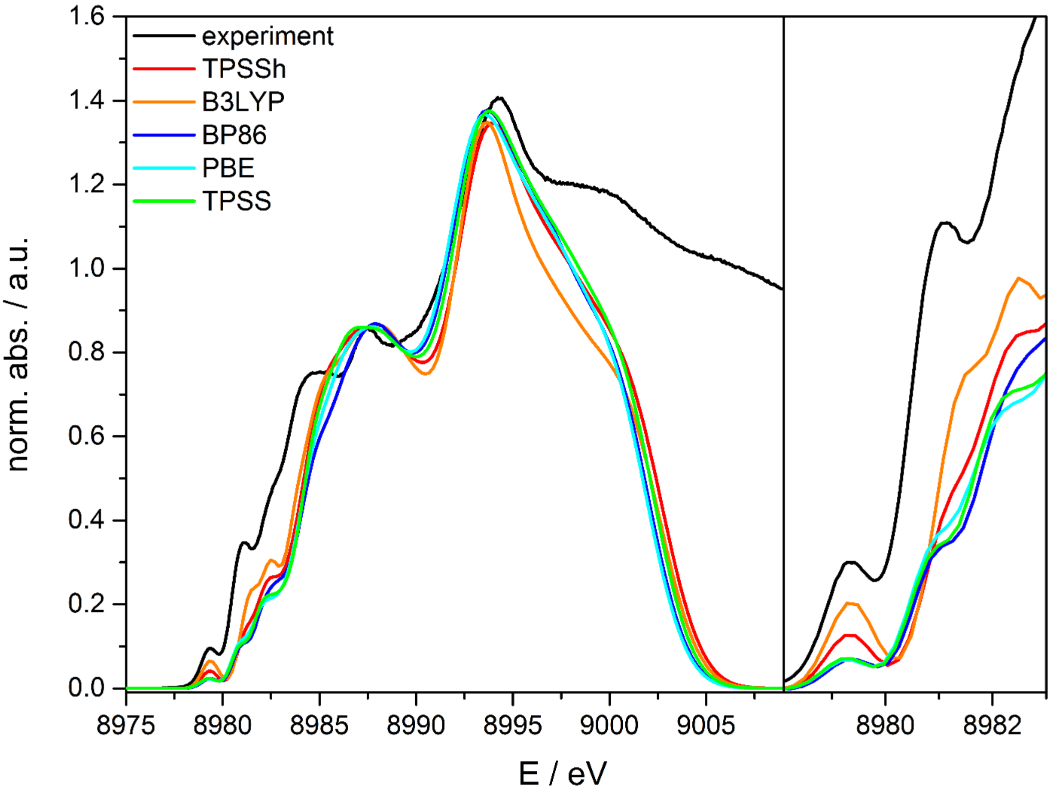

Figure S4: Calculated **Cu(I)** spectra for different XC functionals for the **experimental crystal structure**. The intensity of the spectra is normalized to the intensity of the 8987 eV peak.

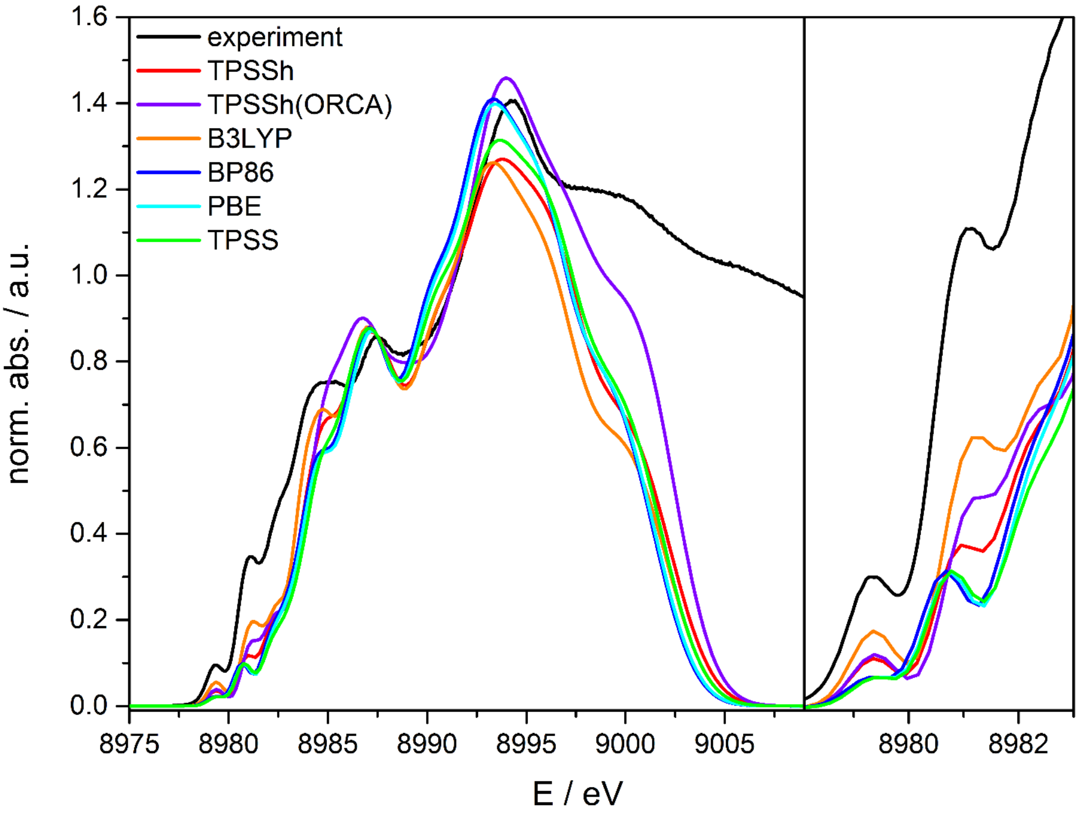

Figure S5: Calculated **Cu(I)** spectra for different XC functionals for the **QE gas phase structure.** For the comparison with the **ORCA gas phase structure** only TPSSh was used. The intensity of the spectra is normalized to the intensity of the 8987 eV peak.

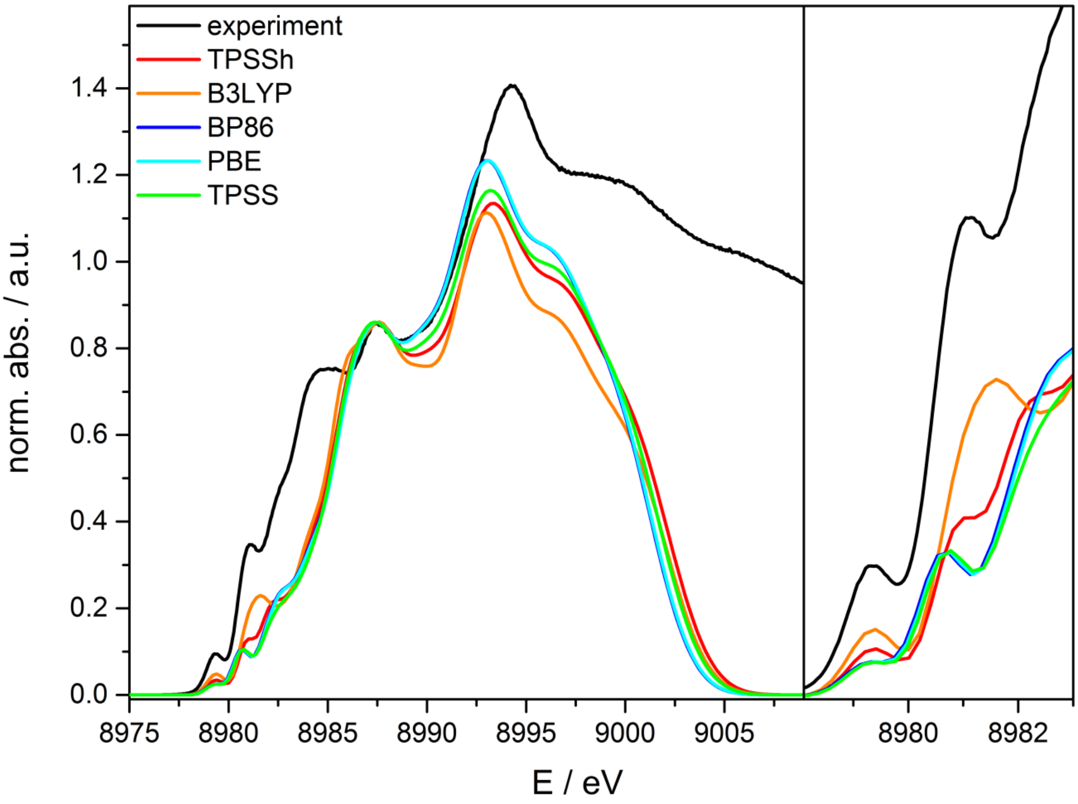

Figure S6: Calculated **Cu(I)** spectra for different XC functionals for the **QE relaxed solid structure**. The intensity of the spectra is normalized to the intensity of the 8987 eV peak.

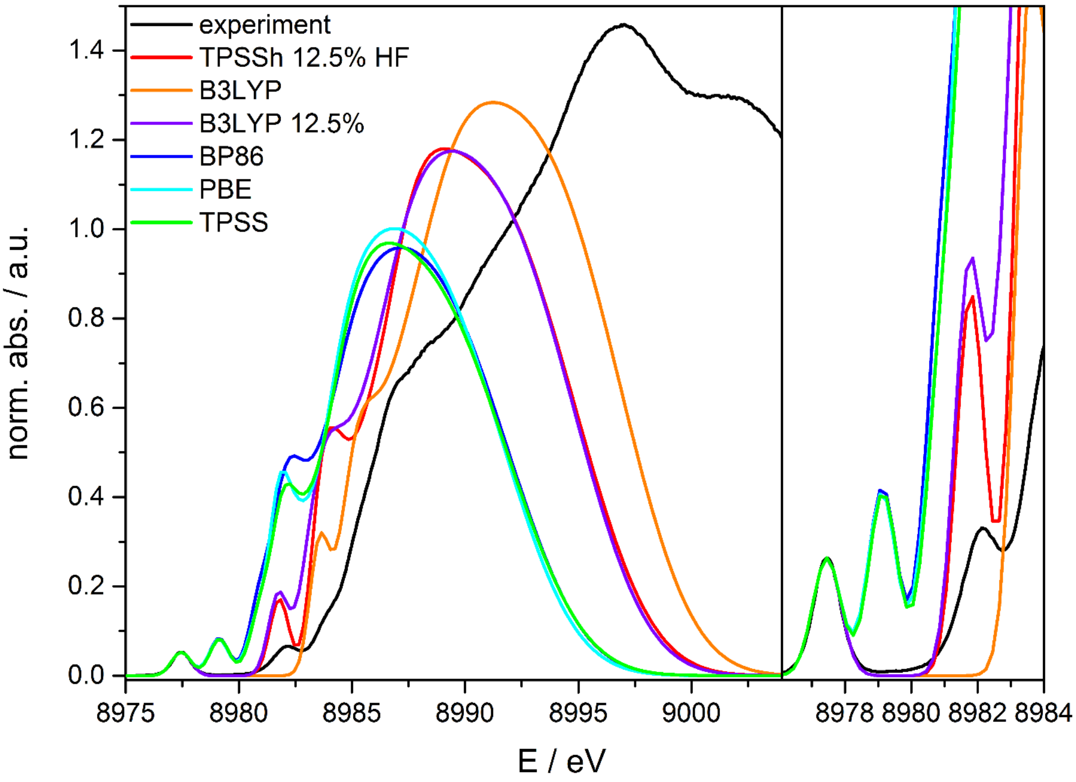

Figure S7: Calculated **Cu(II)** spectra for different XC functionals for the **experimental crystal structure.** The intensity of the spectra is normalized to the intensity of the pre-peak at 8977.5 eV.

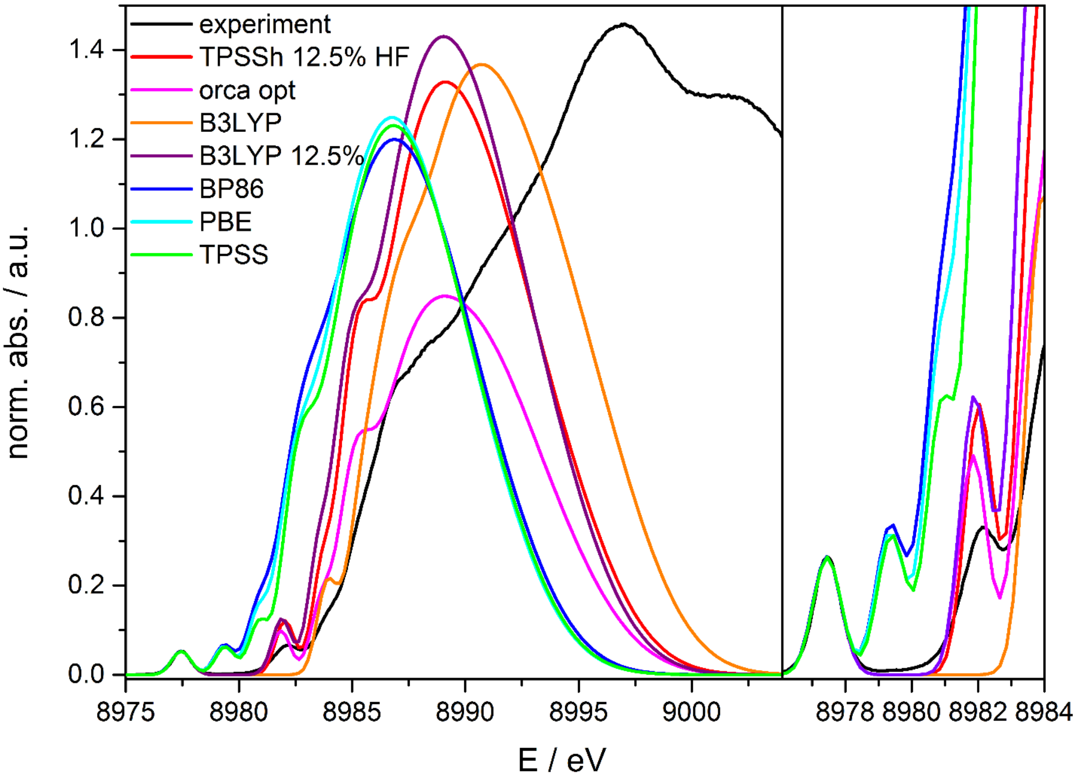

Figure S8: Calculated **Cu(II)** spectra for different XC functionals for the **QE gas phase structure.** For the comparison with the **ORCA gas phase structure** only TPSSh was used. The intensity of the spectra is normalized to the intensity of the pre-peak at 8977.5 eV.

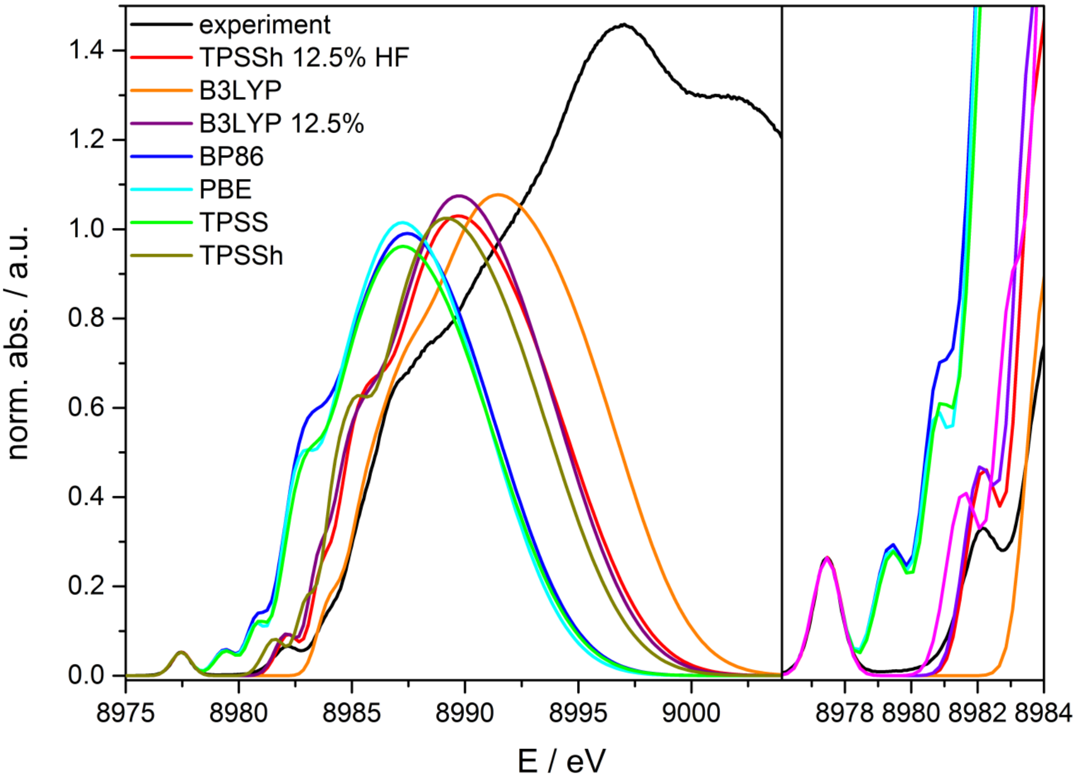

Figure S9: Calculated **Cu(II)** spectra for different XC functionals for the **QE relaxed solid structure** including the unadjusted TPSSh. The intensity of the spectra is normalized to the intensity of the pre-peak at 8977.5 eV.

Section S3 - Acceptor orbital contributions of selected transitions

Table S1: Acceptor Orbital contributions for the different **Cu(I)** transitions.

Acceptor orbital contributions	Cu		N		C	
transition	p	d	s	p	s	p
1s -> 3d	2.3%	55%	2.90%	20.70%	0.00%	6.90%
1s -> π*	0.70%	0.40%	0.00%	14.20%	0.00%	56.90%
1s -> 4p	22.80%	0.40%	0.60%	3.50%	8.30%	24.20%

Table S2: Acceptor orbital contributions for the different **Cu(II)** transitions.

Acceptor orbital contributions	Cu		N		C	
transition	p	d	s	p	s	p
1s -> π*	0.60%	1.80%	0.00%	14.50%	0.00%	56.10%
1s -> 4p	16.80%	1.20%	1.80%	2.90%	8.00%	15.20%

Section S4 - Geometric parameters of the extreme case models

The following values are obtained for the strongly constrained, hypothetical structures in square planar and tetrahedral geometries. These structures result from constrained geometry optimizations where all N-Cu-N angles besides the chelate angles are fixed. This procedure leads to changes in bond lengths, especially in the square planar case of Cu(I). Although these changes are significant if taken separately they do not change the overall result considering the "recovery" of spectral features by mixing the respective spectra.

Table S3: Bond lengths and torsion angle of the tetrahedral and square planar **Cu(I)** geometries

Cu(I)	tetrahedral	square planar
Cu-N_{qu}	2.034, 2.023	1.918, 1.919
Cu-$N_{imine,gua}$	2.024, 2.038	2.386, 2.394
∠ CuN_2 CuN'_2	89.7	0

Table S4: Bond lengths and torsion angle of the tetrahedral and square planar **Cu(II)** geometries

Cu(II)	tetrahedral	square planar
Cu-N_{qu}	1.965, 2.072	2.012, 2.001
Cu-$N_{imine,gua}$	1.956, 1.955	1.995, 1.990
∠ CuN_2 CuN_2'	89.7	0

Section S5 - XYZ coordinates

Cu(I)DMEGqu (gas phase QE)

Cu	0.000000	0.000000	0.000000
N	-0.845166	1.749195	0.991033
N	-1.908488	2.138623	3.172568
N	0.296219	1.626335	3.057221
N	-1.347964	0.546911	-1.397483
N	2.080805	0.131429	-0.642422
N	3.221950	-0.132381	-2.803543
N	1.848988	1.635698	-2.450776
N	0.811611	-1.365863	1.242622
C	-0.845228	1.859802	2.315110
C	-3.279716	1.701839	2.857500
H	-3.548173	1.981354	1.834474
H	-3.968319	2.200433	3.552969
H	-3.376775	0.607403	2.978440
C	-1.469935	1.880633	4.569135
H	-1.781465	0.863080	4.869676
H	-1.913658	2.610629	5.258583
C	0.059557	1.986443	4.468440
H	0.412618	3.017288	4.657663
H	0.585835	1.298948	5.144393
C	1.646137	1.784333	2.506900
H	1.636766	1.522755	1.442081
H	2.330205	1.107279	3.036902
H	1.998072	2.824787	2.630002
C	-1.761220	2.376475	0.140437
C	-2.379864	3.610843	0.388733
H	-2.210590	4.101217	1.347987
C	-3.207059	4.226429	-0.580615
H	-3.667622	5.187063	-0.345466
C	-3.433720	3.634735	-1.815857
H	-4.072076	4.110083	-2.561649
C	-2.818335	2.387989	-2.121592
C	-1.979796	1.754391	-1.143041
C	-2.988538	1.728955	-3.373023
H	-3.623224	2.188082	-4.133216
C	-2.349052	0.523005	-3.607944
H	-2.464175	-0.005016	-4.554435
C	-1.533263	-0.036090	-2.597104
H	-1.016543	-0.984207	-2.752219
C	2.398789	0.506098	-1.876992
C	3.331319	-1.601086	-2.844589
H	3.524832	-2.001804	-1.845228
H	4.171460	-1.865661	-3.500772
H	2.405092	-2.048966	-3.248684
C	1.348436	2.764159	-1.659782
H	0.939498	2.390339	-0.713499
H	0.550204	3.268802	-2.221432
H	2.159253	3.486427	-1.453716
C	2.501142	1.909623	-3.745555
H	3.316059	2.644603	-3.608227
H	1.780938	2.306822	-4.473631
C	3.042500	0.522832	-4.125637
H	2.303337	-0.045781	-4.719851
H	3.992393	0.560314	-4.674659
C	2.876860	-0.682999	0.169552
C	4.278541	-0.730529	0.138103
H	4.807828	-0.156500	-0.623237
C	5.008830	-1.500579	1.074186
H	6.098041	-1.508949	1.012855
C	4.366281	-2.233751	2.062544
H	4.930374	-2.827848	2.782592
C	2.945363	-2.208154	2.145066
C	2.195700	-1.432350	1.197249
C	2.216583	-2.919610	3.141048
H	2.762327	-3.519287	3.871822
C	0.834087	-2.840265	3.169861
H	0.250798	-3.376613	3.918199
C	0.165881	-2.050239	2.205898
H	-0.921878	-1.968162	2.202552

S14

Cu(I)DMEGqu (gas phase ORCA)

Cu	0.000000	0.000000	0.000000
N	-0.868213	1.658091	0.973738
N	-1.996887	1.871867	3.094340
N	0.212390	1.572284	3.047323
N	-1.335146	0.454791	-1.379691
N	2.010449	0.132049	-0.623389
N	3.061238	-0.221921	-2.764878
N	1.818250	1.600045	-2.435400
N	0.747433	-1.370328	1.207302
C	-0.906207	1.725023	2.283402
C	-3.343908	1.496231	2.685301
H	-3.311168	0.968251	1.733698
H	-3.987716	2.371453	2.578037
H	-3.767667	0.834193	3.443813
C	-1.605406	1.691611	4.495655
H	-1.882512	0.684299	4.828709
H	-2.096355	2.420073	5.141382
C	-0.088170	1.869739	4.444073
H	0.206749	2.899344	4.682349
H	0.441487	1.192021	5.114451
C	1.548556	1.802369	2.530796
H	1.568813	1.535257	1.475722
H	2.254688	1.171657	3.071834
H	1.842945	2.852305	2.647746
C	-1.813754	2.240163	0.142542
C	-2.479843	3.430876	0.397152
H	-2.314117	3.938432	1.339884
C	-3.348012	3.996972	-0.551957
H	-3.847887	4.927985	-0.311651
C	-3.562345	3.400044	-1.771516
H	-4.231030	3.840691	-2.500992
C	-2.891575	2.196241	-2.084512
C	-2.016713	1.614661	-1.126573
C	-3.037559	1.528570	-3.322540
H	-3.698464	1.944644	-4.074524
C	-2.343250	0.368055	-3.556129
H	-2.438359	-0.167270	-4.492260
C	-1.497944	-0.137089	-2.555193
H	-0.940269	-1.052811	-2.711932
C	2.312546	0.470149	-1.854500
C	3.251801	-1.665036	-2.699646
H	2.599474	-2.093661	-1.940442
H	4.285210	-1.921480	-2.458304
H	2.996374	-2.094957	-3.670676
C	1.346045	2.733499	-1.662552
H	0.920505	2.370530	-0.728690
H	0.572811	3.254745	-2.227877
H	2.162997	3.431949	-1.444455
C	2.454459	1.818731	-3.730423
H	3.274042	2.541423	-3.631011
H	1.740697	2.200617	-4.461131
C	2.972601	0.423479	-4.078489
H	2.263623	-0.124462	-4.710531
H	3.942075	0.442694	-4.576800
C	2.795019	-0.697370	0.164369
C	4.181297	-0.756023	0.132902
H	4.719422	-0.163120	-0.596955
C	4.897255	-1.554207	1.041423
H	5.979153	-1.570599	0.981208
C	4.253920	-2.297922	2.001984
H	4.809792	-2.910425	2.701469
C	2.843933	-2.255653	2.086103
C	2.112982	-1.455229	1.166147
C	2.104856	-2.971177	3.056491
H	2.631601	-3.592423	3.772028
C	0.736422	-2.870028	3.081055
H	0.144104	-3.409407	3.809194
C	0.093340	-2.054641	2.135938
H	-0.985987	-1.958873	2.130644

S15

Cu(I)DMEGqu (solid relaxed QE)

Cu	0.000000	0.000000	0.000000
N	-1.114045	1.686906	0.560236
N	-2.801135	2.271754	2.230856
N	-0.824611	1.423046	2.886065
N	-1.056071	0.200827	-1.716136
N	1.944167	0.281325	-0.737014
N	2.844924	0.532764	-3.003984
N	1.585733	2.170693	-2.110341
N	0.961123	-1.056001	1.392410
C	-1.577571	1.845741	1.791913
C	-3.974456	2.625675	1.453545
H	-3.858314	2.319225	0.415334
H	-4.141285	3.714588	1.493398
H	-4.847243	2.108399	1.866258
C	-2.985455	1.974963	3.651912
H	-3.649150	1.096656	3.747208
H	-3.464496	2.821252	4.170230
C	-1.551730	1.704565	4.133710
H	-1.114376	2.587741	4.625606
H	-1.488312	0.854259	4.822823
C	0.632011	1.558743	2.926897
H	1.016335	1.537909	1.901830
H	1.072098	0.723578	3.489187
H	0.921062	2.506544	3.417880
C	-1.603899	2.273998	-0.602733
C	-2.042748	3.592445	-0.687850
H	-2.143322	4.157959	0.228097
C	-2.295269	4.199637	-1.930346
H	-2.544875	5.262294	-1.923273
C	-2.192564	3.482846	-3.117246
H	-2.418636	3.953287	-4.071682
C	-1.796636	2.114995	-3.084942
C	-1.479306	1.514709	-1.822127
C	-1.661666	1.296448	-4.243145
H	-1.924945	1.680551	-5.226748
C	-1.206444	-0.006035	-4.117219
H	-1.082533	-0.647749	-4.989857
C	-0.931617	-0.528445	-2.839508
H	-0.627437	-1.567725	-2.719133
C	2.156504	0.939880	-1.878635
C	3.031871	-0.880775	-3.324558
H	3.259038	-1.457008	-2.422097
H	3.875999	-0.957082	-4.023154
H	2.119520	-1.302455	-3.784330
C	1.341688	3.147980	-1.054460
H	1.073661	2.636396	-0.125229
H	0.519409	3.808551	-1.354288
H	2.246453	3.756111	-0.911695
C	2.086459	2.719358	-3.382196
H	2.947239	3.379978	-3.180258
H	1.301169	3.288375	-3.892624
C	2.505690	1.450674	-4.119939
H	1.650096	1.037016	-4.681393
H	3.361457	1.579886	-4.792703
C	2.827562	-0.540275	-0.060412
C	4.190696	-0.694661	-0.330853
H	4.623419	-0.219219	-1.204580
C	5.025020	-1.432548	0.527969
H	6.073906	-1.527668	0.233352
C	4.550738	-2.041720	1.677223
H	5.198498	-2.649744	2.309204
C	3.173521	-1.927104	1.996904
C	2.309856	-1.177937	1.131037
C	2.587915	-2.543679	3.132600
H	3.208115	-3.138107	3.798092
C	1.242184	-2.376194	3.387170
H	0.778309	-2.819403	4.261625
C	0.456813	-1.608036	2.510887
H	-0.595475	-1.416909	2.712590

Cu(I)DMEGqu (exp. crystal structure)

Cu	0.000000	0.000000	0.000000
N	-1.026112	1.599388	0.925925
N	-2.506481	1.726081	2.826023
N	-0.335075	1.384229	3.133899
N	-1.233971	0.434154	-1.486534
N	1.932283	0.052673	-0.902948
N	2.513564	-0.418439	-3.198230
N	1.631578	1.534992	-2.658299
N	0.919469	-1.217181	1.231503
C	-1.307084	1.596802	2.198784
C	-3.777127	1.410201	2.198784
H	-3.618798	1.053838	1.300430
H	-4.321175	2.223137	2.139047
H	-4.248965	0.740932	2.738715
C	-2.362033	1.409026	4.239035
H	-2.659893	0.485077	4.434329
H	-2.876961	2.040754	4.801942
C	-0.876838	1.562597	4.466495
H	-0.658171	2.459348	4.824917
H	-0.535874	0.872980	5.089139
C	1.059529	1.663756	2.881165
H	1.246617	1.558818	1.925372
H	1.615674	1.039487	3.393525
H	1.263264	2.582563	3.154577
C	-1.837373	2.223082	-0.022975
C	-2.472144	3.429454	0.153938
H	-2.447631	3.845140	1.008638
C	-3.151834	4.062519	-0.893758
H	-3.577345	4.896031	-0.737523
C	-3.212511	3.502494	-2.129856
H	-3.680830	3.941004	-2.830618
C	-2.578339	2.268561	-2.366506
C	-1.887060	1.628792	-1.311918
C	-2.566574	1.628102	-3.620985
H	-3.009601	2.028303	-4.358508
C	-1.924722	0.445108	-3.777220
H	-1.921323	0.006653	-4.620432
C	-1.269001	-0.119441	-2.681275
H	-0.823222	-0.950764	-2.805344
C	2.054343	0.339114	-2.175807
C	2.564669	-1.865070	-3.175254
H	2.333362	-2.186197	-2.279198
H	3.469428	-2.163084	-3.407310
H	1.925380	-2.223968	-3.825469
C	1.398062	2.693060	-1.831170
H	1.258139	2.408912	-0.902948
H	0.601760	3.167587	-2.150534
H	2.174406	3.289383	-1.877122
C	1.880226	1.641599	-4.069013
H	2.603125	2.292006	-4.250522
H	1.064431	1.921074	-4.551505
C	2.294880	0.248321	-4.471089
H	1.580007	-0.199199	-4.990342
H	3.124541	0.266066	-5.011020
C	2.777836	-0.810630	-0.227460
C	4.104995	-1.039113	-0.530740
H	4.473024	-0.670553	-1.325703
C	4.916498	-1.804332	0.317066
H	5.824704	-1.947785	0.078118
C	4.440985	-2.345434	1.461261
H	5.015061	-2.853873	2.024168
C	3.091482	-2.148440	1.819683
C	2.255215	-1.405682	0.948901
C	2.516862	-2.644907	3.000639
H	3.053312	-3.130942	3.616390
C	1.208359	-2.440502	3.267158
H	0.820953	-2.772152	4.066716
C	0.430407	-1.727803	2.338936
H	-0.495355	-1.611372	2.522743

Cu(I)DMEGqu (tetrahedral)

Cu	0.000000	0.000000	0.000000
N	-1.262641	1.400852	0.771964
N	-2.048184	1.955614	2.985375
N	0.087676	2.322027	2.455345
N	-1.678013	-0.687972	-0.896146
N	1.838661	0.079367	-0.842641
N	2.802649	-0.459735	-2.988183
N	1.355761	1.231038	-2.828888
N	0.879513	-1.346185	1.245474
C	-1.113392	1.872529	1.988424
C	-3.193609	1.057436	3.075082
H	-3.087213	0.238405	2.365145
H	-4.129876	1.578540	2.867206
H	-3.231428	0.646895	4.086317
C	-1.408304	2.396059	4.229200
H	-1.224726	1.530109	4.876546
H	-2.034919	3.108970	4.765424
C	-0.101889	3.007489	3.730642
H	-0.197432	4.089086	3.571460
H	0.736724	2.825079	4.402861
C	1.171155	2.716764	1.576556
H	1.285365	1.969177	0.790599
H	2.090399	2.757912	2.161015
H	0.989217	3.698062	1.122103
C	-2.508142	1.302784	0.148406
C	-3.520736	2.243316	0.258334
H	-3.372938	3.106181	0.896636
C	-4.732124	2.095300	-0.439718
H	-5.497883	2.853114	-0.322979
C	-4.958069	1.013277	-1.256574
H	-5.898346	0.895282	-1.781526
C	-3.944258	0.043050	-1.422907
C	-2.707701	0.198586	-0.738408
C	-4.089841	-1.098209	-2.246192
H	-5.022269	-1.252532	-2.777489
C	-3.055441	-1.992272	-2.362830
H	-3.142398	-2.876831	-2.980894
C	-1.854008	-1.739954	-1.678058
H	-1.008658	-2.412174	-1.776158
C	2.016003	0.261673	-2.131743
C	3.141491	-1.860405	-2.764350
H	2.569201	-2.256805	-1.927242
H	4.204516	-1.986079	-2.550669
H	2.889848	-2.425371	-3.664628
C	0.751320	2.383455	-2.188848
H	0.183541	2.054707	-1.316404
H	0.069637	2.852131	-2.898543
H	1.504375	3.116269	-1.875393
C	1.932046	1.359650	-4.164781
H	2.676994	2.165177	-4.181783
H	1.162368	1.578654	-4.905023
C	2.579800	-0.007809	-4.365479
H	1.902129	-0.702495	-4.876006
H	3.516005	0.041962	-4.921753
C	2.758636	-0.598430	-0.039527
C	4.135753	-0.525825	-0.182948
H	4.552788	0.060683	-0.992763
C	4.997263	-1.198925	0.701076
H	6.067252	-1.117192	0.550285
C	4.507790	-1.952385	1.741214
H	5.174954	-2.480174	2.412018
C	3.111863	-2.031823	1.945932
C	2.235099	-1.337267	1.068016
C	2.522056	-2.775433	2.995225
H	3.160202	-3.323728	3.679095
C	1.157148	-2.794363	3.135740
H	0.679915	-3.359865	3.926029
C	0.368677	-2.049452	2.241233
H	-0.710908	-2.021564	2.343782

Cu(I)DMEGqu (square planar)

Cu	0.000000	0.000000	0.000000
N	-1.088087	1.747950	1.205799
N	-2.030382	1.341325	3.378774
N	-0.311909	2.736511	3.194823
N	-1.189293	0.582083	-1.387360
N	1.092179	-1.753570	-1.208758
N	-0.179727	-3.437576	-2.358294
N	1.067071	-2.033780	-3.544685
N	1.192813	-0.587479	1.384306
C	-1.176407	1.938458	2.503798
C	-2.804470	0.159634	3.052719
H	-2.573814	-0.139823	2.031807
H	-3.875627	0.357737	3.133133
H	-2.537428	-0.652779	3.734547
C	-1.661257	1.642981	4.760399
H	-1.162355	0.775018	5.207513
H	-2.537171	1.887103	5.362772
C	-0.705567	2.832427	4.597634
H	-1.211583	3.788145	4.777223
H	0.159456	2.771381	5.259749
C	0.439738	3.799433	2.552146
H	0.495098	3.571607	1.489268
H	1.446327	3.849073	2.971329
H	-0.052866	4.767452	2.694565
C	-2.228560	1.853876	0.417158
C	-3.359682	2.558954	0.829406
H	-3.375168	2.971321	1.831147
C	-4.460126	2.789105	-0.006383
H	-5.303019	3.349038	0.381701
C	-4.465797	2.343933	-1.304515
H	-5.298423	2.540499	-1.968549
C	-3.350958	1.625872	-1.785514
C	-2.243955	1.338287	-0.928883
C	-3.284143	1.179666	-3.124069
H	-4.110106	1.401036	-3.790772
C	-2.182422	0.495338	-3.566440
H	-2.091987	0.167605	-4.594264
C	-1.157792	0.205882	-2.655590
H	-0.288870	-0.352714	-2.964747
C	0.697402	-2.400332	-2.283266
C	-1.054964	-3.820424	-1.267842
H	-0.889225	-3.143504	-0.431540
H	-0.853641	-4.843980	-0.943879
H	-2.097060	-3.744235	-1.590861
C	2.263790	-1.253908	-3.803295
H	2.523008	-0.728480	-2.885984
H	2.072798	-0.532356	-4.599702
H	3.095343	-1.901511	-4.101863
C	0.558629	-2.984755	-4.529249
H	1.363318	-3.659081	-4.844666
H	0.170673	-2.475299	-5.412607
C	-0.532357	-3.727627	-3.746624
H	-1.532355	-3.333939	-3.963869
H	-0.532350	-4.800651	-3.942309
C	1.590290	-2.464480	-0.122843
C	2.097419	-3.758606	-0.245805
H	2.026418	-4.251844	-1.207845
C	2.728022	-4.432898	0.807688
H	3.101297	-5.435946	0.636949
C	2.902304	-3.829257	2.027854
H	3.414091	-4.328964	2.841025
C	2.414462	-2.519556	2.218126
C	1.721828	-1.839331	1.169316
C	2.603295	-1.833686	3.438486
H	3.138451	-2.330853	4.239842
C	2.129974	-0.556781	3.589562
H	2.286390	0.003241	4.502770
C	1.415133	0.026846	2.535098
H	1.006438	1.019952	2.631406

Cu(II)DMEGqu (gas phase QE)

Cu	0.000000	0.000000	0.000000
N	-1.084103	1.395805	1.068397
N	-2.270193	1.355074	3.205859
N	-0.024514	1.401027	3.194758
N	-1.266403	0.559600	-1.479862
N	1.855012	-0.272487	-0.866950
N	2.632234	-0.841103	-3.115179
N	1.803219	1.210059	-2.722217
N	0.740596	-1.324324	1.342783
C	-1.149108	1.401310	2.424043
C	-3.584912	0.862138	2.767604
H	-3.521052	0.491086	1.738730
H	-4.338028	1.662693	2.812225
H	-3.893622	0.042517	3.434394
C	-1.898457	1.261602	4.642955
H	-2.160347	0.256529	5.012298
H	-2.444400	2.006147	5.237420
C	-0.368105	1.504799	4.631706
H	-0.104589	2.511696	4.994181
H	0.189154	0.762742	5.220240
C	1.320490	1.751718	2.733673
H	1.332593	1.760417	1.637655
H	2.040585	1.006018	3.101165
H	1.605444	2.746080	3.114943
C	-2.069658	2.007162	0.271031
C	-2.914217	3.054831	0.664040
H	-2.886485	3.411991	1.693320
C	-3.781176	3.678829	-0.266499
H	-4.414465	4.497654	0.076379
C	-3.838721	3.270224	-1.592126
H	-4.524710	3.740059	-2.297471
C	-2.995650	2.211904	-2.038424
C	-2.109070	1.587016	-1.101213
C	-2.995018	1.717505	-3.371729
H	-3.666900	2.164596	-4.106541
C	-2.149705	0.673991	-3.725596
H	-2.146270	0.267423	-4.736503
C	-1.282382	0.128774	-2.753518
H	-0.590650	-0.678206	-2.999701
C	2.109696	0.000436	-2.171477
C	2.605858	-2.310630	-3.040561
H	2.079667	-2.630089	-2.134433
H	3.626689	-2.719783	-3.023624
H	2.079744	-2.698966	-3.926147
C	1.532183	2.438980	-1.973067
H	1.370788	2.188118	-0.918343
H	0.630733	2.924176	-2.375250
H	2.384443	3.132520	-2.061940
C	2.273981	1.286159	-4.124489
H	3.150390	1.952785	-4.174785
H	1.488415	1.688655	-4.778973
C	2.638580	-0.183745	-4.449590
H	1.883611	-0.671000	-5.088259
H	3.620579	-0.283864	-4.930528
C	2.649644	-1.162364	-0.119521
C	3.985999	-1.494144	-0.382676
H	4.472153	-1.102855	-1.276071
C	4.723786	-2.308083	0.511697
H	5.763005	-2.537306	0.274163
C	4.152986	-2.815571	1.670859
H	4.719529	-3.460862	2.342696
C	2.800222	-2.497919	1.984681
C	2.054378	-1.666643	1.085791
C	2.129894	-2.978865	3.142837
H	2.667247	-3.623226	3.840961
C	0.805172	-2.631684	3.373370
H	0.267149	-3.002629	4.245211
C	0.144398	-1.784893	2.456427
H	-0.890062	-1.475792	2.613624

Cu(II)DMEGqu (gas phase ORCA)

Cu	0.000000	0.000000	0.000000
N	-1.138087	1.217345	1.045440
N	-2.258968	1.121748	3.171661
N	-0.072583	1.415753	3.130306
N	-1.213783	0.482165	-1.478106
N	1.712893	-0.383833	-0.887807
N	2.399505	-0.933121	-3.126829
N	1.853498	1.153035	-2.660810
N	0.644930	-1.306842	1.329651
C	-1.177876	1.262666	2.383111
C	-3.579478	0.677369	2.764405
H	-3.524352	0.245706	1.767680
H	-4.295154	1.502643	2.755065
H	-3.924280	-0.081762	3.468423
C	-1.906026	1.336187	4.582382
H	-2.354318	0.558819	5.200034
H	-2.273279	2.307722	4.921782
C	-0.370080	1.265392	4.557292
H	0.094407	2.071071	5.124510
H	0.015661	0.310193	4.926102
C	1.261579	1.680225	2.637560
H	1.198025	1.907010	1.574948
H	1.910015	0.813045	2.785342
H	1.684833	2.536569	3.165580
C	-2.122039	1.821341	0.257222
C	-2.993539	2.823790	0.643677
H	-2.972334	3.199162	1.658921
C	-3.902212	3.382922	-0.276374
H	-4.570294	4.163603	0.065482
C	-3.958739	2.959844	-1.581986
H	-4.674294	3.381795	-2.276064
C	-3.062146	1.962068	-2.025446
C	-2.135223	1.415300	-1.100948
C	-3.027544	1.459691	-3.343858
H	-3.728699	1.842073	-4.076584
C	-2.114060	0.489338	-3.688195
H	-2.083752	0.075767	-4.687498
C	-1.206462	0.031988	-2.724133
H	-0.462544	-0.717541	-2.964814
C	1.995383	-0.085750	-2.162563
C	2.429292	-2.382373	-3.053648
H	1.848143	-2.712389	-2.195675
H	3.450614	-2.757886	-2.956531
H	1.988527	-2.787366	-3.965975
C	1.503625	2.339561	-1.910728
H	1.557880	2.104482	-0.849428
H	0.492481	2.673042	-2.157334
H	2.209290	3.139842	-2.140277
C	2.058860	1.167397	-4.111893
H	2.705752	1.997352	-4.392823
H	1.100286	1.279698	-4.627782
C	2.711121	-0.201688	-4.363136
H	2.286804	-0.721509	-5.221140
H	3.793260	-0.128841	-4.497458
C	2.501835	-1.267659	-0.145992
C	3.809426	-1.633094	-0.410932
H	4.314698	-1.244007	-1.285861
C	4.505979	-2.496728	0.457507
H	5.527286	-2.761857	0.214006
C	3.920736	-3.005234	1.591386
H	4.457755	-3.683997	2.241531
C	2.597926	-2.629306	1.915684
C	1.906733	-1.743731	1.049374
C	1.902830	-3.085626	3.056103
H	2.390997	-3.774897	3.735313
C	0.615355	-2.660980	3.294448
H	0.057026	-3.014444	4.151140
C	0.020282	-1.752505	2.409639
H	-0.983657	-1.382079	2.576949

Cu(II)DMEGqu (solid relaxed QE)

Cu	0.000000	0.000000	0.000000
N	-1.240850	1.478274	0.639595
N	-2.994168	1.800687	2.318702
N	-0.950926	1.150768	2.957675
N	-0.997800	0.214532	-1.744157
N	1.742966	-0.305736	-0.930036
N	2.216688	-0.163849	-3.317579
N	1.455811	1.621993	-2.242896
N	0.884074	-1.082261	1.442206
C	-1.736875	1.525641	1.886956
C	-4.194139	2.190254	1.613297
H	-4.114454	1.983736	0.555543
H	-4.382033	3.264967	1.762462
H	-5.031739	1.616227	2.016852
C	-3.173771	1.444154	3.722429
H	-3.854357	0.582634	3.744019
H	-3.646224	2.261403	4.291061
C	-1.755730	1.096111	4.183716
H	-1.363935	1.821431	4.907731
H	-1.709283	0.090147	4.615821
C	0.477098	1.443067	3.079014
H	0.801337	1.995384	2.192030
H	1.083823	0.537491	3.195860
H	0.642249	2.058218	3.981438
C	-1.886867	2.037920	-0.473657
C	-2.577736	3.239261	-0.475876
H	-2.713276	3.766223	0.454813
C	-3.169785	3.744040	-1.645873
H	-3.744888	4.658813	-1.543004
C	-3.077665	3.083910	-2.858796
H	-3.552105	3.466742	-3.764275
C	-2.373087	1.854772	-2.912268
C	-1.749107	1.362216	-1.724068
C	-2.274103	1.047993	-4.069551
H	-2.812153	1.337330	-4.965150
C	-1.484379	-0.086886	-4.070251
H	-1.330396	-0.679580	-4.968931
C	-0.825268	-0.458101	-2.889767
H	-0.125188	-1.286754	-2.882530
C	1.885157	0.352601	-2.103030
C	2.519750	-1.568419	-3.543473
H	2.656727	-2.071480	-2.580629
H	3.441539	-1.650082	-4.138741
H	1.688278	-2.068382	-4.067092
C	1.134036	2.619180	-1.255614
H	0.986636	2.197480	-0.259227
H	0.217919	3.144604	-1.554327
H	1.956660	3.336191	-1.226273
C	1.208411	1.966699	-3.632267
H	1.704776	2.910301	-3.899197
H	0.124798	2.096412	-3.738383
C	1.745329	0.743551	-4.392161
H	0.932304	0.251526	-4.944629
H	2.549216	0.986725	-5.091899
C	2.643691	-1.037953	-0.193040
C	3.968616	-1.305112	-0.505966
H	4.362596	-1.028817	-1.476936
C	4.801134	-1.930534	0.442962
H	5.834923	-2.114817	0.160545
C	4.343852	-2.389821	1.663479
H	4.990669	-2.936432	2.347828
C	2.981104	-2.194696	1.994114
C	2.164475	-1.443135	1.098517
C	2.353796	-2.719817	3.144957
H	2.909918	-3.330307	3.840873
C	1.025213	-2.458776	3.390534
H	0.525623	-2.886729	4.248458
C	0.333982	-1.566965	2.564917
H	-0.648454	-1.185098	2.825591

Cu(II)DMEGqu (exp. crystal structure)

Cu	0.000000	0.000000	0.000000
N	1.634744	1.125240	-0.231345
N	1.113081	2.990208	-1.544094
N	1.963793	3.400618	0.441170
N	1.298981	-1.284388	0.766668
N	-1.182863	-1.243345	-0.987252
N	0.162751	-2.992141	-1.796960
N	-1.712196	-3.567219	-0.804328
N	-1.477759	1.267734	-0.392748
C	1.604303	2.449646	-0.441169
C	0.744956	2.283287	-2.749241
H	1.121763	2.730499	-3.510528
H	-0.211614	2.264597	-2.829943
H	1.080362	1.383956	-2.708890
C	1.103866	4.447638	-1.471463
H	0.197322	4.793571	-1.476843
H	1.598473	4.839796	-2.208539
C	1.781762	4.720162	-0.156023
H	2.636673	5.158667	-0.293216
H	1.226933	5.281452	0.408890
C	2.135723	3.184075	1.864212
H	1.706278	2.363445	2.117078
H	1.742463	3.912753	2.348423
H	3.071859	3.131025	2.068657
C	2.764122	0.534008	0.330878
C	4.040993	1.064774	0.403510
H	4.198837	1.925531	0.086082
C	5.105180	0.323012	0.952282
H	5.948421	0.711676	1.003393
C	4.931504	-0.947804	1.404212
H	5.651906	-1.423062	1.751230
C	3.647813	-1.541409	1.345031
C	2.579312	-0.782837	0.817779
C	3.346266	-2.828482	1.831932
H	4.025711	-3.370000	2.162809
C	2.064507	-3.285504	1.815791
H	1.859880	-4.125558	2.160119
C	1.056600	-2.481374	1.277779
H	0.182212	-2.798860	1.280469
C	-0.952544	-2.554946	-1.194386
C	1.168161	-2.169914	-2.429124
H	1.380847	-2.533524	-3.292634
H	1.957628	-2.153892	-1.885732
H	0.831832	-1.276355	-2.534036
C	0.249500	-4.452741	-1.735089
H	0.942344	-4.735772	-1.116375
H	0.428910	-4.831580	-2.609358
C	-1.138733	-4.858536	-1.232047
H	-1.666196	-5.260608	-1.939533
H	-1.077518	-5.480018	-0.489591
C	-2.860631	-3.483452	0.075322
H	-3.662667	-3.629772	-0.430409
H	-2.890987	-2.612198	0.478831
H	-2.786918	-4.150147	0.761288
C	-2.384311	-0.675859	-1.398831
C	-3.403991	-1.275258	-2.109007
H	-3.354201	-2.181125	-2.313452
C	-4.518923	-0.525673	-2.528656
H	-5.192174	-0.952734	-3.007487
C	-4.640369	0.798973	-2.262340
H	-5.386945	1.269652	-2.558247
C	-3.623055	1.456119	-1.530644
C	-2.500032	0.706705	-1.105614
C	-3.654290	2.823025	-1.183626
H	-4.360505	3.360135	-1.458012
C	-2.634499	3.352997	-0.433099
H	-2.653558	4.249067	-0.185614
C	-1.569686	2.541601	-0.045731
H	-0.895745	2.910485	0.476141

Cu(II)DMEGqu (tetrahedral)

Cu	0.000000	0.000000	0.000000
N	-1.205827	1.365331	0.711405
N	-2.124426	1.926095	2.868381
N	0.029373	2.312671	2.474749
N	-1.576441	-0.813865	-0.844572
N	1.741765	0.044286	-0.887610
N	2.518418	-0.482298	-3.103940
N	1.458203	1.435082	-2.772823
N	0.924327	-1.319717	1.303030
C	-1.132248	1.845740	1.954187
C	-3.315483	1.081716	2.898486
H	-3.206680	0.245752	2.210717
H	-4.209827	1.646699	2.631845
H	-3.429478	0.695289	3.912556
C	-1.606562	2.457992	4.139295
H	-1.532975	1.641021	4.863809
H	-2.267869	3.224663	4.541703
C	-0.232144	2.999962	3.745928
H	-0.253431	4.082159	3.579629
H	0.541832	2.772643	4.478132
C	1.167758	2.727431	1.673652
H	1.377285	1.981670	0.908228
H	2.034991	2.802367	2.328689
H	0.993754	3.699187	1.198858
C	-2.440505	1.239264	0.035752
C	-3.446113	2.187630	0.043108
H	-3.323357	3.093050	0.625395
C	-4.632681	1.990328	-0.690178
H	-5.398766	2.755250	-0.656118
C	-4.833300	0.853301	-1.435090
H	-5.755473	0.700092	-1.981857
C	-3.817533	-0.127678	-1.497235
C	-2.611162	0.084089	-0.778454
C	-3.926525	-1.327735	-2.237036
H	-4.838030	-1.529196	-2.788317
C	-2.886806	-2.226601	-2.253326
H	-2.953093	-3.155761	-2.803803
C	-1.708470	-1.922987	-1.553125
H	-0.857390	-2.593919	-1.570039
C	1.926215	0.316440	-2.197001
C	2.755742	-1.913574	-2.957870
H	2.330809	-2.269226	-2.022727
H	3.824472	-2.132612	-2.970646
H	2.276384	-2.430894	-3.791720
C	0.992431	2.618525	-2.069185
H	0.473490	2.321474	-1.159995
H	0.292674	3.145994	-2.716760
H	1.823715	3.285812	-1.822056
C	1.913662	1.524344	-4.166608
H	2.724822	2.254833	-4.238633
H	1.099462	1.839113	-4.818654
C	2.394275	0.096550	-4.452366
H	1.660599	-0.481411	-5.021956
H	3.348744	0.065109	-4.976762
C	2.709138	-0.645180	-0.151959
C	4.071440	-0.630982	-0.426887
H	4.437408	-0.076444	-1.282562
C	4.986000	-1.312030	0.392214
H	6.039853	-1.272788	0.146149
C	4.562262	-2.022110	1.492001
H	5.269055	-2.558807	2.113085
C	3.186159	-2.049896	1.823363
C	2.257615	-1.345447	1.013632
C	2.672418	-2.757371	2.932408
H	3.350796	-3.316332	3.566959
C	1.321909	-2.733438	3.195563
H	0.902852	-3.271921	4.035460
C	0.480569	-1.987255	2.358732
H	-0.585441	-1.931472	2.550243

Cu(II)DMEGqu (square planar)

Cu	0.000000	0.000000	0.000000
N	1.599121	1.143377	-0.309794
N	2.264941	2.975125	-1.707444
N	1.107238	3.416466	0.117597
N	1.332781	-1.173049	0.923424
N	-1.621287	-1.125300	0.295201
N	-1.152439	-3.406280	-0.108180
N	-2.286546	-2.934831	1.724203
N	-1.340176	1.179557	-0.928549
C	1.670084	2.451128	-0.621364
C	2.781214	2.230545	-2.842976
H	3.861394	2.359977	-2.938426
H	2.303026	2.587451	-3.757782
H	2.556706	1.175667	-2.700686
C	2.214490	4.444046	-1.678440
H	1.876766	4.825485	-2.642091
H	3.206471	4.852081	-1.470944
C	1.212305	4.722875	-0.542091
H	1.576857	5.469894	0.162175
H	0.231946	5.040137	-0.909465
C	0.426046	3.236395	1.384499
H	0.627730	2.229942	1.746294
H	-0.651787	3.377475	1.267115
H	0.803923	3.961498	2.106882
C	2.784395	0.429755	-0.073096
C	4.080498	0.860805	-0.302283
H	4.264348	1.837407	-0.727752
C	5.187937	0.059373	0.038362
H	6.181273	0.431228	-0.180546
C	5.032464	-1.155792	0.655648
H	5.887550	-1.758551	0.933845
C	3.731082	-1.599531	0.980200
C	2.611199	-0.815224	0.589191
C	3.476351	-2.757597	1.744081
H	4.306029	-3.382320	2.054504
C	2.190264	-3.052471	2.131210
H	1.974189	-3.899949	2.768402
C	1.143118	-2.226745	1.704980
H	0.129954	-2.419008	2.025616
C	-1.699750	-2.427899	0.625451
C	-0.487079	-3.245749	-1.386215
H	-0.881056	-3.975002	-2.095723
H	0.590982	-3.395453	-1.282036
H	-0.684818	-2.241248	-1.755392
C	-1.262989	-4.704650	0.566088
H	-0.281899	-5.028543	0.925713
H	-1.642897	-5.455067	-0.126372
C	-2.249611	-4.404376	1.710718
H	-3.247478	-4.805776	1.519106
H	-1.904239	-4.778393	2.674584
C	-2.784381	-2.173656	2.856854
H	-3.864922	-2.290657	2.963722
H	-2.550379	-1.122632	2.702110
H	-2.301187	-2.526461	3.770609
C	-2.801655	-0.400305	0.078323
C	-4.099921	-0.816151	0.322455
H	-4.291331	-1.790267	0.750426
C	-5.200625	-0.001449	-0.009298
H	-6.196277	-0.360482	0.220286
C	-5.036876	1.209762	-0.632512
H	-5.887657	1.821222	-0.904859
C	-3.733469	1.637232	-0.971013
C	-2.620307	0.841344	-0.585343
C	-3.469977	2.787526	-1.743541
H	-4.293541	3.421622	-2.051224
C	-2.183111	3.061412	-2.143675
H	-1.960879	3.900765	-2.789499
C	-1.143446	2.224676	-1.719929
H	-0.130778	2.400963	-2.051256

2.2 Impact of Finite-Temperature and Condensed-Phase Effects

Participations in this Publication
M. Krack, U. Gerstmann & W. G. Schmidt — Scientific input and support with manuscript preparation
P. Müller & M. Bauer — HERFD-XANES measurements
P. Müller, K. Karhan & T. D. Kühne — CP2K calculations

Reprinted with permission from **Impact of Finite-Temperature and Condensed-Phase Effects on Theoretical X-Ray Absorption Spectra of Transition Metal Complexes**
Patrick Müller, Kristof Karhan, Matthias Krack, Uwe Gerstmann, Wolf Gero Schmidt, Matthias Bauer and Thomas D. Kühne *Journal of Computational Chemistry* **2019** 40, 712-716, DOI:10.1002/jcc.25641.

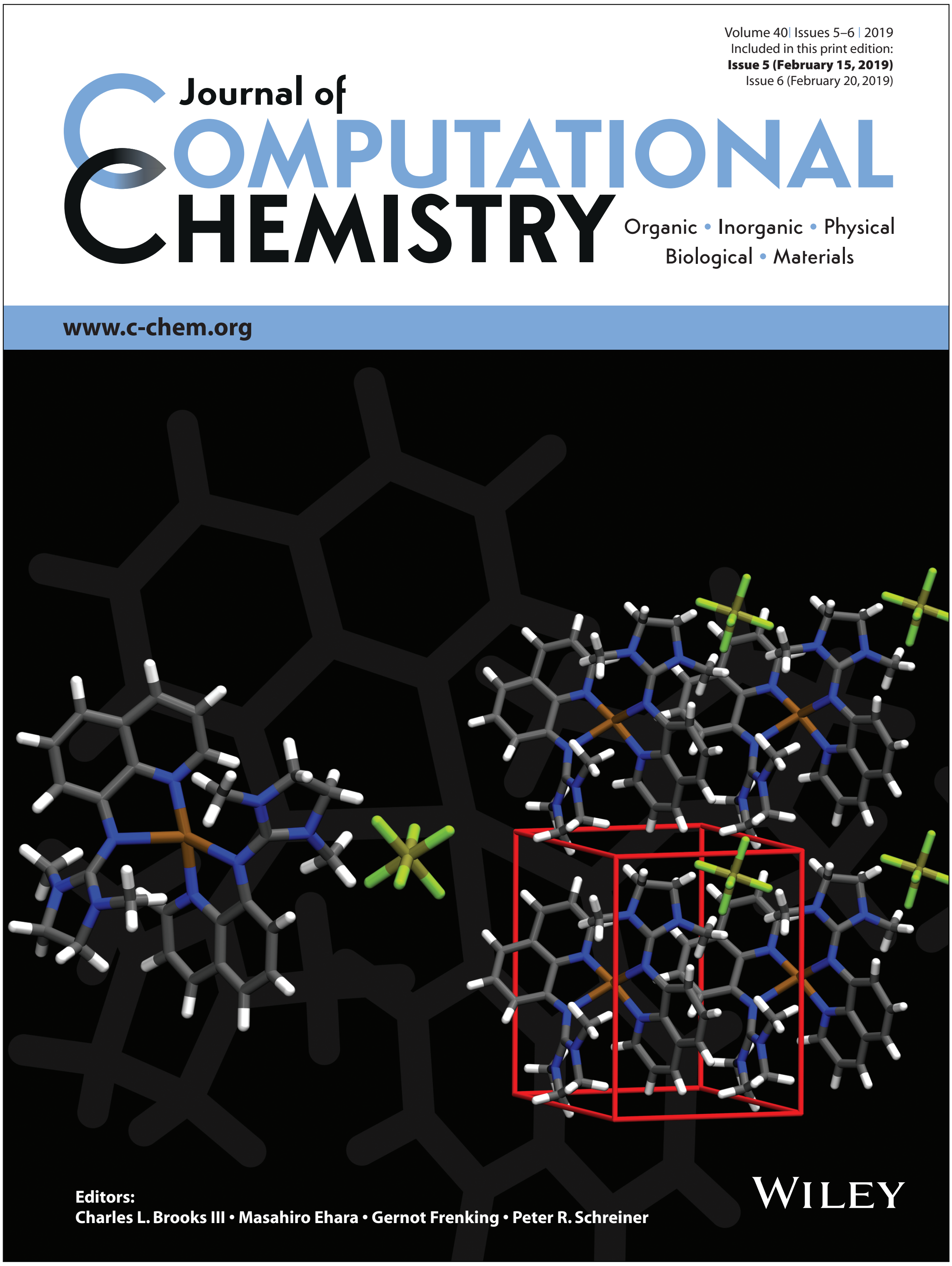

Volume 40| Issues 5–6 | 2019
Included in this print edition:
Issue 5 (February 15, 2019)
Issue 6 (February 20, 2019)

Journal of COMPUTATIONAL CHEMISTRY

Organic • Inorganic • Physical
Biological • Materials

www.c-chem.org

Editors:
Charles L. Brooks III • Masahiro Ehara • Gernot Frenking • Peter R. Schreiner

WILEY

FULL PAPER WWW.C-CHEM.ORG Journal of COMPUTATIONAL CHEMISTRY

Impact of Finite-Temperature and Condensed-Phase Effects on Theoretical X-Ray Absorption Spectra of Transition Metal Complexes

Patrick Müller,[a] Kristof Karhan,[a] Matthias Krack,[b] Uwe Gerstmann,[c] Wolf Gero Schmidt,[c] Matthias Bauer,[d] and Thomas D. Kühne *[d]

The impact of condensed-phase and finite-temperature effects on the theoretical X-ray absorption spectra of transition metal complexes is assessed. The former are included in terms of the all-electron Gaussian and augmented plane-wave approach, whereas the latter are taken into account by extensive ensemble averaging along second-generation Car–Parrinello ab initio molecular dynamics trajectories. We find that employing the periodic boundary conditions and including finite-temperature effects systematically improves the agreement between our simulated X-ray absorption spectra and experimental measurements. © 2018 Wiley Periodicals, Inc.

DOI:10.1002/jcc.25641

Introduction

X-ray absorption spectroscopy (XAS) at transition metal K-edges has proven to be a powerful tool to investigate the working principle of transition metal centers in catalysts, functional materials, and enzymes over the last decades.[1–6] The method's success is because of the fact that it provides both information on the electronic details and local structure of the functional metal center, being fully independent of the state of aggregation.[7] In a typical XAS experiment, the attenuation of an incoming X-ray beam by absorption through a sample is measured as a function of energy. The corresponding X-ray absorption spectrum is obtained by applying Lambert–Beers law. It is characterized by a sharp edge-step caused by a resonant excitation of a 1*s* electron in case of so-called K-edge spectra, which are the subject of this work. Although no sharp separation exists, the interval from around 15 eV before the edge till 40 eV thereafter is called the X-ray absorption near edge structure (XANES) region including pre-edge signals, while the region starting from 40 eV above the edge is defined as the extended X-ray absorption fine structure (EXAFS) region, which is indicated in Figure 1.

Typically, in the XANES part, the so-called prepeak, caused by 1*s* → *nd* transitions, is used to obtain information about the lowest unoccupied molecular orbital (LUMO) states by application of density functional theory (DFT) methods.[8–10] The absorption edge itself and the following intense first oscillations are mostly treated in a comparative way using highly defined references to extract oxidation states and a rough estimation of the local structure.[11] The latter one is then achieved by analysis of the oscillations in the EXAFS part, including type, number, and distances of coordinating ligand atoms.[7,12,13]

Although this three step analysis approach is highly valuable and frequently used, it neglects the superior potential of the XANES region, as it carries basically the full information about the geometric (backscattering) and electronic (orbital contributions) situation. This advantage becomes even larger if the much better signal to noise ratio of XANES spectra compared to EXAFS spectra is taken into account.

Making full use of the information content in K-edge XANES data is limited by the lifetime broadening of the 1*s* electron hole after K-edge excitation.[14] This broadening limits the extraction of information from the pre-edge peak and XANES region significantly, as details of the spectroscopic signatures are smeared out.[14–16] Consequently, the value of comparing such lifetime broadened spectra to highly precise theoretical calculations is limited.

To make use of XANES spectra to the largest possible extent, two main conditions have to be met:

---

[a] *P. Müller, K. Karhan*
Department of Chemistry, University of Paderborn, Warburger Str. 100, 33098, Paderborn, Germany
[b] *M. Krack*
Laboratory for Scientific Computing and Modelling, Paul Scherrer Institut, CH-5232, Villigen PSI, Switzerland
[c] *U. Gerstmann, W. Gero Schmidt*
Department of Physics, University of Paderborn, Warburger Str. 100, 33098, Paderborn, Germany
[d] *M. Bauer, T. D. Kühne*
Department of Chemistry and Center for Sustainable Systems Design, University of Paderborn, Warburger Str. 100, 33098, Paderborn, Germany
E-mail: tdkuehne@mail.upb.de

This project has received funding from the European Research Council (ERC) under the European Union's Horizon 2020 research and innovation programme (grant agreement no. 716142). M.B., P.M., W.G.S., and U.G. received funding from the Forschergruppe 1405 of the German Research Council. M.B. received funding from the German Ministry for Science and Education in frame of project SusChEmX (FKZ 05K14PP1).

Contract Grant sponsor: Bundesministerium für Bildung und Forschung; Contract Grant number: SusChEmX (FKZ 05K14PP1); Contract Grant sponsor: H2020 European Research Council; Contract Grant number: grant agreement No 716142; Contract Grant sponsor: German Ministry for Science and Education; Contract Grant number: FKZ 05K14PP1; Contract Grant sponsor: German Research Council; Contract Grant sponsor: European Research Council (ERC); Contract Grant number: 716142

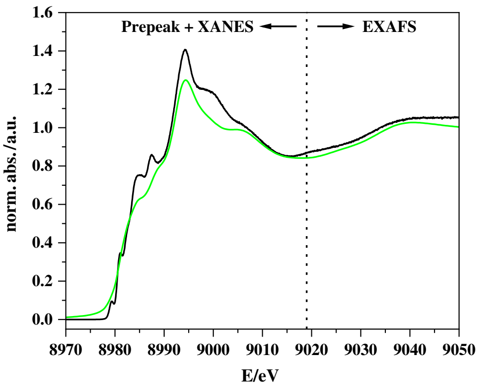

Figure 1. Comparison of the conventional (green) and high energy resolution XANES spectra (black) of [Cu(I)(DMEGqu)$_2$](PF$_6$). The effect of the high resolution detection mode is particularly visible in the XANES region. [Color figure can be viewed at wileyonlinelibrary.com]

1. The lifetime broadening of K-edge XANES data needs to be reduced.
2. An accurate theoretical description of the prepeak and XANES feature has to be achieved over the full XANES energy range.

With the advent of high resolution partial fluorescence yield detection using Johann-type spectrometers,[17] high energy resolution fluorescence detected XANES (HERFD-XANES) spectra can be obtained.[14] HERFD-XANES spectra are recorded by monitoring the intensity of a narrow emission line range in such a way that the lifetime broadening of K-edge spectra is nearly eliminated. However, it still has to be taken into account that an experimental broadening from the beamline and spectrometer is present.[15] Overall, a reduction from around 5–1.5 eV in first row transition metal K-edges can be achieved, and condition 1 is met. The effect of high resolution fluorescence detection is demonstrated in Figure 1 for the example of the biomimetic Cu(I) complex formed by the quinoline-based ligand N-(1,3-dimethyl-imidazolidin-2-ylidene)quinolin-8-amine (DMEGqu), that is, [Cu(I)(DMEGqu)$_2$](PF$_6$), by comparing the conventional with high resolution spectra.[18,19]

As the geometric and electronic structure plays a central role for the electron transfer efficiency of such copper complexes, their investigation using XAS and theoretical techniques can therefore significantly contribute to the understanding of copper mediated electron transfer processes in general. However, with condition 2, several issues are connected. The application of pseudopotential methods to treat core-hole excitations is not straightforward. On the other hand, all-electron calculations are particularly more suited for describing X-ray absorption, but come with the disadvantage of larger computational costs.[20]

Although Kohn–Sham (KS) DFT is commonly used to describe complex structures, especially the description of excited states is more precisely treated by for example the so-called GW approximation for the electronic self-energies and the Bethe–Salpeter approach to describe Coulomb coupled electron–hole pairs.[21,22] Time-dependent DFT (TD-DFT) is currently the method of choice to address charge neutral excitations and to determine core excitations,[23–26] but on the price of the unknown TD exchange and correlation (XC) potential. Most numerical implementations rely on the adiabatic approximation, which often proves successful for finite systems such as molecules, but fails for extended systems such as solids.

Also critical for the simulation of X-ray absorption spectra is the basis set used to expand the electronic wave function. On the one hand, localized basis functions are computationally efficient and thus allow for the modeling of core electrons as well as many-body effects. However, even though systematically improvable, they do not form a complete set and are not suitable for the description of excited delocalized high-energy states. Plane waves, on the other hand, form by construction an orthogonal basis set that can be trivially improved by varying the corresponding cutoff energy. Moreover, plane waves are ideally suited to describe delocalized high-energy states as well as systems with periodic boundary conditions such as molecular crystals. Naturally, the description of core states with plane waves is cumbersome.

Although most of the developments for the simulation of XANES spectra focused on the improved description of the electronic structure of the material under investigation, temperature effects, the systems dynamics, and environmental or matrix factors are rarely in the center of interest. Hence, in this work, we assess the impact of finite-temperature and condensed-phase effects on theoretical X-ray absorption spectra of complex systems in the gas and liquid phase, as well as in water solution.

The remaining of this article is organized as follows. “Methodology and computational details” section describes the employed methods to compute X-ray absorption spectra (XAS) within the all-electron Gaussian and augmented plane-wave (GAPW) approach, as well as the computational details. Further explanation and interpretation of results are discussed in “Results and discussion” section followed by “Conclusions” section.

Methodology and Computational Details

In particular, we are comparing the computed XAS spectra of the aforementioned Cu(I) complex in the gas (69 atoms) and in the crystalline phase (76 atoms), with that of a single complex in water solution (432 atoms), all at 0 K and 300 K. All calculations were conducted at the DFT level using the CP2K suite of programs,[27] where the exact XC functional is substituted by the Becke–Lee–Yang–Parr generalized gradient approximation.[28,29] The atomic configurations were obtained using the mixed Gaussian and plane-wave approach in conjunction with separable and norm-conserving pseudopotentials to describe the interactions between the valence electrons and the ionic cores.[30–32] In this approach, the KS orbitals are expanded in Gaussians, while for the electron density a plane-wave basis is employed. The former are represented by an accurate molecularly optimized double-ζ basis set with one set of polarization functions (DZVP),[33] while a density cutoff of 360 Ry is used for the charge density. For the purpose to compute the static XAS spectra, the nuclear ground-state at 0 K is located by minimizing the total energy with the limited-memory Broyden–Fletcher–Goldfarb–Shanno algorithm.[34] To mimic an extended condensed-phase system, 3D periodic boundary condition were employed, while, in the gas phase, the Poisson problem is tackled using an efficient wavelet-based solver and a vacuum portion of 6 Å along all three nonperiodic directions.[35] In order to assess the impact of finite-temperature effects, DFT-based ab initio molecular dynamics (AIMD) simulations were performed using the second generation Car–Parrinello approach of Kühne et al.[36–39] For each system we are considering here, the modified Langevin equation is integrated for 25 ps to equilibrate the system followed by additional 100 ps in order to accumulate statistics, all using a discretized time-step of 0.5 fs. Out of these trajectories, the eventual finite-temperature XAS spectra are each computed as ensemble averages over 50 statistical independent configurations that are separated by 2 ps.

The XAS spectra were simulated at the copper K-edge using the full-core-hole (FCH) transition potential formalism,[40–42] as implemented in the all-electron GAPW approach.[43–45] As before, the GAPW method consists of a dual basis set made up of localized Gaussian type orbitals to describe the KS orbitals, as well as plane waves to represent only the smoothly varying density between the atoms.[46,47] For the latter, a density cutoff of 480 Ry is employed, whereas the all-electron orbitals are described by consistent DZVP Gaussian basis set for solid-state calculations of Bredow and coworkers.[48]

Because of the fact that the energy functional depends parametrically on the occupation number of the KS orbitals,[49] the transition energies can be determined by computing the total energy differences between the ground and an excited state that is obtained by promoting an electron into a virtual orbital. Both, the initial and final states can be directly approximated by selected orbitals that are solutions of the KS equations with a modified core-hole potential on the absorbing atom. Because we assume that the location of the promoted electron is immediately delocalized in the conduction band, its contribution to the final spectrum is essentially independent of the final state, which allows computing the whole spectrum with just one electronic structure calculation. In the single electron picture, the transition probabilities simplifies to dipole transition elements between the initial and final orbitals. Thus, $I \propto |\langle \psi'_f | \mathbf{E}\mu | \psi'_{\text{core}} \rangle|^2$, where **E** is the electric field representing the incoming photon and μ is the dipole operator. Yet, in the case of soft X-rays, where the wavelength of the interacting photon is much larger than the molecular dimension, it suffices to consider just the first term in the expansion of the electric field. In this so-called electric dipole approximation, the transition probabilities are proportional to the orbital-dipole integral along the polarization direction l, that is, $|\langle \psi'_f | \mathbf{r}_l | \psi'_{\text{core}} \rangle|^2$. For the purpose to uniquely associate the core orbitals to the atomic centers, the canonical orbitals are substituted by maximally localized Wannier functions as obtained the scheme of Berghold et al.[50] The localized core orbital ψ^A_{core} are characterized by maximizing the overlap between ψ^A_{core} and the functions of a minimal Slater-type basis set STO^A_α with respect to α, which denotes the energy level and angular momentum. By changing the occupation number of the excited core-hole orbital, the selected core-hole potential is applied that is followed by a variational optimization of the modified KS equations within the local spin density approximation to accommodate for the spin polarization because of removing an electron from the core. While, as already alluded to above, the dynamic XAS spectra at finite-temperature are computed as an ensemble average, in the static case, the eventual discrete spectral distribution, which is determined in terms of transition moment integrals in the velocity form, are convoluted by Gaussian functions to mimic the experimental broadening. Specifically, for all static spectra a constant Gaussian width of 0.5 eV is used below the edge, followed by a linearly increasing width up to 8 eV over the following 20 eV.[51]

HERFD-XANES experiments were performed at beamline ID26 of the European Synchrotron Radiation Facility (ESRF) in Grenoble (France). For the measurements at the copper K-edge (8979 eV), a Si(311) double-crystal monochromator was used. The maximum beam current was 200 mA with a ring-energy of 6 GeV. For the K-edge measurements, the solid samples were prepared as wafers using degassed cellulose as a binder to avoid self-absorption effects. The spectra were recorded at 30 K in a closed cycle helium cryostat. The Cu(I) samples were additionally prepared under inert atmosphere in a glove box and spectrometer was kept under helium atmosphere to reduce the absorption of the fluorescence radiation. No signs of radiation damage could be detected in any sample within the acquisition time and measurements were carried out on multiple spots.

Results and Discussion

Blue copper or type-one proteins span a large window of reduction potentials that leads to a variety of possible electron transfer partners.[1,2] However, subject to the present investigation are so-called type-zero biomimetic copper complexes, which exhibit electron transfer features similar to blue copper proteins, but with hard nitrogen instead of sulfur donor ligands.[52] The electron transfer properties of such complexes depend crucially on the structural details at the Cu(I) center,[53–55] which are closely correlated to the electronic properties of the compounds. As a prototype model for type-zero complexes, we use the aforementioned Cu(I) complex formed by the quinoline-based ligand DMEGqu, that is, $[\text{Cu(I)}(\text{DMEGqu})_2](\text{PF}_6)$.[18,19] Yet, in order to understand the working principle of biomimetic complexes, it is of course mandatory to access their electronic and structural details in situ, which is a highly demanding task that is perfectly matched by XANES spectroscopy. However, the sensitivity of XANES toward temperature effects, cluster sizes, and solvent influences is rarely addressed.

In general, the spectrum can roughly be divided into two sections. The first one being transitions into discrete orbitals with and without charge transfer character in the region up to 8985 eV and transitions into the continuum after that. As can be seen in Figure 2, the computed spectrum of using a single Cu(I) complex in the gas phase, whose structure has been

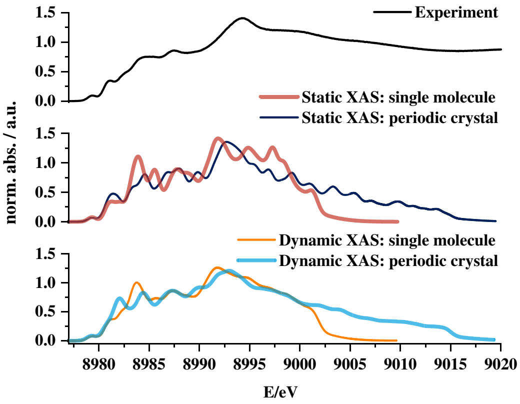

Figure 2. Experimental and simulated XAS spectra of the Cu(I) complex as obtained by static (0 K) and dynamic (300 K) calculations in the gas (single molecule), as well as condensed-phase (periodic crystal). [Color figure can be viewed at wileyonlinelibrary.com]

optimized to yield the nuclear ground-state at 0 K, already qualitatively reproduces most experimental features up to 9000 eV. In particular, the energetic position of the transitions is described reasonably well; although, the intensity differs for some of them. For example, the peak at 8984 eV is quite strongly overestimated in its intensity. Furthermore, within the simulated spectra, most of the features are too narrow. Nevertheless, this can be corrected increasing the artificial broadening of the calculated transitions. However, computing the same XAS spectrum at finite-temperature exhibits several differences. In spite of the fact that because of the ensemble averaging, no artificial broadening is necessary, the spectra are throughout much smoother and generally in better agreement with the experimental reference. Still, the intensity of the peak at 8984 eV is overestimated and the white line at 8994 eV is shifted to a lower energy of 8992 eV in the calculation. This is to say that although the intensity of the spectrum is not quantitatively reproduced, the general shape and oscillations as obtained by the combined AIMD-XAS approach are in qualitative good agreement with experiment.

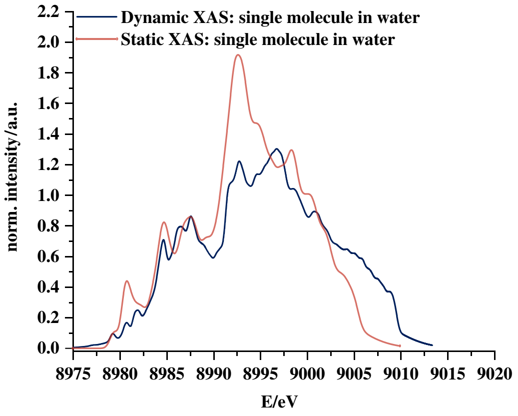

Figure 3. Simulated XAS spectra of a single Cu(I) complex in water solution, as obtained by dynamic (300 K) and static (0 K) condensed-phase calculations using periodic boundary conditions. [Color figure can be viewed at wileyonlinelibrary.com]

Yet, because the experimental spectra are obtained from solid state measurements, additional condensed-phase XAS calculations of the crystal structure using periodic boundary conditions were conducted. Already the static condensed-phase calculation represents a systematic improvement compared with the single molecule calculations. The energetic position and the intensity of the peaks are very well reproduced and the spectral shape is in very good agreement up to the white line. At higher energies, however, the oscillations are too narrow compared to the experimental measurement. Nevertheless, including finite-temperature effects, the latter part of spectrum is again significantly improved and reproduces the experimental curve rather well, but lacks the very good agreement for the second transition at 8982 eV, which is strongly overestimated. Comparing the dynamic finite-temperature simulations with their static counterparts at 0 K, it is apparent that, although the combined AIMD-XAS approach entails a systematically increased agreement with experiment in the high energy part of the spectrum, the improvement is relatively small in particular when considering the much larger computational effort of the AIMD simulations. On that occasion, we find it important to make a note that the investigated Cu(I) complex is rather stiff with a very hydrophobic ligand. This immediately suggests that the XAS response because of conformational fluctuations, which is the chief advantage of the present AIMD-XAS method to take those explicitly into account, is much higher when using other hydrophilic ligands.

In addition, to investigate the effect of solvation on the XAS spectrum, calculations of a single molecule in water solution were conducted for comparison. As can be seen in Figure 3, the most obvious difference in the XAS spectrum between the static and dynamic calculations in water solution is the intensity ratio between the white line and the other transitions. Another distinct difference is the shoulder at 8982 eV, which is absent in the simulated finite-temperature water solution spectrum. Because the underlying transition has some charge transfer character,[19] it might be shifted to higher or lower energies or just be dampened in intensity. Therefore, it might not be visible anymore. Even though the simulated XAS spectra cannot be directly compared to the present experiment because of the difference of solvent, it nevertheless demonstrates the feasibility of this approach to compute XAS spectra of complex molecules in aqueous solution, which is critical for further studies, for example, photocatalytic water splitting. Further mixed computational and experimental studies on complexes in aqueous solution have to be carried out in the future to shed light on these effects, which could either be of electronic or geometric nature.

Conclusions

In conclusion, we have assessed the impact of finite-temperature and condensed-phase effects on theoretical X-ray absorption spectra of transition metal complexes. We found that the usage of periodic boundary conditions entails a systematic improvement of the simulated XAS spectrum within the EXAFS range, though quantitative agreement with experiment cannot be achieved using a simple single electron approach. Nevertheless, further quantitative improvements can be achieved by the inclusion of finite-temperature effects using the present combined AIMD-XAS scheme.

Acknowledgments

Sonja Herres-Pawlis (RWTH Aachen) is kindly acknowledged for provision of samples and beamline ID26 at the ESRF (Grenoble) for provision of beamtime. The authors would like to thank the Gauss Center for Supercomputing (GCS) for providing computing time through the John von Neumann Institute for Computing (NIC) on the GCS share of the supercomputer JUWELS at the Jülich Supercomputing Centre (JSC) and on the GCS Supercomputer SuperMUC at Leibniz Supercomputing Centre (www.lrz.de). The generous allocation of supercomputing time on OCuLUS at the Paderborn Center for Parallel Computing (PC^2) (https://pc2.uni-paderborn.de/hpc-services/available-systems/oculus/) is knidly acknowledged.

Keywords: ab initio molecular dynamics · Car–Parrinello molecular dynamics · X-ray absorption spectroscopy · X-ray absorption near edge structure · near edge X-ray absorption fine structure

How to cite this article: P. Müller, K. Karhan, M. Krack, U. Gerstmann, W. G. Schmidt, M. Bauer, T. D. Kühne. *J. Comput. Chem.* **2019**, *40*, 712–716. DOI: 10.1002/jcc.25641

[1] L. E. Aleandri, B. Bogdanović, C. Dürr, S. C. Huckett, D. J. Jones, U. Kolb, M. Lagarden, J. Rozière, U. Wilczok, *Chem. A Eur. J.* **1997**, *3*, 1710.
[2] H. Dau, P. Liebisch, M. Haumann, *Anal. Bioanal. Chem.* **2003**, *376*, 562.
[3] M. Haumann, P. Liebisch, C. Müller, M. Barra, M. Grabolle, H. Dau, *Science* **2005**, *310*, 1019.
[4] A. S. K. Hashmi, C. Lothschütz, M. Ackermann, R. Doepp, S. Anantharaman, B. Marchetti, H. Bertagnolli, F. Rominger, *Chem. A Eur. J.* **2010**, *16*, 8012.
[5] P. Glatzel, T. -C. Weng, K. Kvashnina, J. Swarbrick, M. Sikora, E. Gallo, N. Smolentsev, R. A. Mori, *J. Electr. Spectrosc. Relat. Phenom.* **2013**, *188*, 17.
[6] R. Bjornsson, M. U. Delgado-Jaime, F. A. Lima, D. Sippel, J. Schlesier, T. Weyhermüller, O. Einsle, F. Neese, S. de Beer, *Z. Anorg. Allg. Chem.* **2015**, *641*, 65.
[7] M. Bauer, H. Bertagnolli, Methods in Physical Chemistry, Wiley-VCH Verlag GmbH & Co. KGaA, Weinheim, Germany, **2012**, p. 231.
[8] S. DeBeer George, T. Petrenko, F. Neese, *Inorg. Chim. Acta* **2008**, *361*, 965.
[9] P. Chandrasekaran, S. C. E. Stieber, T. J. Collins, L. Que, Jr., F. Neese, S. DeBeer, *Dalton Trans.* **2011**, *40*, 11070.
[10] V. Krewald, B. Lassalle-Kaiser, T. T. Boron, C. J. Pollock, J. Kern, M. A. Beckwith, V. K. Yachandra, V. L. Pecoraro, J. Yano, F. Neese, S. DeBeer, *Inorg. Chem.* **2013**, *52*, 12904.
[11] R. Schoch, W. Desens, T. Werner, M. Bauer, *Chem. A Eur. J.* **2013**, *19*, 15816.
[12] H. Bertagnolli, T. S. Ertel, *Angew. Chem. Int. Ed.* **1994**, *33*, 45.
[13] M. Bauer, C. Gastl, *Phys. Chem. Chem. Phys.* **2010**, *12*, 5575.
[14] P. Glatzel, U. Bergmann, *Coord. Chem. Rev.* **2005**, *249*, 65.
[15] M. Bauer, *Phys. Chem. Chem. Phys.* **2014**, *16*, 13827.
[16] A. J. Atkins, M. Bauer, C. R. Jacob, *Phys. Chem. Chem. Phys.* **2015**, *17*, 13937.
[17] H. H. Johann, *Z. Phys.* **1931**, *69*, 185.
[18] A. Hoffmann, J. Stanek, B. Dicke, L. Peters, B. Grimm-Lebsanft, A. Wetzel, A. Jesser, M. Bauer, M. Gnida, W. Meyer-Klaucke, M. Rübhausen, S. Herres-Pawlis, *Eur. J. Inorg. Chem.* **2016**, *2016*, 4731.
[19] N. J. Vollmers, P. Müller, A. Hoffmann, S. Herres-Pawlis, M. Rohrmüller, W. G. Schmidt, U. Gerstmann, M. Bauer, *Inorg. Chem.* **2016**, *55*, 11694.
[20] L. Triguero, L. G. M. Pettersson, H. Agren, *Phys. Rev. B* **1998**, *58*, 8097.
[21] E. L. Shirley, *Phys. Rev. Lett.* **1998**, *80*, 794.
[22] F. Bechstedt, Many-Body Approach to Electronic Excitations. Springer Series in Solid-State Sciences, Vol. *181*, Springer Berlin Heidelberg, Berlin, Heidelberg, Germany, **2015**.
[23] N. A. Besley, A. T. B. Gilbert, P. M. W. Gill, *J. Chem. Phys.* **2009**, *130*, 124308.
[24] S. DeBeer George, T. Petrenko, F. Neese, *J. Phys. Chem. A* **2008**, *112*, 12936.
[25] Y. Zhang, S. Mukamel, M. Khalil, N. Govind, *J. Chem. Theory Comput.* **2015**, *11*, 5804.
[26] I. P. E. Roper, N. A. Besley, *J. Chem. Phys.* **2016**, *144*, 114104.
[27] J. Vande Vondele, M. Krack, F. Mohamed, M. Parrinello, T. Chassaing, J. Hutter, *Comput. Phys. Commun.* **2005**, *167*, 103.
[28] A. D. Becke, *Phys. Rev. A* **1988**, *38*, 3098.
[29] C. T. Lee, W. T. Yang, R. G. Parr, *Phys. Rev. B* **1988**, *37*, 785.
[30] G. Lippert, J. Hutter, M. Parrinello, *Mol. Phys.* **1997**, *92*, 477.
[31] S. Goedecker, M. Teter, J. Hutter, *Phys. Rev. B* **1996**, *54*, 1703.
[32] M. Krack, *Theor. Chem. Acc.* **2005**, *114*, 145.
[33] J. Vande Vondele, J. Hutter, *J. Chem. Phys.* **2007**, *127*, 114105.
[34] J. Nocedal, *Math. Comput.* **1980**, *35*, 773.
[35] L. Genovese, T. Deutsch, A. Neelov, S. Goedecker, G. Beylkin, *J. Chem. Phys.* **2006**, *125*, 074105.
[36] T. D. Kühne, M. Krack, F. R. Mohamed, M. Parrinello, *Phys. Rev. Lett.* **2007**, *98*.
[37] T. D. Kühne, M. Krack, M. Parrinello, *J. Chem. Theory Comput.* **2009**, *5*, 235.
[38] T. D. Kühne, *WIREs Comput. Mol. Sci.* **2014**, *4*, 391.
[39] T. D. Kühne, E. Prodan, *Ann. Phys. Rehabil. Med.* **2018**, *391*, 120.
[40] B. Hetenyi, F. De Angelis, P. Giannozzi, R. Car, *J. Chem. Phys.* **2004**, *120*, 8632.
[41] M. Cavalleri, M. Odelius, D. Nordlund, A. Nilsson, L. G. M. Pettersson, *Phys. Chem. Chem. Phys.* **2005**, *7*, 2854.
[42] D. Prendergast, G. Galli, *Phys. Rev. Lett.* **2006**, *96*.
[43] M. Iannuzzi, T. Chassaing, T. Wallman, J. Hutter, *CHIMIA* **2005**, *59*, 499.
[44] M. Iannuzzi, J. Hutter, *Phys. Chem. Chem. Phys.* **2007**, *9*, 1599.
[45] M. Iannuzzi, *J. Chem. Phys.* **2008**, *128*, 204506.
[46] G. Lippert, J. Hutter, M. Parrinello, *Theor. Chem. Acc.* **1999**, *103*, 124.
[47] M. Krack, M. Parrinello, *Phys. Chem. Chem. Phys.* **2000**, *2*, 2105.
[48] M. F. Peintinger, D. Vilela Oliveira, T. Bredow, *J. Comput. Chem.* **2012**, *34*, 451.
[49] J. F. Janak, *Phys. Rev. B* **1978**, *18*, 7165.
[50] G. Berghold, C. J. Mundy, A. H. Romero, J. Hutter, M. Parrinello, *Phys. Rev. B* **2000**, *61*, 10,040.
[51] M. Cavalleri, M. Odelius, A. Nilsson, L. Pettersson, *J. Chem. Phys.* **2004**, *121*, 065.
[52] K. M. Lancaster, S. DeBeer George, K. Yokoyama, J. H. Richards, H. B. Gray, *Nat. Chem.* **2009**, *1*, 711.
[53] H. B. Gray, B. G. Malmström, R. J. P. Williams, *J. Biol. Inorg. Chem.* **2000**, *5*, 551.
[54] D. B. Rorabacher, *Chem. Rev.* **2004**, *104*, 651.
[55] P. Comba, M. Kerscher, *Coord. Chem. Rev.* **2009**, *253*, 564.

Received: 23 May 2018
Revised: 20 August 2018
Accepted: 18 September 2018

Chapter 3: Dinuclear Copper Complex as a potential Cu_A model

The study in this chapter revolves around three dinuclear copper complexes sharing a Cu_2S_2 core motif designed as biomimetic Cu_A model complexes. Electronic and geometric details are investigated by means of HERFD-XANES and VtC-XES in conjunction with (TD-)DFT calculations. With this combination of methods it is possible to elucidate changes in spin and oxidation state as well as charge transfer capabilites. Ligand sensitivity can also be achieved, especially with the VtC-XES technique. Last but not least, the possibility to follow the formation and fate of a mixed-valent state are demonstrated in an 'in-silico' experiment.

Participations in this Publication

A. Neuba & G. Henkel — Synthesis and provisioning of the samples

U. Flörke — X-Ray crystallography

Thomas D. Kühne — Scientific input and support with manuscript preparation

P. Müller & M. Bauer — HERFD-XANES and VtC-XES measurements, ORCA calculations and concomitant orbital analysis

Reprinted with permission from **Experimental and Theoretical High Energy Resolution Hard X-ray Absorption and Emission Spectroscopy on Biomimetic Cu_2S_2 Complexes**
Patrick Müller, Adam Neuba, Ulrich Flörke, Gerald Henkel, Thomas D. Kühne and Matthias Bauer, *The Journal of Physical Chemistry A*, **Just Accepted Manuscript**, DOI:10.1021/acs.jpca.9b00463. Copyright (2019) American Chemical Society.

Experimental and Theoretical High Energy Resolution Hard X-Ray Absorption and Emission Spectroscopy on Biomimetic Cu_2S_2 Complexes

Patrick Müller,[†] *Adam Neuba*[†]*, Ulrich Flörke,* [†] *Gerald Henkel,* [†] *Thomas D. Kühne,* [†#] *Matthias Bauer**[,†#]

[†]Universität Paderborn, Department Chemie, Warburger Straße 100, D-33098 Paderborn, Germany

[#]Center for sustainable systems design (CSSD), Warburger Straße 100, D-33098 Paderborn, Germany

ABSTRACT

High energy resolution fluorescence detected X-ray absorption near edge structure (HERFD-XANES) and Valence-to-Core X-ray emission (VtC-XES) spectroscopy are established as hard X-ray methods to investigate complexes that might be relevant as mimics for the biologically important Cu$_A$ site. By investigation of three carefully selected complexes of the type

$[Cu_2(NGuaS)_2X_2]$, characterized by a cyclic Cu_2S_2 core portion and a varying adjunct ligand nature, it is proven that the HERFD-XANES and VtC-XES measurements in combination with extensive TD-DFT calculations can reveal details of the electronic states in such complexes, including HOMO and LUMO levels and spin states. By theoretical spectroscopy, the value of this methodic combination for future in-situ studies is demonstrated.

INTRODUCTION

Cu_A – a prosthetic group based on a unique dinuclear copper motif - is a key prerequisite for the electron transfer within cytochrome c oxidases as well as nitrous oxide reductases.[1–7] Geometric and electronic structures of synthetic model complexes containing the Cu_2S_2 core portion of Cu_A are typically investigated by methods comprising X-ray crystallography,[1–3,8] electron paramagnetic resonance (EPR)[9,10] and optical absorption.[11,12].

Recently, modern X-ray spectroscopic methods offer great opportunities to study the geometric and electronic properties of enzymes and bio-inorganic mimics. Even in-situ measurements are readily possible due to an independence of the state of aggregation with these techniques.[13,14] In X-ray absorption spectra the pre-peak region is of special interest, but details of the electronic structure usually contained there are hidden because of the 1s core hole lifetime broadening encountered in conventional X-ray absorption spectroscopy (or XAS). The full potential of the XANES region can only be used by means of high energy resolution fluorescence detected XAS (HERFD-XAS). The smaller energy bandwidth and the concomitant sharpening of spectral features allows for a viable comparison with theoretically calculated spectra. Since transitions in this region directly reflect the 1s - 3d / LUMO states,[15] HERFD-XAS is suited for studying the electronic structure of a complex in a variety of different states.

Complementary to that, Valence to Core X-ray Emission spectroscopy (VtC-XES) is uniquely suited to probe the HOMO states of a given biomimetic complex.[16] As such, it enables to study the ligand structure around the central transition metal ion.[13] One of the biggest advantages compared to EXAFS spectroscopy is the possibility to distinguish between light atoms like carbon, nitrogen and oxygen. Both techniques applied together yield a detailed picture of the electronic structure and is even capable of revealing charge transfer transitions.[17]

Both techniques are yet unexplored regarding the investigation of electronic and geometric details of bio-relevant dinuclear Cu-S complexes. Considering the possibility of ultrafast measurements recently becoming available at X-ray free electron lasers, HERFD-XAS and VtC-XES will further gain importance in the future.[18] They very nicely complement transient XAS measurements,[19] thus allowing to record highly detailed molecular movies of photoinduced electron processes.

First explorative VtC-XES and HERFD-XAS analyses of the three homovalent sulfur bridged Cu-S complexes $[Cu^{II}_2(NGuaS)_2Cl_2]$ (**1**), $[Cu^{II}_2(NGuaS)_2Br_2]$ (**2**)[20] and $[Cu^{II}_2(NGuaS)_2(TC)_2]$ (**3**, TC = thiophenecarboxylate, NGuaS = 2-(1,1,3,3-tetramethylguanidino)benzenethiolate) will highlight the opportunity to study spin- and oxidation state as well as charge transfer transitions in such systems with hard X-rays.

Experimental Section

Materials

The complexes **1** and **2** were prepared following a procedure described earlier.[20] The synthesis of complex **3** follows the exact same scheme but since it was not reported before it is described in the following paragraph.

The reaction of (NGuaS-)$_2$ [20] (0.5 mmol, 222 mg) and Cu(I) thiophene-2-carboxylate [Sigma-Aldrich] (1.05 mmol, 200 mg) in 10 ml of abs. MeCN leads to a suspension of a blue solid. The reaction mixture was refluxed for 30 min. After cooling, ca. 70 ml of Et_2O was added. The blue precipitate was collected by filtration and washed with Et_2O. Yield: 0.57 g (70 %). Single crystals of **3** were obtained by slow diffusion of Et_2O into the mother liquor.

Measurements

HERFD-XANES and VtC-XES experiments were performed at beamline ID26 at the ESRF (European Synchrotron Radiation Facility) in Grenoble (France). A Johann-type X-ray emission spectrometer was used, where the crystal analyzers and photon detector (avalanche photodiode) were arranged in a vertical Rowland geometry with the sample. The measurements at the copper K-edge (8979 eV) were conducted using a Si(311) double-crystal monochromator. Ge(800) crystal analyzers were used to collect the emission spectra, while Si(444) crystals were used to select the k_α emission energy for the measurement of the HERFD-XANES. The ring energy was 6 GeV and the maximum beam current was 200 mA. A closed cycle helium cryostat was used to cool the samples to 30K. In order to avoid self-absorption effects, solid samples were prepared as wafers with degassed cellulose as binding material with a copper weight percentage of approx. 1 %. A constant helium atmosphere was used around the spectrometer parts reducing the absorption of fluorescence radiation. The measurements were carried out on multiple spots and no signs of radiation damage could be detected in any sample within the acquisition time. An incident energy of 9.1 keV was chosen for the VtC-XES measurements. The extraction procedure for the VtC-XES and the normalization of the HERFD-XANES spectra are briefly described in the Supporting Information.

DFT calculations

All DFT calculations were carried out with the ORCA program suite (version 3.0.3).[21,22] The functional of choice for all calculations was TPSSh following previous studies.[23] This is frequently considered the functional of choice for copper related systems and it was already shown that the broken-symmetry ground state of the chosen compounds can be described successfully.[24] The only exception are the VtC-XES spectra where the non-hybrid variant TPSS[23] was used. Geometry optimizations of single molecules were carried out using Ahlrich's def2-TZVP[25–27] basis set on all atoms for the three neutral species while ma-def2-SVP[26,28] was used in case of the reduced anionic species. To speed up the hybrid calculations, the RIJCOSX[29,30] approximation implemented in ORCA was used. The tight convergence criterion was imposed on all calculations and the Grimme dispersion correction with Becke-Johnson damping (D3BJ) has been utilized. [31,32] Copper K-edge transitions were calculated using the time-dependent DFT (TD-DFT) approach.[34] In these calculations the core properties were described by triple-ζ basis set CP(PPP)[33] for Cu and all-electron relativistically contracted (TZV-ZORA) basis sets on all other atoms.[35] Here, a special DFT grid of seven was chosen for the copper atom. VtC-XES spectra were calculated with a one electron approach using the same parameters.[36] Furthermore, the ZORA approach was used to account for relativistic effects.[37] For further analysis of the results, we used the program MOAnalyzer.[38] The calculated spectra have all been shifted to match the Cu K-edge (XANES) or

5

the main peak of the spectrum (VtC-XES): a shift of 1 eV was required for the XANES and 11-16 eV for the VtC spectra. In addition to the shift, all computed XANES spectra have been normalized to the experimental intensity of the prepeak and all VtC spectra to the intensity of the main peak. The discrete energy transitions were broadened using a Gaussian with a fwhm starting at 1 eV for the prepeak and linearly rising with increasing excitation energy (XANES) or with a fixed fwhm of 3.5 eV (XES).

Results and discussion

The gas phase geometry optimized complexes under investigation are shown in figure 1. All three complexes share the structural motif of two copper centers bridged by two sulfurs provided by a guanidine ligand. The Cu_2S_2 core portion shows a diamond like structure which is in line with previous studies.[20,24,39] The coordination of each copper atom is completed by a nitrogen donor function from one of the two guanidine ligands and a further ligand that varies

from chlorine (**1**) via bromine (**2**) to thiophenecarboxylate (**3**).

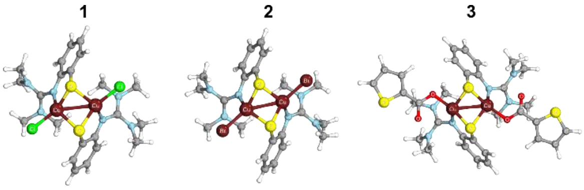

Figure 1: Structure models of the three complexes studied in this work.

To investigate the electronic structure of those three complexes we conducted HERFD-XANES and VtC-XES measurements as well as (TD)DFT calculations. We start the discussion with the experimental HERFD-XANES results. The spectra in figure 2 show a clearly separated prepeak located at 8977.9 eV, in agreement with an oxidation state of two for both copper centers, and several features in the edge. The spectral shape of the three compounds is expectedly very similar because their structures have strong resemblance to one another as only two of the ligands change while the $N_2Cu_2S_2$ core portion stays intact. The exact origin of this prepeak can only be evaluated by comparison with the results from calculations.

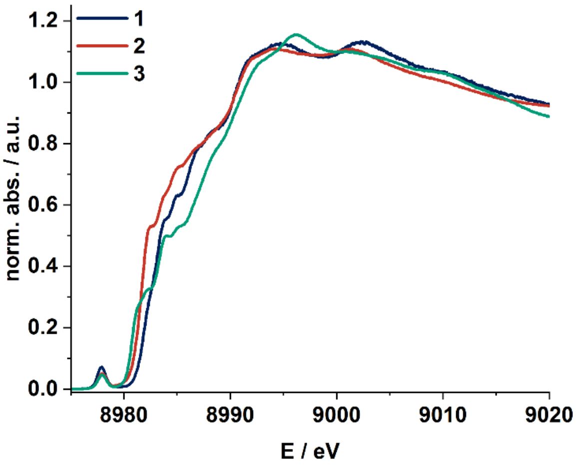

Figure 2: Comparison of the experimental HERFD-XANES spectra.

Because of the highly symmetric structure, every peak consists of two nearly degenerate transitions as deduced from the calculations. We therefore take only one of the copper centers into account for the following discussion of the results shown in figure 3.

The overall agreement for **1** (chloro derivative) is very good. Only the broken symmetry solution exhibits the correct energetic splitting between prepeak and edge while the singlet and triplet models are characterized by a too small or too large splitting between the spectral features prepeak and edge, respectively. Although for **2** and **3** the prepeak is as well reproduced in a very exact way, the splitting to the higher edge features is not reflected by any of the applied models (cf. figure 3). It has however to be mentioned, that a precise match between DFT level calculations and higher edge features of a significant continuum character cannot be routinely expected due to the intrinsic localized character of the method.

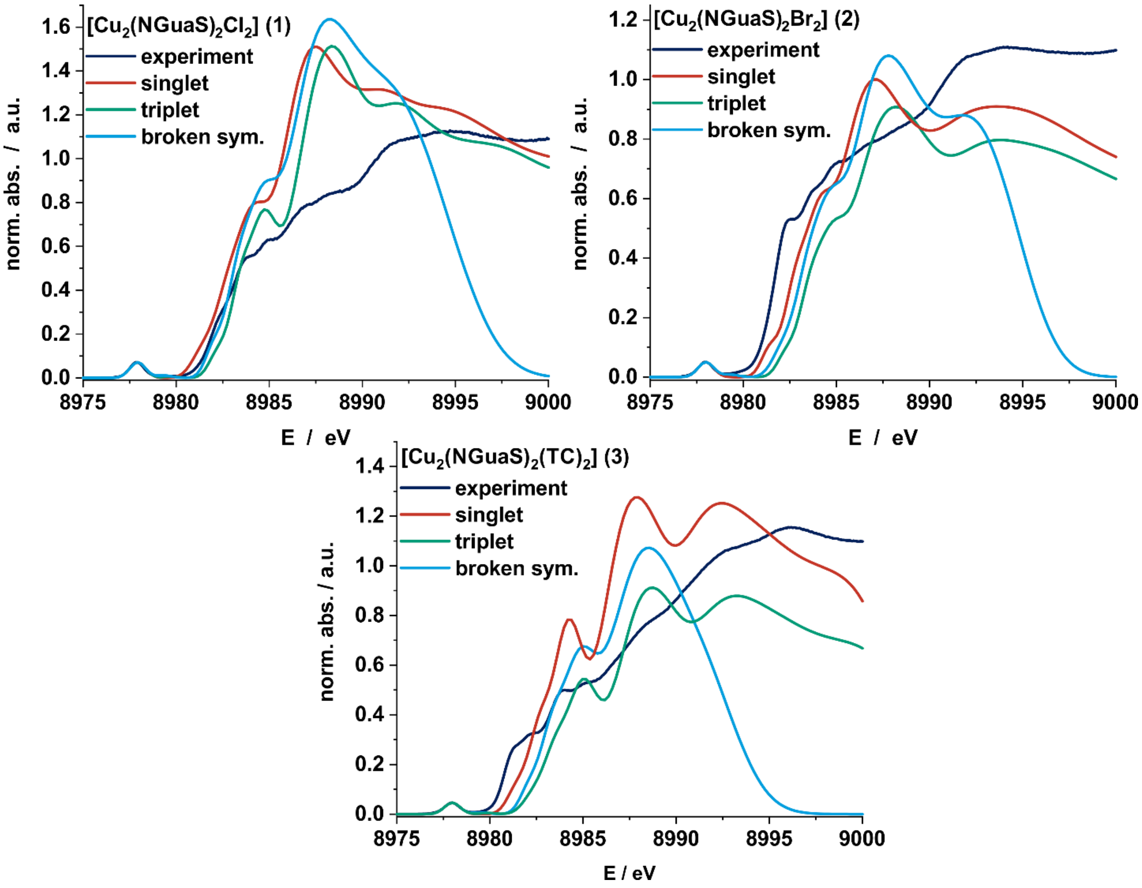

Figure 3: Comparison of the experimental spectrum with the three calculated spectra for different multiplicity solutions.

As already mentioned, the first feature in the spectrum of **1** is the prepeak at 8977.9 eV. A detailed look on the theoretical calculations reveals a 1s → LUMO transition underneath this signal, which is well known for Cu(II) complexes and this assignment is also valid for complexes **2** and **3**, as deduced from the acceptor orbitals displayed in figure 4. The composition in terms of orbital contributions is summarized in table 1 and reveals the binding combination of copper 3d and sulfur 3p orbitals.

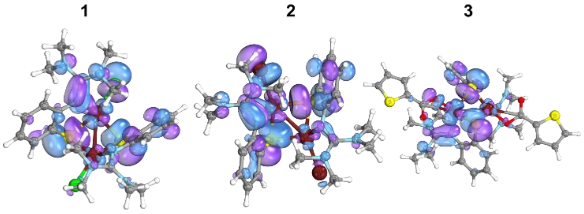

Figure 4: Spatial distribution of the LUMO orbitals of all three complexes.

Table 1: Orbital contributions to the alpha and beta spin LUMOs of the three complexes under investigation.

LUMO contributions / %	Cu		S		N	C
prepeak	p	d	p	d	p	P
1: alpha / beta spin	2.0 / 1.0	40.0 / 39.9	24.0 / 24.0	0.9 / 0.7	5.2 / 5.3	8.9 / 8.8
2: alpha / beta spin	2.3 / 2.3	38.1 / 38.2	24.7 / 24.7	0.6 / 0.6	5.4 / 5.4	9.2 / 9.2
3: alpha / beta spin	2.1 / 2.1	42.9 / 42.9	24.7 / 24.7	0.7 / 0.7	5.1 / 5.1	8.1 / 8.1

The following features are assigned to transitions from the copper 1s into π* orbitals of the ligand system. These orbitals are strongly delocalized and therefore a detailed assignment to single parts or atoms of the ligand is hardly possible. However, the feature at 8983.4 eV (see figure 5 for the sulfur projection of the relevant transitions of **1** and the Supporting Information for additional spectra) can be assigned to the 3p and 3d orbitals of the bridging sulfurs (combination with Cu 3p, see table S2 in the Supporting Information).

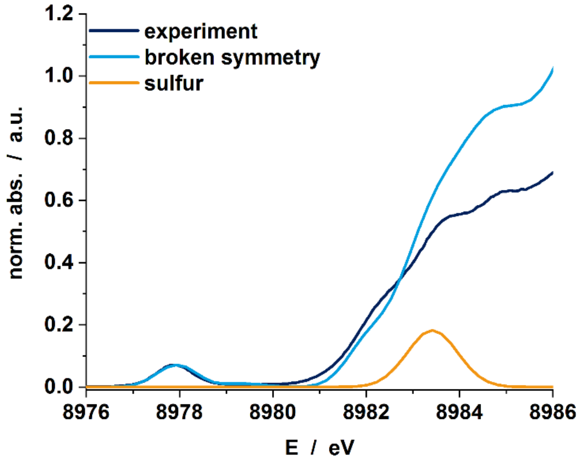

Figure 5: Ligand (sulfur) projection of relevant transitions in the XANES spectrum of **1** in comparison to the complete experimental and calculated spectrum.

Since the sulfur bridges in biomimetic Cu$_A$ models are of utmost importance for the electron transfer capabilities of such systems, details of the electronic structure of the Cu-S motif are highly desirable factors to be investigated experimentally. As the spectroscopic signature of the Cu-S motif contained in the HERFD-XANES spectra are falling in the edge, the potential of this technique is rather limited, which is also obvious from the mismatch between calculations and experiment in case of complexes **2** and **3**. Thus the information to be extracted from the simulations need to be treated with care and should only be used as rough estimate of the underlying quantum mechanical levels. Still, this piece of information is important for future in-situ studies. In order to overcome this limitations, VtC-XES measurements are employed in the following, as this technique offers a higher specificity towards different coordinating atoms.[40]

The experimental spectra given in figure 6 show one very intense feature and a very broad asymmetric slope to lower energies. A comparison with the calculated spectra reveals three peaks underlying these spectra in each case.

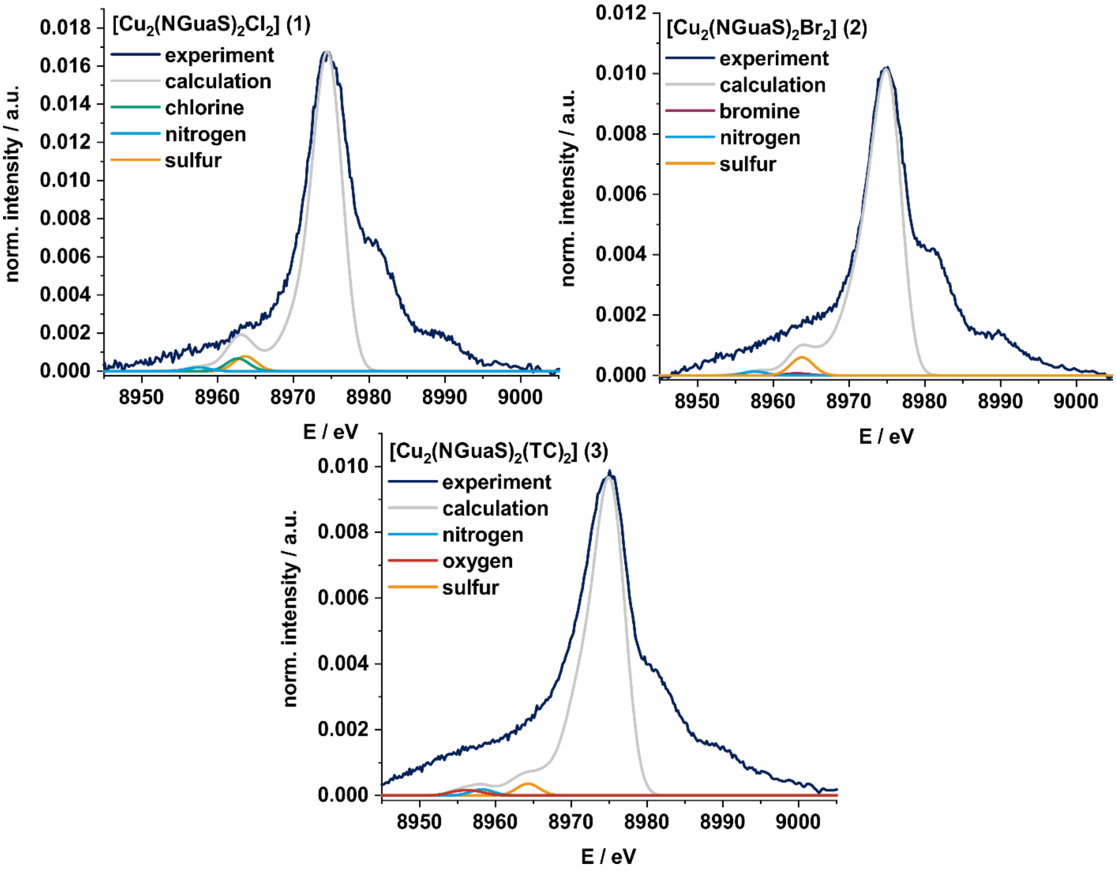

Figure 6: Comparison of the experimental VtC spectra of **1** (top left), **2** (top right) and **3** (bottom) with the calculated ones as well as the ligand projected spectra as denoted.

The main peak consists of transitions from bonding combinations of the copper 3d and ligand p orbitals into the 1s orbital. Considering that all parts of the ligand play a role in numerous transitions underlying this signal, no further assignment to structural fragments was carried out. Since this signal shows hardly any differences between the three complexes **1**, **2** and **3**, it can be concluded that the copper dominated states are nearly identical in these complexes. The differences between the three complexes appear in the low energy Kβ'' or crossover peaks, which are by ligand s to metal s transitions.[41] In **1**, the ligand projection shows a close proximity of the signals caused by 3s→1s transitions from the bridging sulfur atom of the guanidine ligand and the terminal chloride ligand. These two overlapping contributions are responsible for the feature at 8963 eV. The smallest intensity peak at 8957.6 eV originates from transitions of the guanidine nitrogen 2s orbitals. For **2** the situation is a little different because of the exchange of the chloride by bromide ligands. This leads to a significantly reduced halide contribution to the peak at 8963 eV, which thus becomes dominated by the sulfur signal. The reduced halide signal intensity is explained by the shift of the halide s levels to higher energy with increasing atomic number,[42] which in turn causes an energy shift of the crossover signals. Since complex **3** contains no halide ligand the situation differs a little more. The peak at 8963 eV can be assigned mainly to the sulfur-containing ligand with a minor fraction of the remaining ligands. The low energy signal of little intensity is in contrast a combination of signals from the oxygen 2s of the thiophene-carboxylate ligand and the nitrogen 2s of the guanidine ligand. Since these two transitions are close in energy, they largely overlap, which is the reason why this signal is a little more intense and broadened compared to **1** and **2**. All exact orbital compositions of the preceding discussion are given in the supplementary information. The two higher energy features found in all spectra are tentatively attributed to KβL channels.[43] Although such effects are not expected at the used excitation energy, these spectral signatures are found in all published Cu VtC-XES studies.[44,45] Accordingly, a physical origin of general character seems to be present and a structural interpretation might not be appropriate.

Since a mixed valence Cu(I)/Cu(II) compound is a prerequisite for Cu_A activity, the possibility to investigate such mixed states by X-ray spectroscopy is addressed by theoretical spectroscopy for the example of **1**. The structural motif of the Cu_2S_2 core stays intact upon reduction, while the involved Cu-S and Cu-Cu bond lengths change. The Cu-Cu distance reduces from 2.747 to 2.619 Å and conditionally two Cu-S distances elongate by approx. 0.1 Å (see Supporting Information). As can be expected, the VtC-XES spectra show a shift to lower energies by formal reduction from Cu^{2+}…Cu^{2+} to $Cu^{1.5+}$…$Cu^{1.5+}$, while the general shape of the spectra is nearly unaffected. The low intensity peak around 8948 eV, which consists of the Cu-Cl and Cu-S crossover peaks loses some intensity though. This can be explained with the aforementioned elongation of the Cu-S bonds in the core and the concomittant loss of intensity due to worse orbital overlap.[36]

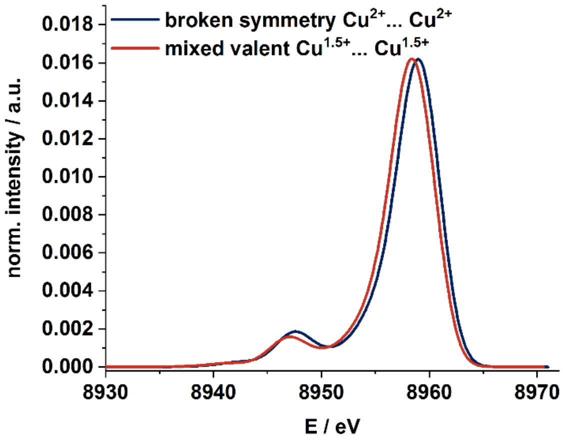

Figure 7: Comparison of the calculated VtC-spectra of **1** and the reduced species of **1**.

For the HERFD-XANES spectrum given in figure 8, a significant change for the mixed valent state is observed in the prepeak and the first feature after the prepeak. The prepeak shifts to lower energies due to the reduced oxidation state and the intensity decreases due to the reduced number of d orbital vacancies. The second peak following the prepeak at higher energy can be assigned to MLCT transitions from the copper centers to the bridging sulfur atoms and the guanidine moiety (see Supporting Information Figure S2 and Table S3), which is in line with the strong electron transfer capabilities of Cu_A systems and is just another indication towards the fact that a mixed valent compound is necessary.

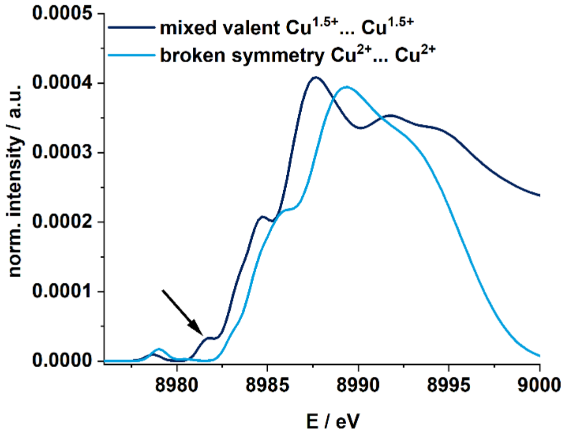

Figure 8: Comparison of the calculated spectrum for **1** and the reduced species of **1**. The arrow points to the MLCT transitions, which is the most significant change when calculating the mixed valent compound. Although such transitions can be found for the broken symmetry $Cu^{2+}…Cu^{2+}$ ground state as well the intensity is much weaker.

CONCLUSION

The recent methods HERFD-XANES and VtC-XES were established as hard X-ray techniques to study biomimetic complexes that reflect important Cu_A properties. For this purpose, a set of three compounds of general formula $[Cu_2(NGuaS)_2X_2]$ with X = Cl (**1**), Br (**2**) and thiophenecarboxylate (**3**) which are characterized by identical Cu_2S_2 core portions and only different anionic ligands was chosen as subject. By comparison with theoretical TD-DFT calculations, it is possible to detect spin and oxidation state changes as well as charge transfer capabilities. HERFD-XANES offers a tremendous advancement compared to conventional XANES spectroscopy, which allows a more precise analysis of the prepeak region, which is of central interest. In the studied complexes only a broken symmetry ground state can be brought into agreement with the experimental spectra, and the prepeak is caused by a Cu(1s) → Cu(3d)/S(3p) transition. But moreover, also the continuum-like first resonances in the edge can be addressed with the applied methodology to Cu(1s) → ligand(π*) transitions, thus it is obvious that from the HERFD-XANES particular details of such states in Cu_A models can be obtained.

This enhanced resolution towards ligand states is even increased by valence-to-core XES. It was demonstrated here that in particular the cross-over or Kβ” signal is of pronounced diagnostic value for changes in the ligand environment of the investigated complexes, while the Cu_2S_2 core remains unchanged. Finally, VtC-XES is also able to follow the formation and fate of mixed-valent states, which are responsible for the enzymatic activity of Cu_A systems. By means of theoretical spectroscopy, it could be shown that a shift of the spectra is reflecting the change in oxidation state, while changes in the cross-over signal are reflecting alterations in the bond lengths.

With the presented approach it should therefore be possible to not only get insight into possible electron pathways in catalytic systems but to also predict spectral changes by theoretical spectroscopy due to the significant observed changes. The results form a basis for future ground-state, kinetic and even ultra-fast pump-probe experiments in the field, using the powerful techniques HERFD-XANES and VtC-XES.

AUTHOR INFORMATION

Corresponding Author

E-mail: matthias.bauer@uni-paderborn.de.

Notes

The authors declare no competing financial interest.

SUPPORTING INFORMATION

X-ray crystallography of [$Cu_2(NGuaS)_2(TC)_2$], acceptor and donor orbital contributions of selected transitions, geometric parameters of the geometries used in the calculations and additional computed spectra. This material is available free of charge via the Internet at http://pubs.acs.org.

ACKNOWLEDGMENT

The ESRF is acknowledged for a provision of beamtime. We thank the staff of beamline ID26 for support during the measurements. The German DFG is acknowledged for funding in frame of the Forschergruppe 1405. Generous grant of computer time at the Paderborn Center for Parallel Computing PC^2 is gratefully acknowledged.

REFERENCES

(1) Iwata, S.; Ostermeier, C.; Ludwig, B.; Michel, H. Structure at 2.8 Å Resolution of Cytochrome c Oxidase from Paracoccus Denitrificans. *Nature* **1995**, *376*, 660–669.

(2) Wilmanns, M.; Lappalainen, P.; Kelly, M.; Sauer-Eriksson, E.; Saraste, M. Crystal Structure of the Membrane-Exposed Domain from a Respiratory Quinol Oxidase Complex with an Engineered Dinuclear Copper Center. *Proceedings of the National Academy of Sciences* **1995**, *92*, 11955–11959.

(3) Tsukihara, T.; Aoyama, H.; Yamashita, E.; Tomizaki, T.; Yamaguchi, H.; Shinzawa-Itoh, K.; Nakashima, R.; Yaono, R.; Yoshikawa, S. Structures of Metal Sites of Oxidized Bovine Heart Cytochrome c Oxidase at 2.8 Å. *Science* **1995**, *269*, 1069–1074.

(4) Henkel, G.; Müller, A.; Weissgräber, S.; Buse, G.; Soulimane, T.; Steffens, G. C. M.; Nolting, H.-F. The Active Sites of the Native Cytochrome-c Oxidase from Bovine Heart Mitochondria: EXAFS-Spectroscopic Characterization of a Novel Homobinuclear Copper Center(Cu_A) and of the Heterobinuclear Fe_{a3}-Cu_B Center. *Angewandte Chemie International Edition in English* **1995**, *34*, 1488–1492.

(5) Blackburn, N. J.; Vries, S. de; Barr, M. E.; Houser, R. P.; Tolman, W. B.; Sanders, D.; Fee, J. A. X-ray Absorption Studies on the Mixed-Valence and Fully Reduced Forms of the Soluble Cu_A Domains of Cytochrome c Oxidase. *Journal of the American Chemical Society* **1997**, *119*, 6135–6143.

(6) Brown, K.; Tegoni, M.; Prudêncio, M.; Pereira, A. S.; Besson, S.; Moura, J. J.; Moura, I.; Cambillau, C. A Novel Type of Catalytic Copper Cluster in Nitrous Oxide Reductase. *Nature Structural Biology* **2000**, *7*, 191–195.

(7) Paraskevopoulos, K.; Antonyuk, S. V.; Sawers, R. G.; Eady, R. R.; Hasnain, S. S. Insight into Catalysis of Nitrous Oxide Reductase from High-resolution Structures of Resting and Inhibitor-bound Enzyme from Achromobacter cycloclastes. *Journal of Molecular Biology* **2006**, *362*, 55–65.

(8) Tsukihara, T.; Aoyama, H.; Yamashita, E.; Tomizaki, T.; Yamaguchi, H.; Shinzawa-Itoh, K.; Nakashima, R.; Yaono, R.; Yoshikawa, S. The Whole Structure of the 13-Subunit Oxidized Cytochrome c Oxidase at 2.8 Å. *Science* **1996**, *272*, 1136–1144.

(9) Hoffman, B. M.; Roberts, J. E.; Swanson, M.; Speck, S. H.; Margoliash, E. Copper Electron-Nuclear Double Resonance of Cytochrome c Oxidase. *Proc. Natl. Acad. Sci. USA* **1980**, *77*, 1452–1456.

(10) Stevens, T. H.; Martin, C. T.; Wang, H.; Brudvig, G. W.; Scholes, C. P.; Chan, S. I. The Nature of Cu_A in Cytochrome c Oxidase. *Journal of Biological Chemistry* **1982**, *257*, 12106–12113.

(11) Hay, M.; Richards, J. H.; Lu, Y. Construction and Characterization of an Azurin Analog for the Purple Copper Site in Cytochrome c Oxidase. *Proceedings of the National Academy of Sciences* **1996**, *93*, 461–464.

(12) Lappalainen, P.; Aasa, R.; Malmstrom, B. G.; Saraste, M. Soluble Cu_A-binding Domain from the Paracoccus Cytochrome c Oxidase. *Journal of Biological Chemistry* **1993**, *268*, 26416–26421.

(13) Pollock, C. J.; DeBeer, S. Insights into the Geometric and Electronic Structure of Transition Metal Centers from Valence-to-Core X-ray Emission Spectroscopy. *Accounts of Chemical Research* **2015**, *48*, 2967–2975.

(14) Bauer, M. HERFD-XAS and Valence-to-Core-XES: New Tools to Push the Limits in Research with Hard X-Rays? *Phys. Chem. Chem. Phys.* **2014**, *16*, 13827–13837.
(15) Bauer, M.; Bertagnolli, H. X-Ray Absorption Spectroscopy - the Method and Its Applications. *Methods in Physical Chemistry*; Wiley-VCH Verlag GmbH & Co. KGaA: Weinheim, Germany, 2012; pp 231–269.
(16) Smolentsev, G.; Soldatov, A. V.; Messinger, J.; Merz, K.; Weyhermüller, T.; Bergmann, U.; Pushkar, Y.; Yano, J.; Yachandra, V. K.; Glatzel, P. X-ray Emission Spectroscopy to Study Ligand Valence Orbitals in Mn Coordination Complexes. *Journal of the American Chemical Society* **2009**, *131*, 13161–13167.
(17) Vollmers, N. J.; Müller, P.; Hoffmann, A.; Herres-Pawlis, S.; Rohrmüller, M.; Schmidt, W. G.; Gerstmann, U.; Bauer, M. Experimental and Theoretical High-Energy-Resolution X-ray Absorption Spectroscopy: Implications for the Investigation of the Entatic State. *Inorganic Chemistry* **2016**, *55*, 11694–11706.
(18) Vankó, G.; Bordage, A.; Glatzel, P.; Gallo, E.; Rovezzi, M.; Gawelda, W.; Galler, A.; Bressler, C.; Doumy, G.; March, A. M., et al. Spin-State Studies with XES and RIXS: From Static to Ultrafast. *Journal of Electron Spectroscopy and Related Phenomena* **2013**, *188*, 166–171.
(19) Naumova, M.; Khakhulin, D.; Rebarz, M.; Rohrmüller, M.; Dicke, B.; Biednov, M.; Britz, A.; Espinoza, S.; Grimm-Lebsanft, B.; Kloz, M., et al. Structural Dynamics upon Photoexcitation-induced Charge Transfer in a Dicopper(I)–disulfide Complex. *Physical Chemistry Chemical Physics* **2018**, *20*, 6274–6286.
(20) Neuba, A.; Haase, R.; Meyer-Klaucke, W.; Flörke, U.; Henkel, G. A Halide-Induced Copper(I) Disulfide/Copper(II) Thiolate Interconversion. *Angewandte Chemie International Edition* **2012**, *51*, 1714–1718.
(21) Neese, F. Software Update: the ORCA Program System, Version 4.0. *WIREs Comput Mol Sci* **2018**, *8*, e1327.
(22) Neese, F. The ORCA Program System. *WIREs Comput Mol Sci* **2012**, *2*, 73–78.
(23) Staroverov, V. N.; Scuseria, G. E.; Tao, J.; Perdew, J. P. Comparative Assessment of a New Nonempirical Density Functional: Molecules and Hydrogen-Bonded Complexes. *The Journal of Chemical Physics* **2003**, *119*, 12129–12137.
(24) Witte, M.; Gerstmann, U.; Neuba, A.; Henkel, G.; Schmidt, W. G. Density Functional Theory of the Cu_A -like Cu_2S_2 Diamond Core in $Cu_2^{II}(NGuaS)_2Cl_2$. *Journal of Computational Chemistry* **2016**, *37*, 1005–1018.
(25) Schäfer, A.; Horn, H.; Ahlrichs, R. Fully Optimized Contracted Gaussian Basis Sets for Atoms Li to Kr. *The Journal of Chemical Physics* **1992**, *97*, 2571.
(26) Weigend, F.; Ahlrichs, R. Balanced Basis Sets of Split Valence, Triple Zeta Valence and Quadruple Zeta Valence Quality for H to Rn: Design and Assessment of Accuracy. *Physical Chemistry Chemical Physics* **2005**, *7*, 3297–3305.
(27) Schäfer, A.; Huber, C.; Ahlrichs, R. Fully Optimized Contracted Gaussian Basis Sets of Triple Zeta Valence Quality for Atoms Li to Kr. *The Journal of Chemical Physics* **1994**, *100*, 5829–5835.
(28) Zheng, J.; Xu, X.; Truhlar, D. G. Minimally Augmented Karlsruhe Basis Sets. *Theoretical Chemistry Accounts* **2011**, *128*, 295–305.
(29) Neese, F.; Wennmohs, F.; Hansen, A.; Becker, U. Efficient, Approximate and Parallel Hartree-Fock and Hybrid DFT Calculations. A 'Chain-of-Spheres' Algorithm for the Hartree-Fock Exchange. *Chemical Physics* **2009**, *356*, 98–109.

(30) Neese, F. An Improvement of the Resolution of the Identity Approximation for the Formation of the Coulomb Matrix. *Journal of Computational Chemistry* **2003**, *24*, 1740–1747.

(31) Grimme, S.; Antony, J.; Ehrlich, S.; Krieg, H. A Consistent and Accurate Ab Initio Parametrization of Density Functional Dispersion Correction (DFT-D) for the 94 Elements H-Pu. *The Journal of Chemical Physics* **2010**, *132*, 154104.

(32) Grimme, S.; Ehrlich, S.; Goerigk, L. Effect of the Damping Function in Dispersion Corrected Density Functional Theory. *Journal of Computational Chemistry* **2011**, *32*, 1456–1465.

(33) Neese, F. Prediction and Interpretation of the 57Fe Isomer Shift in Mössbauer Spectra by Density Functional Theory. *Inorganica Chimica Acta* **2002**, *337*, 181–192.

(34) Runge, E.; Gross, E. K. U. Density-Functional Theory for Time-Dependent Systems. *Physical Review Letters* **1984**, *52*, 997–1000.

(35) Pantazis, D. A.; Chen, X. Y.; Landis, C. R.; Neese, F. All-Electron Scalar Relativistic Basis Sets for Third-Row Transition Metal Atoms. *Journal of Chemical Theory and Computation* **2008**, *4*, 908–919.

(36) Lee, N.; Petrenko, T.; Bergmann, U.; Neese, F.; DeBeer, S. Probing Valence Orbital Composition with Iron Kβ X-ray Emission Spectroscopy. *Journal of the American Chemical Society* **2010**, *132*, 9715–9727.

(37) van Wüllen, C. Molecular Density Functional Calculations in the Regular Relativistic Approximation: Method, Application to Coinage Metal Diatomics, Hydrides, Fluorides and Chlorides, and Comparison with First-Order Relativistic Calculations. *The Journal of Chemical Physics* **1998**, *109*, 392.

(38) Delgado-Jaime, M. U.; DeBeer, S. Expedited Analysis of DFT Outputs: Introducing MOAnalyzer. *Journal of Computational Chemistry* **2012**, *33*, 2180–2185.

(39) Witte, M.; Grimm-Lebsanft, B.; Goos, A.; Binder, S.; Rübhausen, M.; Bernard, M.; Neuba, A.; Gorelsky, S.; Gerstmann, U.; Henkel, G., et al. Optical Response of the Cu_2S_2 Diamond Core in $Cu_2^{II}(NGuaS)_2Cl_2$. *Journal of Computational Chemistry* **2016**, *37*, 2181–2192.

(40) Delgado-Jaime, M. U.; DeBeer, S.; Bauer, M. Valence-to-Core X-Ray Emission Spectroscopy of Iron-Carbonyl Complexes: Implications for the Examination of Catalytic Intermediates. *Chemistry (Weinheim an der Bergstrasse, Germany)* **2013**, *19*, 15888–15897.

(41) Glatzel, P.; Bergmann, U. High Resolution 1s Core Hole X-Ray Spectroscopy in 3d Transition Metal Complexes - Electronic and Structural Information. *Coordination Chemistry Reviews* **2005**, *249*, 65–95.

(42) Bergmann, U.; Horne, C. R.; Collins, T. J.; Workman, J. M.; Cramer, S. P. Chemical Dependence of Interatomic X-Ray Transition Energies and Intensities – a Study of Mn Kβ″ and Kβ2,5 spectra. *Chemical Physics Letters* **1999**, *302*, 119–124.

(43) Glatzel, P. Multiple Excitations in the K Fluorescence Emission of Mn, Fe and Ni Compounds. In *AIP Conference Proceedings*; AIP, 2002; pp 250–255.

(44) Martin-Diaconescu, V.; Chacón, K. N.; Delgado-Jaime, M. U.; Sokaras, D.; Weng, T.-C.; DeBeer, S.; Blackburn, N. J. Kβ Valence to Core X-ray Emission Studies of Cu(I) Binding Proteins with Mixed Methionine – Histidine Coordination. Relevance to the Reactivity of the M- and H-sites of Peptidylglycine Monooxygenase. *Inorganic Chemistry* **2016**, *55*, 3431–3439.

(45) Günter, T.; Carvalho, H. W. P.; Doronkin, D. E.; Sheppard, T.; Glatzel, P.; Atkins, A. J.; Rudolph, J.; Jacob, C. R.; Casapu, M.; Grunwaldt, J.-D. Structural Snapshots of the SCR Reaction Mechanism on Cu-SSZ-13. *Chemical Communications* **2015**, *51*, 9227–9230.

TOC GRAPHIC

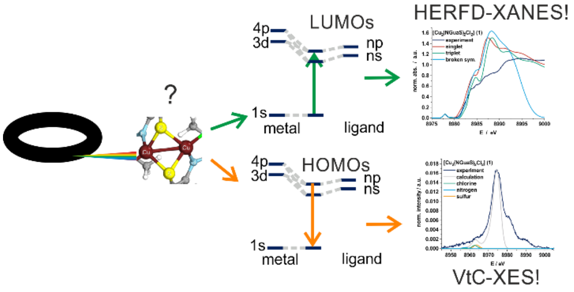
?
LUMOs
HERFD-XANES!
4p
3d
np
ns
1s
metal
ligand
HOMOs
4p
3d
np
ns
1s
metal
ligand
VtC-XES!

Supporting Information

Experimental and Theoretical High Energy Resolution Hard X-Ray Absorption and Emission Spectroscopy on Biomimetic Cu_2S_2 Complexes

Patrick Müller[†], *Adam Neuba*[†], *Ulrich Flörke*, [†] *Gerald Henkel*, [†] *Thomas D. Kühne*, [†#] *Matthias Bauer**[, †#]

[†]Universität Paderborn, Department Chemie, Warburger Straße 100, D-33098 Paderborn, Germany

[#]Center for sustainable systems design (CSSD), Warburger Straße 100, D-33098 Paderborn, Germany

*Corresponding Authors: matthias.bauer@uni-paderborn.de

Table of Contents

Section S1 – Structure Determination of $[Cu_2(NGuaS)_2(TC)_2]$ **(3)**

$C_{32}H_{38}Cu_2N_6O_4S_4$, M_r = 826.0; black needle, 0.47 x 0.03 x 0.02 mm, monoclinic, space group C 2/c, a = 32.043(3), b = 6.9797(7), c = 20.6591(19) Å, β = 129.878(2)°, V = 3545.8(6) $Å^3$, Z = 4, D_c = 1.547 g/cm^3, F(000) = 1704.

The intensity data were recorded using a Bruker SMART diffractometer with graphite monochromated MoK_α radiation ($\lambda = 0.71073$ Å) at T = 120(2) K. 16073 intensities collected, h -42/42, k -9/9, l -25/27; $1.6 < \Theta < 27.9°$. 4229 unique reflections $R_{int} = 0.091$. Structure solutions by direct methods[1], full-matrix least squares refinements[1] based on F^2. All but H-atoms were refined an-isotropically, hydrogen atoms were clearly located from difference Fourier maps, refined at idealized positions riding on the parent atoms with isotropic displacement parameters Hydrogen atoms were located from difference Fourier maps, refined at idealized positions riding on the parent atoms with isotropic displacement parameters $U_{iso}(H) = 1.2U_{eq}(C)$ or $1.5U_{eq}(-CH_3)$ and C-H 0.95-0.98 Å. All CH_3 hydrogen atoms were allowed to rotate but not to tip.

The thiophene group is disordered over two sites A and B with positions S21/C141 for orientation A and S22/C142 for B. Site occupation factors are 0.8 and 0.2 for A and B, respectively. Fixed position and isotropic refinement for C142 was necessary in order to achieve stable convergence at R1 = 0.051 (I > 2s(I)), wR2 = 0.105 (all data), S = 1.03, min/max DF -0.46/0.53 e/A^3.

Complete crystallographic data have been deposited as CCDC 1882197.

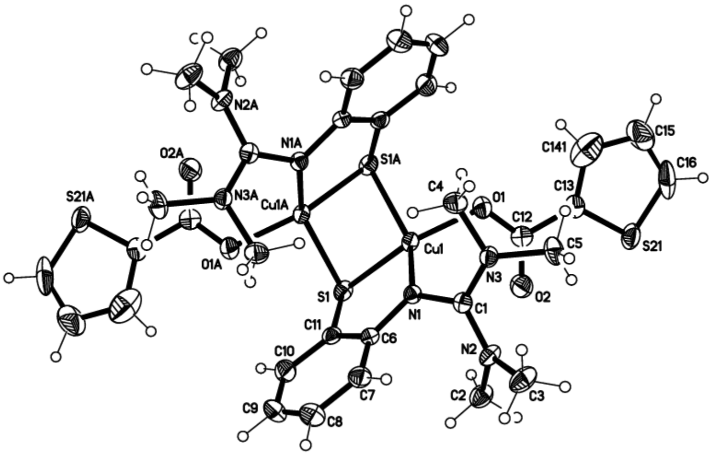

Figure S1: Molecular structure of **3** with anisotropic displacement ellipsoids drawn at 50% probability level. Only orientation A of disordered thiophene groups shown.

Section S2 – Structural parameters of the geometry optimized structures

Table S1: Selected distances in Å of the four complexes under investigation.

Complex	Cu-Cu	Cu-S
[Cu$_2$(NGuaS)$_2$Cl$_2$] (**1**)	2.74741	2.25764, 2.32107 2.32055, 2.25740
[Cu2(NGuaS)$_2$Br$_2$] (**2**)	2.72464	2.26416, 2.31204 2.31185, 2.26437
[Cu2(NGuaS)$_2$(TC)$_2$] (3)	2.73399	2.24606, 2.33995 2.33995, 2.24606
mixed valent	2.61873	2.36798, 2,33678 2,33423, 2,36607

Section S2 – Orbital compositions and spatial distributions of selected acceptor orbitals

Table S2: Acceptor orbital contribution for the transition from the copper 1s into the copper 3p / sulfur 3p/3d orbital.

Orbital contribution	Cu		S		N		C	
Cu 3p / S 3p/3d	p	d	p	d	s	p	s	p
alpha spin	20.4%	3.1%	11.4%	20.1%	0.4%	3.7%	3.8%	14.5%
beta spin	29.2%	3.9%	11.6%	19.5%	0.6%	4.0%	4.4%	13.6%

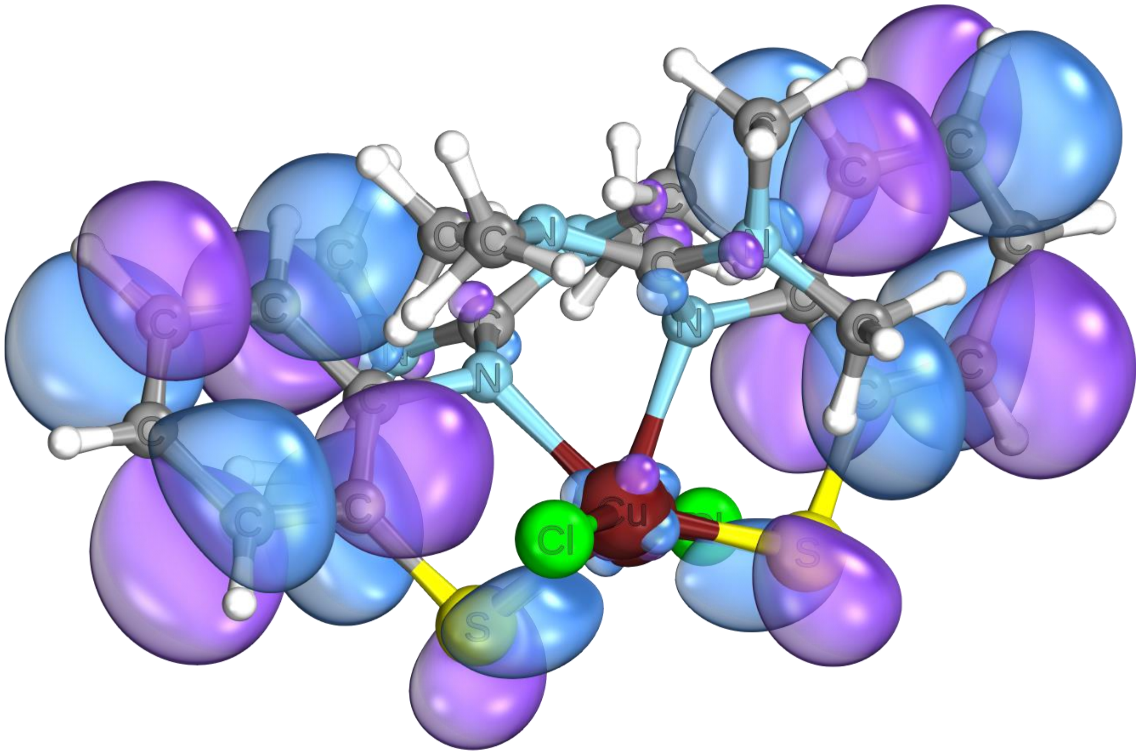

Figure S2: Spatial distribution of one of the acceptor orbitals of the MLCT transition in the reduced mixed valent compound.

Table S3: Orbital contributions to one of the acceptor orbitals of the MLCT transition in the reduced mixed valent compound.

Acceptor orbital contributions	Cu		S		N		C	
MLCT	p	d	p	d	s	p	s	p
alpha spin	0.8%	0.7%	3.6%	2.9%	0.0%	0.4%	0.0%	62.0%
beta spin	0.8%	0.8%	3.6%	2.7%	0.0%	0.4%	0.0%	62.1%

Section S4 – Orbital compositions of selected donor orbitals

Table S4: Orbital compositions in percent for the donor orbitals contributing to the valence-to-core peaks in complex **1.**

Donor orbital contributions	Cl		Cu		S		N		C		H	
8963 eV - S	s	p	p	d	s	p	s	p	s	p	s	p
Orbital 86	2.1 / 2.1	0 / 0	4.6 / 4.7	0 / 0	22.1 / 22.1	0.8 / 0.8	1.3 / 1.3	2.8 / 2.8	19.3 / 19.3	30.5 / 30.2	6.7 / 6.7	0.2 / 0.2
Orbital 87	0 / 0	0 / 0	3.5 / 3.5	0.5 / 0.5	25.1 / 25.1	0 / 0	1.1 / 1.1	2.6 / 2.6	18.9 / 18.9	33.1 / 33.0	6.7 / 6.1	0.2 / 0.2
8963 eV - Cl												
Orbital 82	67.0 / 66.9	0 / 0	7.1 / 7.2	0.7 / 0.7	0.4 / 0.4	0 / 0	1.0 / 1.0	2.1 / 2.1	6.9 / 7.0	4.8 / 6.9	3.4 / 3.5	0 / 0
Orbital 83	58.6 / 58.3	0 / 0	5.7 / 5.6	0.5 / 0.6	0.6 / 0.6	0 / 0	1.8 / 1.8	3.3 / 3.4	10.2 / 10.2	6.9 / 7.0	5.2 / 5.2	0.2 / 0.3
8957.6 eV - N												
Orbital 70	0 / 0	0 / 0	1.4 / 1.4	0 / 0	0.5 / 0.5	0.4 / 0.4	30.3 / 30.2	4.5 / 4.6	26.7 / 26.9	23.7 / 23.7	2.3 / 2.1	0 / 0
Orbital 71	0 / 0	0 / 0	1.8 / 1.8	0 / 0	0.4 / 0.4	0.4 / 0.4	30.3 / 30.2	4.7 / 4.6	27.3 / 27.1	23.6 / 23.8	2.3 / 2.2	0 / 0

Values presented are for alpha / beta spin respectively.

Table S5: Orbital compositions in percent for the donor orbitals contributing to the valence-to-core peaks in complex **2.**

Donor orbital contributions	Br		Cu		S		N		C		H	
8963 eV - S	s	p	p	d	s	p	s	p	s	p	s	p
Orbital 104	5.3 / 5.3	0 / 0	5.3 / 5.3	0 / 0	21.2 / 21.2	0.6 / 0.6	1.2 / 1.2	2.7 / 2.6	18.5 / 18.5	29.0 / 28.7	6.6 / 6.6	0.2 / 0.1
Orbital 105	0 / 0	0 / 0	3.5 / 3.6	0.6 / 0.5	25.0 / 25.0	0 / 0	1.1 / 1.1	2.6 / 2.6	18.8 / 18.8	32.9 / 33.0	6.8 / 6.8	0.2 / 0.1
8963 eV - Br												
Orbital 102	81.8 / 81.9	0 / 0	5.9 / 5.7	0.9 / 0.9	1.0 / 1.0	0.3 / 0.3	0 / 0	0.3 / 0.3	1.2 / 1.3	2.1 / 2.0	0.2 / 0.2	0 / 0
Orbital 103	83.6 / 83.6	0 / 0	8.2 / 8.1	0.9 / 0.9	0.5 / 0.5	0.1 / 0.1	0.1 / 0.1	0.2 / 0.2	0.6 / 0.6	1.1 / 1.0	0 / 0	0 / 0
8957.6 eV - N												
Orbital 88	0 / 0	0 / 0	1.3 / 1.3	0 / 0	0.5 / 0.5	0.4 / 0.4	30.4 / 30.3	4.5 / 4.7	27.0 / 26.8	23.9 / 23.6	2.2 / 2.2	0 / 0
Orbital 89	0 / 0	0 / 0	1.8 / 1.9	0 / 0	0.4 / 0.4	0.5 / 0.4	30.2 / 30.3	4.5 / 4.5	27.0 / 26.9	23.6 / 23.6	2.3 / 2.5	0 / 0

Table S6: Orbital compositions in percent for the donor orbitals contributing to the valence-to-core peaks in complex **3.**

Donor orbital contributions	Cu		S		O		N		C		H	
8963 eV - S	p	d	s	p	s	p	s	p	s	p	s	p
Orbital 108	3.5 / 3.5	0.3 / 0.3	22.3 / 22.3	0.8 / 0.8	0 / 0	0 / 0	1.3 / 1.3	3.0 / 3.0	20.2 / 20.2	30.6 / 30.6	6.5 / 6.5	0.2 / 0.2
Orbital 109	3.4 / 3.4	0.6 / 0.6	25.7 / 25.7	0.2 / 0.2	0 / 0	0 / 0	1.0 / 1.0	2.4 / 2.4	18.6 / 18.6	33.5 / 33.5	6.4 / 6.4	0.2 / 0.2
8957.6 eV - O												
Orbital 80	2.3 / 2.3	0.2 / 0.2	0 / 0	0.2 / 0.2	46.4 / 46.4	7.9 / 7.9	1.1 / 1.1	0.2 / 0.2	25.7 / 25.7	7.7 / 7.7	0.2 / 0.2	0 / 0
Orbital 81	2.4 / 2.4	0.1 / 0.2	0 / 0	0.2 / 0.2	46.1 / 46.1	7.9 / 7.9	1.3 / 1.3	0.2 / 0.2	25.7 / 25.7	7.5 / 7.5	0.2 / 0.2	0 / 0
Orbital 84	0.7 / 0.7	0.2 / 0.2	0 / 0	0 / 0	53.8 / 53.7	2.6 / 2.6	2.3 / 2.3	0.2 / 0.2	1.2 / 1.4	29.8 / 29.8	0.3 / 0.3	0 / 0
Orbital 85	0.7 / 0.7	0.2 / 0.2	0 / 0	0 / 0	52.2 / 52.2	2.5 / 2.5	3.3 / 3.3	0.3 / 0.3	1.9 / 1.8	29.9 / 30.0	0.8 / 0.8	0 / 0
8957.6 eV - N												
Orbital 88	1.5 / 1.6	0.1 / 0.1	0.6 / 0.6	0.4 / 0.4	0 / 0	0 / 0	30.3 / 30.4	4.4 / 4.5	26.9 / 27.0	23.6 / 23.5	2.3 / 2.3	0 / 0
Orbital 89	1.8 / 1.8	0 / 0	0.4 / 0.4	0.4 / 0.4	0 / 0	0 / 0	30.2 / 30.2	4.4 / 4.4	27.5 / 27.4	23.4 / 23.4	2.3 / 2.3	0 / 0

Section S3 – XYZ coordinates

$[Cu_2(NGuaS)_2Cl_2]$ (1)

Cl	-0.087728000	0.039933000	2.240712000
Cu	-0.203953000	-0.050400000	0.022590000
Cu	-0.226102000	-1.644671000	-2.350860000
S	0.536935000	0.549866000	-2.045958000
S	0.720147000	-2.171568000	-0.347236000
N	-1.879055000	0.996354000	-0.398644000
N	-3.152119000	0.690665000	1.513279000
N	-2.681485000	2.857152000	0.809134000
N	-1.766627000	-2.830214000	-1.806122000
N	-2.498763000	-4.757936000	-2.951874000
N	-3.204983000	-2.642895000	-3.613655000
C	-2.571461000	1.513162000	0.618808000
C	-3.223098000	1.014419000	2.935369000
H	-2.727642000	1.963297000	3.121134000
H	-2.686102000	0.239635000	3.485086000
H	-4.261858000	1.059766000	3.276197000
C	-3.312795000	-0.725973000	1.204468000
H	-3.359699000	-0.859060000	0.128045000
H	-4.238465000	-1.078605000	1.665216000
H	-2.468662000	-1.296882000	1.599956000
C	-3.878416000	3.479649000	1.350223000
H	-4.639733000	2.721826000	1.521916000
H	-4.260759000	4.206803000	0.625492000
H	-3.673286000	4.002056000	2.289621000
C	-1.686028000	3.763277000	0.255004000
H	-0.764062000	3.215765000	0.073472000
H	-1.495087000	4.553341000	0.985302000
H	-2.028030000	4.212656000	-0.682864000
C	-0.933972000	1.346991000	-2.593231000
C	-1.060276000	1.767601000	-3.919231000
H	-0.244567000	1.575583000	-4.604370000
C	-2.221827000	2.389897000	-4.353375000
H	-2.311754000	2.709291000	-5.384560000
C	-3.273996000	2.583273000	-3.458641000
H	-4.192204000	3.054327000	-3.791281000
C	-3.164499000	2.156431000	-2.142623000
H	-4.002097000	2.275096000	-1.464340000
C	-1.992480000	1.538216000	-1.681902000
C	-0.631113000	-3.089236000	0.309211000
C	-0.619840000	-3.513291000	1.640112000
H	0.226129000	-3.249392000	2.261660000
C	-1.687876000	-4.230121000	2.160172000
H	-1.671729000	-4.551176000	3.194629000
C	-2.784854000	-4.516188000	1.347873000
H	-3.631791000	-5.061862000	1.748624000
C	-2.812444000	-4.087609000	0.028079000
H	-3.686236000	-4.279776000	-0.584606000
C	-1.735680000	-3.374140000	-0.519161000
C	-2.488427000	-3.408495000	-2.768507000
C	-1.391583000	-5.574430000	-2.475977000
H	-0.507756000	-4.950595000	-2.364350000
H	-1.190856000	-6.349519000	-3.219578000
H	-1.622531000	-6.045992000	-1.515357000
C	-3.676859000	-5.481571000	-3.400540000
H	-4.509226000	-4.790726000	-3.515659000
H	-3.942249000	-6.232670000	-2.648464000
H	-3.499535000	-5.991990000	-4.352127000
C	-3.359531000	-2.978436000	-5.026327000

H	-2.804835000	-3.885046000	-5.251390000
H	-2.931572000	-2.165361000	-5.615095000
H	-4.414587000	-3.109555000	-5.285029000
C	-3.463994000	-1.244178000	-3.290312000
H	-3.433070000	-1.109577000	-2.213487000
H	-4.452001000	-0.976886000	-3.672323000
H	-2.708925000	-0.603560000	-3.753354000
Cl	-0.268272000	-1.733407000	-4.571455000

$[Cu_2(NGuaS)_2Cl_2]^-$ (reduced)

Cl	0.087607000	0.523838000	2.122699000
Cu	-0.183793000	-0.114814000	-0.077724000
Cu	-0.207297000	-1.575386000	-2.251177000
S	0.512919000	0.678550000	-2.159501000
S	0.702361000	-2.303677000	-0.225676000
N	-2.014751000	0.832454000	-0.505463000
N	-3.153438000	0.590714000	1.508782000
N	-2.628773000	2.742722000	0.749313000
N	-1.920610000	-2.665603000	-1.683116000
N	-2.447973000	-4.629839000	-2.891354000
N	-3.228944000	-2.541127000	-3.604572000
C	-2.597228000	1.379223000	0.551102000
C	-3.087081000	0.936073000	2.923825000
H	-2.617070000	1.917023000	3.045515000
H	-2.448322000	0.202241000	3.438214000
H	-4.096171000	0.937963000	3.373273000
C	-3.312639000	-0.830663000	1.233398000
H	-3.450504000	-0.982080000	0.159202000
H	-4.184794000	-1.209822000	1.788297000
H	-2.415095000	-1.385984000	1.549444000
C	-3.791505000	3.430751000	1.267445000
H	-4.576185000	2.702436000	1.506993000
H	-4.184390000	4.131355000	0.505910000
H	-3.555175000	4.010945000	2.178426000
C	-1.554982000	3.565711000	0.216486000
H	-0.673921000	2.934486000	0.045271000
H	-1.297460000	4.335339000	0.962697000
H	-1.840549000	4.057865000	-0.730783000
C	-1.028293000	1.378980000	-2.661943000
C	-1.193102000	1.863171000	-3.972239000
H	-0.357921000	1.757230000	-4.667183000
C	-2.393418000	2.447573000	-4.384045000
H	-2.499783000	2.811916000	-5.409157000
C	-3.462067000	2.545664000	-3.481243000
H	-4.412486000	2.986189000	-3.795166000
C	-3.321185000	2.051149000	-2.182237000
H	-4.167556000	2.084279000	-1.490718000
C	-2.117606000	1.455097000	-1.751238000
C	-0.732012000	-3.130586000	0.388621000
C	-0.753540000	-3.632742000	1.702016000
H	0.120186000	-3.458519000	2.332807000
C	-1.863829000	-4.321223000	2.196899000
H	-1.859186000	-4.699218000	3.222532000
C	-2.985843000	-4.507848000	1.376654000
H	-3.867985000	-5.031025000	1.756454000
C	-2.989440000	-3.994665000	0.077274000
H	-3.880004000	-4.099519000	-0.548471000
C	-1.877216000	-3.295910000	-0.437703000
C	-2.528267000	-3.268313000	-2.694293000
C	-1.262590000	-5.346576000	-2.447960000
H	-0.433476000	-4.635084000	-2.346067000
H	-0.994967000	-6.092555000	-3.214378000
H	-1.424296000	-5.858165000	-1.482005000
C	-3.578821000	-5.425131000	-3.318368000
H	-4.445262000	-4.774177000	-3.489407000
H	-3.841958000	-6.157475000	-2.531355000
H	-3.364288000	-5.982640000	-4.248776000
C	-3.241781000	-2.897434000	-5.018560000
H	-2.668564000	-3.816909000	-5.173853000

H	-2.741184000	-2.101157000	-5.589559000
H	-4.277137000	-3.026715000	-5.381797000
C	-3.486749000	-1.135319000	-3.323291000
H	-3.569147000	-0.987378000	-2.242856000
H	-4.420273000	-0.833531000	-3.822644000
H	-2.659381000	-0.510859000	-3.696862000
Cl	-0.071641000	-2.197928000	-4.469288000

[$Cu_2(NGuaS)_2Br_2$] (2)

Br	0.041825000	0.268993000	2.285707000
Cu	-0.216646000	-0.067496000	-0.047023000
Cu	-0.233177000	-1.629037000	-2.279728000
S	0.516384000	0.550382000	-2.098200000
S	0.704771000	-2.173796000	-0.292055000
N	-1.932481000	0.925273000	-0.452797000
N	-3.202684000	0.649429000	1.466634000
N	-2.645586000	2.803633000	0.782189000
N	-1.820410000	-2.765054000	-1.747012000
N	-2.467007000	-4.701583000	-2.927945000
N	-3.252061000	-2.604314000	-3.563173000
C	-2.596911000	1.460628000	0.581063000
C	-3.290315000	0.974727000	2.888275000
H	-2.746335000	1.892888000	3.089465000
H	-2.808663000	0.171958000	3.448422000
H	-4.332945000	1.072285000	3.205193000
C	-3.363229000	-0.766957000	1.159049000
H	-3.426530000	-0.902379000	0.084244000
H	-4.276539000	-1.125949000	1.637797000
H	-2.507864000	-1.332520000	1.540073000
C	-3.798743000	3.479436000	1.352865000
H	-4.605054000	2.765190000	1.505146000
H	-4.138321000	4.249893000	0.652463000
H	-3.557934000	3.959699000	2.306082000
C	-1.592900000	3.663995000	0.257593000
H	-0.702771000	3.067128000	0.071601000
H	-1.361121000	4.419623000	1.011750000
H	-1.902166000	4.158260000	-0.668612000
C	-0.975401000	1.304700000	-2.634896000
C	-1.109355000	1.718493000	-3.964408000
H	-0.303754000	1.505373000	-4.655560000
C	-2.256248000	2.373193000	-4.385417000
H	-2.349792000	2.695081000	-5.415442000
C	-3.292187000	2.598922000	-3.476834000
H	-4.200630000	3.094133000	-3.801104000
C	-3.184297000	2.166931000	-2.163539000
H	-4.013486000	2.306393000	-1.479156000
C	-2.029650000	1.504715000	-1.715871000
C	-0.671289000	-3.051605000	0.354840000
C	-0.667614000	-3.469531000	1.689812000
H	0.167017000	-3.185065000	2.317944000
C	-1.718791000	-4.218055000	2.195686000
H	-1.705701000	-4.542281000	3.229133000
C	-2.797932000	-4.535345000	1.368398000
H	-3.633372000	-5.104873000	1.759978000
C	-2.827869000	-4.101449000	0.051635000
H	-3.691940000	-4.314083000	-0.567674000
C	-1.771541000	-3.345056000	-0.481470000
C	-2.514899000	-3.358292000	-2.728113000
C	-1.309853000	-5.469704000	-2.487106000
H	-0.460842000	-4.800379000	-2.367408000
H	-1.073931000	-6.206273000	-3.258650000
H	-1.505974000	-5.984595000	-1.541458000
C	-3.600360000	-5.472953000	-3.410285000
H	-4.472469000	-4.828657000	-3.498645000
H	-3.820218000	-6.266213000	-2.687880000
H	-3.394212000	-5.935235000	-4.380382000
C	-3.420578000	-2.941910000	-4.974609000
H	-2.818825000	-3.812351000	-5.218824000

H	-3.051833000	-2.104088000	-5.568157000
H	-4.472553000	-3.127566000	-5.211117000
C	-3.508361000	-1.205429000	-3.241124000
H	-3.496154000	-1.070456000	-2.164489000
H	-4.484688000	-0.928421000	-3.644006000
H	-2.738143000	-0.570736000	-3.688941000
Br	-0.124691000	-1.948330000	-4.626403000

[Cu$_2$(NGuaS)$_2$(TC)$_2$] (3)

Cu	-1.993058000	0.425825000	4.324778000
S	-3.660399000	-0.469429000	5.534440000
S	3.435783000	0.103754000	4.714210000
O	-0.249805000	0.580106000	3.473945000
O	0.560547000	0.130085000	5.523381000
N	-2.102498000	2.053025000	5.529918000
N	-0.404307000	2.845247000	6.967116000
N	-0.394701000	3.378374000	4.702569000
C	-0.985277000	2.755672000	5.743697000
C	-0.572309000	1.781668000	7.949637000
H	-1.306879000	2.058888000	8.712219000
H	0.395441000	1.600491000	8.422384000
H	-0.879696000	0.873906000	7.438591000
C	0.296596000	4.032808000	7.422854000
H	1.364637000	3.844648000	7.570156000
H	-0.133042000	4.349612000	8.378978000
H	0.170374000	4.835980000	6.699791000
C	-1.128164000	3.604211000	3.461618000
H	-0.894299000	2.824192000	2.733985000
H	-0.840362000	4.577964000	3.057786000
H	-2.194044000	3.587906000	3.665904000
C	1.054186000	3.520278000	4.602362000
H	1.359765000	4.569067000	4.663333000
H	1.373777000	3.113146000	3.641775000
H	1.533730000	2.947923000	5.392257000
C	-3.122207000	2.049177000	6.482390000
C	-3.403380000	3.150258000	7.305728000
H	-2.763924000	4.024033000	7.257106000
C	-4.505457000	3.147618000	8.148331000
H	-4.705735000	4.016605000	8.764877000
C	-5.364622000	2.049072000	8.187015000
H	-6.230703000	2.051716000	8.837765000
C	-5.109513000	0.956063000	7.372319000
H	-5.773002000	0.100916000	7.364156000
C	-3.992437000	0.940009000	6.533042000
C	0.702498000	0.331759000	4.309026000
C	2.056318000	0.330283000	3.708011000
C	2.422353000	0.525661000	2.398361000
H	1.691057000	0.686216000	1.618304000
C	3.825283000	0.492703000	2.210553000
H	4.316704000	0.619948000	1.254847000
C	4.500581000	0.274829000	3.384847000
H	5.567639000	0.197507000	3.529154000
Cu	-4.629805000	0.425944000	3.602100000
S	-2.962525000	-0.469315000	2.392363000
S	-10.058802000	0.105884000	3.212597000
O	-6.373018000	0.580362000	4.452975000
O	-7.183534000	0.131195000	2.403423000
N	-4.520226000	2.053236000	2.397117000
N	-6.218434000	2.845122000	0.959755000
N	-6.228495000	3.377923000	3.224423000
C	-5.637535000	2.755698000	2.183227000
C	-6.050170000	1.781517000	-0.022692000
H	-5.315540000	2.058794000	-0.785194000
H	-7.017836000	1.600190000	-0.495553000
H	-5.742728000	0.873820000	0.488441000
C	-6.919436000	4.032562000	0.503841000
H	-7.987443000	3.844271000	0.356465000
H	-6.489752000	4.349316000	-0.452280000

H	-6.793360000	4.835825000	1.226822000
C	-5.495204000	3.603895000	4.465447000
H	-5.728643000	2.823568000	5.192886000
H	-5.783581000	4.577386000	4.869502000
H	-4.429310000	3.588249000	4.261191000
C	-7.677476000	3.518795000	3.324712000
H	-7.983800000	4.567374000	3.263912000
H	-7.996729000	3.111295000	4.285257000
H	-8.156661000	2.946210000	2.534767000
C	-3.500427000	2.049481000	1.444742000
C	-3.219115000	3.150644000	0.621560000
H	-3.858494000	4.024470000	0.670260000
C	-2.116985000	3.148024000	-0.220974000
H	-1.916596000	4.017077000	-0.837390000
C	-1.257920000	2.049404000	-0.259762000
H	-0.391802000	2.052057000	-0.910464000
C	-1.513179000	0.956301000	0.554762000
H	-0.849772000	0.101090000	0.562840000
C	-2.630305000	0.940231000	1.393970000
C	-7.325402000	0.332484000	3.617850000
C	-8.679221000	0.331374000	4.218874000
C	-9.045182000	0.526910000	5.528522000
H	-8.313832000	0.687349000	6.308551000
C	-10.448084000	0.493618000	5.716480000
H	-10.939421000	0.620488000	6.672278000
C	-11.123438000	0.275236000	4.542312000
H	-12.190471000	0.197237000	4.398183000

Section S6 – Sulfur projected HERFD-XANES spectra of complexes **2** and **3**

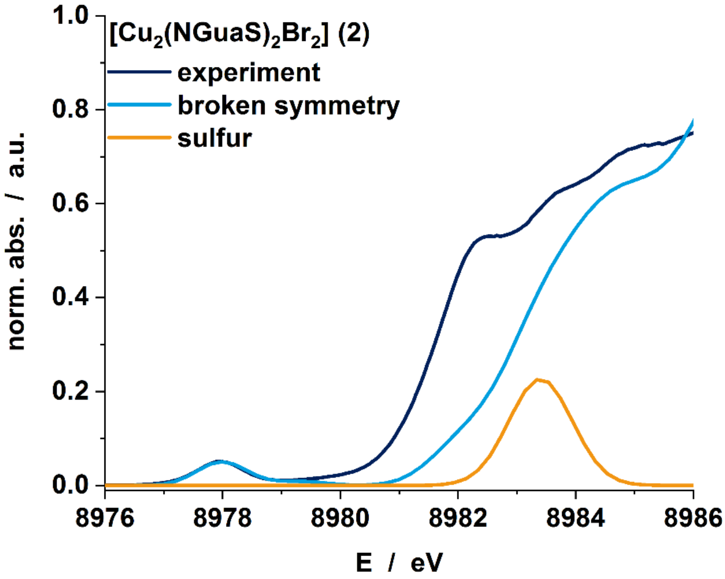

Figure S3: Ligand (sulfur) projected XANES spectrum of **2** in comparison to the complete experimental and calculated spectrum.

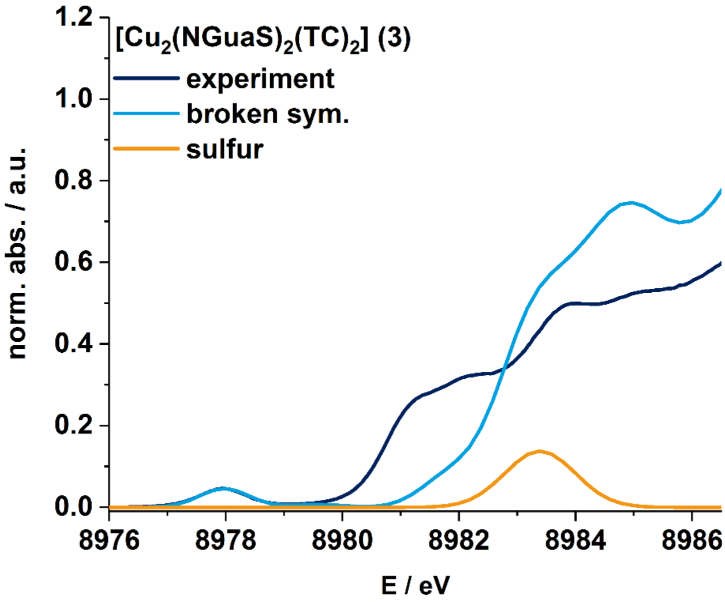

Figure S4: Ligand (sulfur) projected XANES spectrum of **3** in comparison to the complete experimental and calculated spectrum.

Section S7 – XES extraction procedure and XANES normalization

In order to remove the background resulting from the high energy slope of the kb$_{1,3}$ we masked the valence-to-core signal and then fitted the background with an exponential decay function of the following type..

$$y = y_0 + A_1 e^{-x/t_1} + A_2 e^{-x/t_2}$$

where y_0 is the offset, A_1, A_2 are amplitudes and t_1, t_2 are decay constants.

Then the resulting fit function is subtracted from the raw data and the background corrected spectrum is obtained. One example of the raw data, the fit function and the resulting spectrum is shown in figure S5.

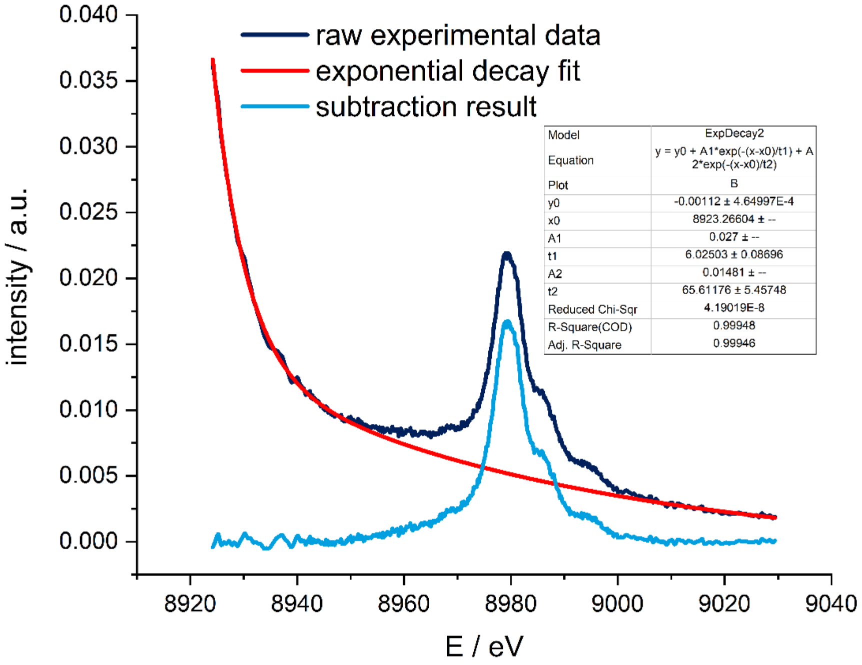

Model	ExpDecay2
Equation	y = y0 + A1*exp(-(x-x0)/t1) + A 2*exp(-(x-x0)/t2)
Plot	B
y0	-0.00112 ± 4.64997E-4
x0	8923.26604 ± --
A1	0.027 ± --
t1	6.02503 ± 0.08696
A2	0.01481 ± --
t2	65.61176 ± 5.45748
Reduced Chi-Sqr	4.19019E-8
R-Square(COD)	0.99948
Adj. R-Square	0.99946

Figure S5: Raw experimental spectrum, exponential decay fit of the background and resulting corrected spectrum after subtraction of the background.

The HERFD-XANES spectra were normalized using the approach implemented in Athena[2]. The normalization algorithm uses three ranges: a post and a pre edge as well as a normalization range. While the pre edge region is fitted with a line, the normalization and post edge are fitted by polynomials.

References

(1) Sheldrick, G. M. Crystal Structure Refinement with SHELXL. *Acta crystallographica. Section C, Structural chemistry* **2015**, *71*, 3–8.

(2) Ravel, B.; Newville, M. ATHENA, ARTEMIS, HEPHAESTUS: Data Analysis for X-Ray Absorption Spectroscopy using IFEFFIT. *Journal of synchrotron radiation* **2005**, *12*, 537–541.

Chapter 4: Conclusion and Outlook

The goal of this work was the establishment of (high energy resolution) X-ray absorption and emission techniques as well as computational methods to describe and analyse these spectra. The chemical focus was on biomimetic copper compounds in-situ and ex-situ. In the first work HERFD-XANES in combination with two theoretical approaches was used to show that it is possible to reveal even small geometric changes between two structurally similar complexes. In addition to that oxidation state and electronic structure changes could be extracted.

The Cu(I) complex from this study was then evaluated again in the second study concerning condensed-phase and finite-temperature effects. Therefore we conducted MD simulations and XAS calculations for a single molecule in the gas phase and a crystalline sample. We found that especially periodic boundary conditions improve the results in the higher energy regime. A further quantitative improvement is then achieved by including finite-temperature through the MD simulation. In order to evaluate the feasibility of the theoretical approach concerning compounds in solution we also calculated the spectra of a single molecule in water. Since no experiment was available further conclusions cannot be drawn.

Concerning the different theoretical approaches no easy conclusion can be drawn and the usage, as is often the case, depends on the system under study and available resources. The ORCA TD-DFT approach is fast and describes the prepeak and first edge transitions very well, but the higher energy regime cannot be calculated. The GIPAW method resolves the latter problem and is still feasible on reasonable time scales but obviously already much more expensive than TD-DFT with the inclusion of periodic boundary conditions. The GAPW approach, especially in conjunction with MD, is in nice agreement at low and high energies but is the most expensive approach concerning calculation time.

The third and final study presented here shows HERFD-XANES and VtC-XES in combination with calculations to evaluate their possibilites for studying dinuclear transition metal complexes. In this case three copper compounds sharing the same binding motif were studied. The electronic and geometric structure is elucidated with possible Cu_A functionality in mind. This is found not to be valid since a broken symmetry $Cu^{2+}...Cu^{2+}$ ground state is present. A theoretical study of a reduced species of one of the complexes reveals a mixed valent $Cu^{1.5+}...Cu^{1.5+}$ ground state which is a better model to the Cu_A center and exhibits some distinct differences. Nontheless valuable insight for the usage of HERFD-XANES and VtC-XES concerning dinuclear TM compounds was gained and information about oxidation state, spin state and geometry can be extracted.

The measurements and calculations need to be done for several other systems to check their broad applicability. This concerns especially other transition metal complexes used for photo reactions or found in enzymes. As mentioned before in-situ measurements and appropriate calculations have to be performed and analysed to complete the picture. In addition to that, pump-probe experiments are the next step to understand electron transfer reactions enabled by biomimetic complexes or light absorption processes in general.

Appendices

Bibliography

[1] G. Henkel et al., ‘The Active Sites of the Native Cytochrome-c Oxidase from Bovine Heart Mitochondria: EXAFS-Spectroscopic Characterization of a Novel Homobinuclear Copper Center(Cu_A) and of the Heterobinuclear Fe_{a3}-Cu_B Center’, *Angew. Chemie Int. Ed. English*, 1995, **34**, 1488–1492.

[2] T. Tsukihara et al., ‘Structures of metal sites of oxidized bovine heart cytochrome c oxidase at 2.8 Å’, *Science*, 1995, **269**, 1069–1074.

[3] S. Iwata et al., ‘Structure at 2.8 Å resolution of cytochrome c oxidase from Paracoccus denitrificans’, *Nature*, 1995, **376**, 660–669.

[4] K. Paraskevopoulos et al., ‘Insight into Catalysis of Nitrous Oxide Reductase from High-resolution Structures of Resting and Inhibitor-bound Enzyme from Achromobacter cycloclastes’, *J. Mol. Biol.*, 2006, **362**, 55–65.

[5] K. Brown et al., ‘A novel type of catalytic copper cluster in nitrous oxide reductase’, *Nat. Struct. Biol.*, 2000, **7**, 191–195.

[6] E. I. Solomon and R. G. Hadt, ‘Recent advances in understanding blue copper proteins’, *Coord. Chem. Rev.*, 2011, **255**, 774–789.

[7] E. I. Solomon et al., ‘Electronic Structures of Metal Sites in Proteins and Models: Contributions to Function in Blue Copper Proteins’, *Chem. Rev.*, 2004, **104**, 419–458.

[8] P. Hosseinzadeh et al., ‘Design of a single protein that spans the entire 2-V range of physiological redox potentials’, *Proc. Natl. Acad. Sci.*, 2016, **113**, 262–267.

[9] R. P. Houser, V. G. Young and W. B. Tolman, ‘A Thiolate-Bridged, Fully Delocalized Mixed-Valence Dicopper(I,II) Complex That Models the Cu_A Biological Electron-Transfer Site’, *J. Am. Chem. Soc.*, 1996, **118**, 2101–2102.

[10] J. J. Warren et al., ‘Inner- and outer-sphere metal coordination in blue copper proteins’, *J. Inorg. Biochem.*, 2012, **115**, 119–126.

[11] K. D. Karlin, *Bioinorganic Chemistry of Copper*, Springer Netherlands, Dordrecht, 2013, p. 1509.

[12] K. M. Lancaster et al., ‘Type-zero copper proteins.’, *Nat. Chem.*, 2009, **1**, 711–715.

[13] K. M. Lancaster et al., ‘Electron Transfer Reactivity of Type Zero Pseudomonas aeruginosa Azurin’, *J. Am. Chem. Soc.*, 2011, **133**, 4865–4873.

[14] K. M. Lancaster, Biological Outer-Sphere Coordination, in *Mol. Electron. Struct. Transit. Met. Complexes I*, ed. D. M. P. Mingos, P. Day and J. P. Dahl, Springer Berlin Heidelberg, Berlin, Heidelberg, 2012, pp. 119–153.

[15] J. C. Maxwell, ‘A Dynamical Theory of the Electromagnetic Field’, *Philos. Trans. R. Soc. London*, 1865, **155**, 459–512.

[16] G. Bunker, *Introduction to XAFS : a practical guide to X-ray absorption fine structure spectroscopy*, Cambridge University Press, 2010, p. 260.

[17] H. Winick, Proc. 1997 Part. Accel. Conf. (Cat. No.97CH36167), IEEE, 1998, vol. 1, pp. 37–41.

[18] S. Mobilio, F. Boscherini and C. Meneghini, *Synchrotron Radiation*, ed. S. Mobilio, F. Boscherini and C. Meneghini, Springer Berlin Heidelberg, Berlin, Heidelberg, 2015, pp. 1–799.

[19] M. de Broglie, ‘Sur une nouveau procédé permettant d’obtenir la photographie des spectres de raies des rayons Röntgen’, *Comptes Rendus*, 1913, 924–926.

[20] H. Fricke., ‘The K-Characteristic Absorption Frequencies for the Chemical Elements Magnesium to Chromium’, *Phys. Rev.*, 1920, **16**, 202–215.

[21] E. A. Stern, ‘Theory of the extended x-ray-absorption fine structure’, *Phys. Rev. B*, 1974, **10**, 3027–3037.

[22] E. A. Stern, D. E. Sayers and F. W. Lytle, ‘Extended x-ray-absorption fine-structure technique. III. Determination of physical parameters’, *Phys. Rev. B*, 1975, **11**, 4836–4846.

[23] D. E. Sayers, E. A. Stern and F. W. Lytle, ‘New Technique for Investigating Noncrystalline Structures: Fourier Analysis of the Extended X-Ray Absorption Fine Structure’, *Phys. Rev. Lett.*, 1971, **27**, 1204–1207.

[24] F. W. Lytle, D. E. Sayers and E. A. Stern, ‘Extended x-ray-absorption fine-structure technique. II. Experimental practice and selected results’, *Phys. Rev. B*, 1975, **11**, 4825–4835.

[25] J. E. Hahn et al., ‘Observation of an electric quadrupole transition in the X-ray absorption spectrum of a Cu(II) complex’, *Chem. Phys. Lett.*, 1982, **88**, 595–598.

[26] M. L. Baker et al., ‘K- and L-edge X-ray absorption spectroscopy (XAS) and resonant inelastic X-ray scattering (RIXS) determination of differential orbital covalency (DOC) of transition metal sites’, *Coord. Chem. Rev.*, 2017, **345**, 182–208.

[27] T. E. Westre et al., ‘A multiplet analysis of Fe K-edge 1s → 3d pre-Edge features of iron complexes’, *J. Am. Chem. Soc.*, 1997, **119**, 6297–6314.

[28] B. K. Teo, *EXAFS: Basic Principles and Data Analysis*, Springer Berlin Heidelberg, 1986, p. 349.

[29] D. C. Koningsberger et al., ‘XAFS spectroscopy ; fundamental principles and data analysis’, *Top. Catal.*, 2000, **10**, 143–155.

[30] M. Rovezzi and P. Glatzel, ‘Hard x-ray emission spectroscopy: a powerful tool for the characterization of magnetic semiconductors’, *Semicond. Sci. Technol.*, 2014, **29**, 023002.

[31] P. Glatzel, R. Alonso-Mori and D. Sokaras, Hard X-Ray Photon-in/Photon-out Spectroscopy: Instrumentation, Theory and Applications, in *X-Ray Absorption and X-Ray Emission Spectroscopy: Theory and Applications*, ed. J. A. Van Bokhoven and C. Lamberti, John Wiley & Sons, Ltd, Chichester, UK, 2016, ch. 6, pp. 125–153.

[32] H. A. Kramers and W. Heisenberg, ‘Über die Streuung von Strahlung durch Atome’, *Zeitschrift für Phys.*, 1925, **31**, 681–708.

[33] J. J. Sakurai, *Advanced quantum mechanics*, Addison-Wesley Publishing Company, 1967, p. 336.

[34] B. D. Cullity, *Elements of X-ray Diffraction*, Addison-Wesley Publishing Company, 1978, p. 555.

[35] X. Wang, F. de Groot and S. Cramer, ‘Spin-polarized x-ray emission of 3d transition-metal ions: A comparison via Kα and Kβ detection’, *Phys. Rev. B*, 1997, **56**, 4553–4564.

[36] P. Glatzel and U. Bergmann, ‘High resolution 1s core hole X-ray spectroscopy in 3d transition metal complexes - Electronic and structural information’, *Coord. Chem. Rev.*, 2005, **249**, 65–95.

[37] P. Glatzel, ‘X-Ray Fluorescence Emission Following K Capture and 1s Photoionization of Mn and Fe in Various Chemical Environments’, Dissertation, Universität Hamburg, 2001.

[38] U. Bergmann et al., ‘Chemical dependence of interatomic X-ray transition energies and intensities - a study of Mn Kβ'' and K$\beta_{2,5}$ spectra’, *Chem. Phys. Lett.*, 1999, **302**, 119–124.

[39] U. Bergmann and P. Glatzel, ‘X-ray emission spectroscopy’, *Photosynth. Res.*, 2009, **102**, 255–266.

[40] F. de Groot, ‘High-Resolution X-ray Emission and X-ray Absorption Spectroscopy’, *Chem. Rev.*, 2001, **101**, 1779–1808.

[41] N. Lee et al., ‘Probing Valence Orbital Composition with Iron Kβ X-ray Emission Spectroscopy’, *J. Am. Chem. Soc.*, 2010, **132**, 9715–9727.

[42] C. J. Pollock and S. Debeer, ‘Valence-to-core X-ray emission spectroscopy: A sensitive probe of the nature of a bound ligand’, *J. Am. Chem. Soc.*, 2011, **133**, 5594–5601.

[43] V. Martin-Diaconescu et al., ‘Kβ Valence to Core X-ray Emission Studies of Cu(I) Binding Proteins with Mixed Methionine – Histidine Coordination. Relevance to the Reactivity of the M- and H-sites of Peptidylglycine Monooxygenase’, *Inorg. Chem.*, 2016, **55**, 3431–3439.

[44] K. Hämäläinen et al., ‘Elimination of the inner-shell lifetime broadening in x-ray-absorption spectroscopy’, *Phys. Rev. Lett.*, 1991, **67**, 2850–2853.

[45] F. de Groot, G. Vankó and P. Glatzel, ‘The 1s x-ray absorption pre-edge structures in transition metal oxides’, *J. Phys. Condens. Matter*, 2009, **21**, 104207.

[46] A. J. Atkins, C. R. Jacob and M. Bauer, ‘Probing the Electronic Structure of Substituted Ferrocenes with High-Resolution XANES Spectroscopy’, *Chem. - A Eur. J.*, 2012, **18**, 7021–7025.

[47] M. Bauer, ‘HERFD-XAS and valence-to-core-XES: new tools to push the limits in research with hard X-rays?’, *Phys. Chem. Chem. Phys.*, 2014, **16**, 13827–13837.

[48] N. J. Vollmers et al., ‘Experimental and Theoretical High-Energy-Resolution X-ray Absorption Spectroscopy: Implications for the Investigation of the Entatic State’, *Inorg. Chem.*, 2016, **55**, 11694–11706.

[49] E. Kleimenov et al., ‘High-resolution hard-X-ray fluorescence spectrometer’, *J. Phys. Conf. Ser.*, 2009, **190**, 012035.

[50] H. H. Johann, ‘Die Erzeugung lichtstarker Röntgenspektren mit Hilfe von Konkavkristallen’, *Zeitschrift für Phys.*, 1931, **69**, 185–206.

[51] T. Johansson, ‘Über ein neuartiges, genau fokussierendes Röntgenspektrometer’, *Zeitschrift für Phys.*, 1933, **82**, 507–528.

[52] L. v. Hámos, ‘Röntgenspektroskopie und Abbildung mittels gekrümmter Kristallreflektoren’, *Naturwissenschaften*, 1932, **20**, 705–706.

[53] L. v. Hámos, ‘Röntgenspektroskopie und Abbildung mittels gekrümmter Kristallreflektoren. I. Geometrisch-optische Betrachtungen’, *Ann. Phys.*, 1933, **409**, 716–724.

[54] E. Fermi, ‘Eine statistische Methode zur Bestimmung einiger Eigenschaften des Atoms und ihre Anwendung auf die Theorie des periodischen Systems der Elemente’, *Zeitschrift für Phys.*, 1928, **48**, 73–79.

[55] L. H. Thomas, ‘The calculation of atomic fields’, *Math. Proc. Cambridge Philos. Soc.*, 1927, **23**, 542.

[56] N. Mardirossian and M. Head-Gordon, ‘Thirty years of density functional theory in computational chemistry: An overview and extensive assessment of 200 density functionals’, *Mol. Phys.*, 2017, **115**, 2315–2372.

[57] R. O. Jones, ‘Density functional theory: Its origins, rise to prominence, and future’, *Rev. Mod. Phys.*, 2015, **87**, 897–923.

[58] M. Casida and M. Huix-Rotllant, ‘Progress in Time-Dependent Density-Functional Theory’, *Annu. Rev. Phys. Chem.*, 2012, **63**, 287–323.

[59] A. D. Laurent and D. Jacquemin, ‘TD-DFT benchmarks: A review’, *Int. J. Quantum Chem.*, 2013, **113**, 2019–2039.

[60] F. Neese, ‘A critical evaluation of DFT, including time-dependent DFT, applied to bioinorganic chemistry’, *J. Biol. Inorg. Chem.*, 2006, **11**, 702–711.

[61] P. Hohenberg and W. Kohn, ‘Inhomogeneous Electron Gas’, *Phys. Rev.*, 1964, **136**, B864–B871.

[62] M. Born and R. Oppenheimer, ‘Zur Quantentheorie der Molekeln’, *Ann. Phys.*, 1927, **389**, 457–484.

[63] W. Kohn and L. J. Sham, ‘Self-Consistent Equations Including Exchange and Correlation Effects’, *Phys. Rev.*, 1965, **140**, A1133–A1138.

[64] W. Kohn, ‘Nobel Lecture: Electronic structure of matter—wave functions and density functionals’, *Rev. Mod. Phys.*, 1999, **71**, 1253–1266.

[65] D. S. Sholl and J. A. Steckel, *Density Functional Theory: A Practical Introduction*, John Wiley & Sons, Inc., Hoboken, NJ, USA, 2009, p. 252.

[66] A. Szabo and N. S. Ostlund, *Modern quantum chemistry: introduction to advanced electronic structure theory*, Dover Publications, 1996, p. 466.

[67] D. Marx and J. Hutter, *Ab initio molecular dynamics: basic theory and advanced methods*, Cambridge University Press, 2009, p. 567.

[68] K. Capelle, ‘A bird’s-eye view of density-functional theory’, *Brazilian J. Phys.*, 2006, **36**, 1318–1343.

[69] M. Iannuzzi and J. Hutter, ‘Inner-shell spectroscopy by the Gaussian and augmented plane wave method’, *Phys. Chem. Chem. Phys.*, 2007, **9**, 1599–1610.

[70] S. DeBeer George, T. Petrenko and F. Neese, ‘Prediction of Iron K-Edge Absorption Spectra Using Time-Dependent Density Functional Theory †’, *J. Phys. Chem. A*, 2008, **112**, 12936–12943.

[71] S. DeBeer George, T. Petrenko and F. Neese, ‘Time-dependent density functional calculations of ligand K-edge X-ray absorption spectra’, *Inorganica Chim. Acta*, 2008, **361**, 965–972.

[72] D. C. Rapaport, *The Art of Molecular Dynamics Simulation*, Cambridge University Press, Cambridge, 2004, p. 564.

[73] J. M. Haile, *Molecular Dynamics Simulation: Elementary Methods*, Wiley, New York, 1997, p. 512.

[74] J. M. Herbert and M. Head-Gordon, ‘Accelerated, energy-conserving Born-Oppenheimer molecular dynamics via Fock matrix extrapolation’, *Phys. Chem. Chem. Phys.*, 2005, **7**, 3269–3275.

[75] R. Car and M. Parrinello, ‘Unified Approach for Molecular Dynamics and Density-Functional Theory’, *Phys. Rev. Lett.*, 1985, **55**, 2471–2474.

[76] T. D. Kühne, ‘Second generation Car-Parrinello molecular dynamics’, *Wiley Interdiscip. Rev. Comput. Mol. Sci.*, 2014, **4**, 391–406.

[77] T. D. Kühne et al., ‘Efficient and Accurate Car-Parrinello-like Approach to Born-Oppenheimer Molecular Dynamics’, *Phys. Rev. Lett.*, 2007, **98**, 066401.

[78] J. Kolafa, ‘Time-reversible always stable predictor-corrector method for molecular dynamics of polarizable molecules’, *J. Comput. Chem.*, 2004, **25**, 335–342.

[79] A. H. Palser and D. E. Manolopoulos, ‘Canonical purification of the density matrix in electronic-structure theory’, *Phys. Rev. B - Condens. Matter Mater. Phys.*, 1998, **58**, 12704–12711.

Abbreviations

ASPC	Always stable predictor-corrector
AIMD	Ab-initio molecular dynamics
CtC	Core-to-Core
DFT	Density functional theory
DMEGqu	N-(1,3-dimethylimidazolidin-2-ylidene)quinolin-8-amine
EXAFS	Extended X-Ray absorption fine structure
FEL	Free electron laser
GAPW	Gaussian augmented plane wave
GIPAW	Gauge-including projector-augmented-wave
GPW	Gaussian plane wave
HERFD	High energy resolution fluorescence detection
HOMO	Highest occupied molecular orbital
HS	High-spin
I_0	Incident intensity
I_1	Transmitted intensity
(k)eV	(kilo) Electron volt
LUMO	Lowest occupied molecular orbital
LS	Low-spin
MD	Molecular dynamics
MLCT	Metal-to-ligand charge transfer
MO	Molecular orbital
TD-DFT	Time dependent density functional theory
VtC	Valence-to-Core
XANES	X-ray absorption near edge structure
XAS	X-ray absorption spectroscopy
XES	X-ray emission spectroscopy

List of Figures